



THE HONG KONG
POLYTECHNIC UNIVERSITY

香港理工大學

Pao Yue-kong Library

包玉剛圖書館

Copyright Undertaking

This thesis is protected by copyright, with all rights reserved.

By reading and using the thesis, the reader understands and agrees to the following terms:

1. The reader will abide by the rules and legal ordinances governing copyright regarding the use of the thesis.
2. The reader will use the thesis for the purpose of research or private study only and not for distribution or further reproduction or any other purpose.
3. The reader agrees to indemnify and hold the University harmless from and against any loss, damage, cost, liability or expenses arising from copyright infringement or unauthorized usage.

IMPORTANT

If you have reasons to believe that any materials in this thesis are deemed not suitable to be distributed in this form, or a copyright owner having difficulty with the material being included in our database, please contact lbsys@polyu.edu.hk providing details. The Library will look into your claim and consider taking remedial action upon receipt of the written requests.

**THEORETICAL UNDERSTANDING ON THE
FORMATION MECHANISM OF TWO
DIMENSIONAL MATERIALS**

QIU LU

M.Phil

The Hong Kong Polytechnic University

2017

**The Hong Kong Polytechnic University
Institute of Textiles and Clothing**

**Theoretical Understanding on the Formation
Mechanism of Two Dimensional Materials**

Qiu Lu

**A thesis submitted in partial fulfilment of the
requirements for the degree of Master of Philosophy**

January 2017

CERTIFICATE OF ORIGINALITY

I hereby declare that this thesis is my own work and that, to the best of my knowledge and belief, it reproduces no material previously published or written, nor material that has been accepted for the award of any other degree or diploma, except where due acknowledgement has been made in the text.

_____ (*Signed*)

_____ QIU LU _____ (*Name of student*)

Abstract

Since the discovery of graphene, within only one decade, great achievements have been made in the field of two dimensional (2D) materials and the researches on it is still very extensive because of its potential applications in electronic devices, energy harvesting, micro sensors, catalysis and so on. To realize these potential applications in real life and industrial scale, the synthesis of high quality 2D materials in large area at a reasonable cost is a critical step and therefore has attracted great attention. With more than 10 years' efforts, wafer-scale single-crystal monolayer graphene films have been fabricated on metal substrates with the so-called chemical vapor deposition (CVD) method as well as its large scale roll-to-roll production. In contrast to graphene, the techniques of synthesizing other 2D materials is far immature and many great challenges remain.

In this thesis, I report my recent studies of two important 2D materials, graphene and phosphorene, focusing on their structural stability and mechanisms regarding their synthesis. Three relative independent studies included in this thesis are:

- i) the mechanism of the ultrafast CVD growth of large area single crystal graphene on the copper foils with the continuous supply of oxygen. In this study, together with our experimental collaborators, we have revealed a key role of oxygen in graphene CVD growth on Cu surface, that it facilitates the catalytic decomposition of carbon feedstock and therefore enables the

ultrafast growth of graphene with the growth rate of ~ 3 mm/min, which is about two orders magnitude faster than previous record.

- ii) a global searching to find out the possible phosphorene isomers. In this study, we systematically explored more than 10 phosphorene isomers and have found a few ultra-stable isomers.

- iii) the potential of growing monolayer phosphorene films with CVD method on metal substrates. In this study, we have carefully explored the stability of four most important phosphorene isomers and studied the possibility of synthesizing them *via* a CVD method. In contrast to the intuition, we have found that blue phosphorene (BLP), instead of the black one, should be synthesized on most metal surfaces. The black one can be synthesized on Sn surface and the gamma one can be synthesized on Ru(0001) surface.

The above studies advance our knowledge of 2D materials' stability and the mechanism of their synthesis greatly and are very helpful for leading the large-scale synthesis of 2D materials in general. The conclusion that the growth of phosphorene is highly substrate dependent can be extended to nearly all 2D materials.

Publications Arising from the Thesis

1. Xu, X.; Zhang, Z.; Qiu, L.; Zhuang, J.; Zhang, L.; Wang, H.; Liao, C.; Song, H.; Qiao, R.; Gao, P.; Hu, Z.; Liao, L.; Liao, Z.; Yu, D.; Wang, E.; Ding, F.; Peng, H. and Liu, K. 2016, 'Ultrafast growth of single-crystal graphene assisted by a continuous oxygen supply', *Nature Nanotechnology*, vol. 11, pp. 930-935.
2. Qiu, L.; Dong, J.; Ding, F. 'Selective growth of two dimensional phosphorene on catalyst surface', *To be submitted*.
3. Qiu, L.; Dong, J.; Ding, F. 'High stable phosphorene isomers based on buckled honey', *Submitted to J. Am. Chem. Soc.*

Acknowledgements

First of all, I would like to express my deepest gratitude to my supervisor Associate Professor Feng Ding, without whose guidance and persistence this project would simply not have happened. Such academic insight and scientific pursuits of him have brought me into an interesting and promising research world, and inspired me for a further adventure in the field.

I would also like to thank Professor Zhenyu Li, who introduced me into the academic field and gave me great advice for the future career, and Professor Tianying Yan, whose generosity and encouragement in the code training of molecular dynamics greatly enhanced the depth of my research work.

I must also thank all of my group members, Dr. Jichen Dong, Associate Professor Ziwei Xu, Dr. Jianing Zhuang, Dr. Junfeng Gao, Dr. Wen Zhao, Dr. Xiao Wang, and Dr. Ding Yi. As the youngest colleague of the team, I received sincere welcome, creative and comprehensive advice, and unwavering support from them.

Finally, and most importantly, I would like to thank my parents, who have been supportive in every way possible, and who have shown the patience and forbearance of saints over the years this thesis has taken.

Table of Contents

Abstract	I
Publications Arising from the Thesis	III
Acknowledgements	IV
Table of Contents	V
List of Figures	VIII
List of Tables	XIII
List of Abbreviations	XXV
Chapter 1. Research Background	1
1.1 2D Materials and 2D Crystal Growth	1
1.1.1 Graphene	5
1.1.2 Phosphorene	9
1.1.3 Hexagonal Boron Nitride (h-BN) and Transition Metal Dichalcogenides (TMDCs)	15
1.2 The Synthesis of 2D Materials	19
1.2.1 Mechanical Exfoliation	20
1.2.2 Liquid-Phase Exfoliation	22
1.2.3 Chemical Synthesis	24
1.2.4 Chemical Vapor Deposition (CVD)	26
1.2.5 Summary of the Synthetic Methods	28

Chapter 2. Literature Review	31
2.1 CVD Growth of Graphene	31
2.1.1 From Multilayer to Monolayer Graphene	32
2.1.2 From Polycrystalline to Single Crystal Graphene.....	37
2.1.3 Mechanism Insight into the Graphene CVD Growth.....	44
2.2 Structure of Phosphorene	52
2.3 Synthesis of Phosphorene	56
2.4 Research Gap and Motivation	60
Chapter 3. Methodology	63
3.1 Density Functional Theory (DFT)	63
3.1.1 Basic Quantum Mechanics	64
3.1.2 Basic Density Functional Theories	67
3.1.3 Hohenberg-Kohn (HK) Theorem	69
3.1.4 The Kohn-Sham (KS) Equations	71
3.1.5 The Exchange-Correlation Functionals	74
3.2 Nudged Elastic Band (NEB) Method	75
Chapter 4. Graphene CVD Growth with Continuous Supply of Oxygen	79

4.1 Introduction	79
4.2 Experimental and Elementary Theoretical Results by Collaborators	80
4.3 Oxygen Assistance on CH ₄ Dissociation	87
4.4 Summary	97
Chapter 5. Isomers of Phosphorene	99
5.1 Introduction	99
5.2 A Global Searching Method for Phosphorene Isomers	100
5.3 Discussion of the Predicted Phosphorene Isomers	107
5.4 Summary	118
Chapter 6. Phosphorene CVD Growth on Catalyst Surfaces	120
6.1 Introduction	120
6.2 Theoretical Analysis of Phosphorene CVD Growth on Transition Metals	121
6.3 Summary	134
Chapter 7. Conclusions	136
Reference	140

List of Figures

- Figure 1.1** Some of the most studied 2D materials—(a) graphene, (b) silicene, (c) phosphorene, (d) h-BN, (e) MX with X = S, Se, ... and M = Sn, G, ..., (f) MX₂ with M = Mo, Nb, W, ... and X = S, Se, Te, ..., and (g) M₂X₂ with M = Ga, In, ..., X = S, Se, (h) M₂X₃ with M = Bi, ..., X = Se, Te, ... (c) Reprinted with permission from [20]. Copyright (2014) American Chemical Society.2
- Figure 1.2** (a) Wrinkled graphene in 3D space. Retrieved from <http://eandt.theiet.org>. (b) Different graphene domain shapes on catalyst surface. From reference [40]. Copyright (2013), Rights Managed by Nature Publishing Group.4
- Figure 1.3** (a) Graphene image by scanning probe microscope. Retrieved from <http://flickr.com/photos/10393857@N03/6795812766>. [47] (b) Graphene lattice and unit cell. (c) Graphene electronic band structure in 3D Brillouin zone. Retrieved from <http://www.uni-muenster.de/Physik.PI/Zacharias/research/graphene/graphene.html>. [48]5
- Figure 1.4** (a) Optical picture of the measured graphene-based quantum device. (b) σ_{xy} and ρ_{xx} vs gate voltages (V_g). (c) Hall resistance of the measured device. (a-c) From reference [49]. Reprinted with permission from AAAS. (d) SEM image of a large graphene film over a row of round holes. (e) Schematic of nanoindentation device. (d-e) From reference [50]. Reprinted with permission from AAAS. (f) Schematic of the experimental measured graphene based device with a graphene layer on a trench. (g) Shift of G peak as a function of the change in total dissipated power. (f-g) Reprinted

with permission from [51]. Copyright (2008) American Chemical Society.7

Figure 1.5 (a) Schematic of the graphene based device with Cu/Ni electrodes. (b) Optical microscope image of the measured device with SLG. (c) Cumulative probability as a function of resistance of the device. (d) Median resistance plot of length (e) and width. (a-e) Reprinted with permission from [52]. Copyright (2008) American Chemical Society. (f) Schematic of a graphene-based touch sensor. (g-h) A real production of smartphone with graphene-based touch panel. (f-h) From Wikipedia: https://commons.wikimedia.org/wiki/File:Graphene_Touch_Screen.png.....8

Figure 1.6 (a) Schematic of phosphorene-based FET device. (b) Source/drain current vs gate voltage measured with the FET device on a silicon substrate. Reprinted by permission from Macmillan Publishers Ltd : Nature Nanotechnology ([63]), copyright (2014).10

Figure 1.7 Atomic structure of few layer black phosphorene in (a) perspective view, (b) side view, and (c) top view. Reprinted with permission from [20]. Copyright (2014) American Chemical Society.11

Figure 1.8 (a) Electronic band structure of single layer black phosphorene. The dependence of phosphorene’s band gap on (b) number of layers and (c) the strain applied to the phosphorene plane. (a-c) Reprinted with permission from [20]. Copyright (2014) American Chemical Society. (d) The dependence of electronic mobility on the applied strain in the phosphorene plane. Reprinted with permission from [68].

Copyright (2014) American Chemical Society. **(e)** The difference of thermal conductivity along ac and zz directions. **(f)** Thermoelectric figure of merit vs doping carrier density. **(e, f)** Reprinted with permission from [72]. Copyright (2014) American Chemical Society.12

Figure 1.9 (a) Schematics of heterojunction device made of few-layer BP films on monolayer MoS₂. Reprinted with permission from [77]. Copyright (2014) American Chemical Society. **(b)** Optical micrograph of few-layer BP based device and its 3D image in detail. Reprinted with permission from [78]. Copyright (2014) American Chemical Society. **(c)** Schematic of a BP-based FET device. Reprinted with permission from [79]. Copyright (2015) American Chemical Society.14

Figure 1.10 Structure and lattice of h-BN (marked by red line).15

Figure 1.11 (a) The dependence of strain energy on the indentation depth of a h-BN sheet. **(b)** The breaking stress σ_{m2D} , breaking strain ϵ , and modulus E_{2D} as a function of the concentration of vacancies. **(a-b)** Reprinted with permission from [84]. Copyright (2010) American Chemical Society. **(c), (d)** The thermal conductance changes with the temperature with different widths of zz and ac h-BN nanoribbons. ©IOP publishing. Reproduced with permission from [85]. All rights reserved. **(e)** X-ray spectra for BN nanotube’s thermal stability before oxidation, heating to 700 °C and to 900 °C. Reprinted from [87], with the permission of AIP Publishing.16

Figure 1.12 Atomic structure of TMDC monolayer from top view and side view. (Transition metal atoms are marked in green and chalcogen in yellow.)18

Figure 1.13 (a) Schematic of a FET device based on MoS₂ monolayer nanosheets. Reprinted by permission from Macmillan Publishers Ltd: Nature Nanotechnology ([25]), copyright (2011). **(b)** Photoluminescence (PL) spectra of MoS₂. Insert: Raman spectra. **(c)** Optical micrograph of MoS₂ based FET device. **(b-c)** Reprinted with permission from [99]. Copyright (2011) American Chemical Society.19

Figure 1.14 (a) Optical micrograph of a large few-layer graphene film on Si wafer. **(b)** AFM image of the graphene film's edge with a 2 μm by 2 μm area. **(c)** AFM image of a graphene monolayer. **(a-c)** From reference [1]. Reprinted with permission from AAAS. **(d)** AFM image of h-BN nanosheets. **(e)** Height profile as a function of position marked with dashed lines in **(d)**. **(d-e)** Reprinted from [14], with the permission of AIP Publishing.21

Figure 1.15 (a-b) TEM image of multilayer graphene nanosheets with both 500 nm scale bar. **(c)** The number of graphene flakes vs the number of graphene monolayers per flake. Reprinted by permission from Macmillan Publishers Ltd: Nature Nanotechnology ([108]), copyright (2008).23

Figure 1.16 TEM images of few-layer BN nanosheets. The samples were prepared with different boric acid/urea mixture: **(a)** 1:12, **(b)** 1:24, and **(c)** 1:48. Reprinted with permission from ([118]). Copyright (2010) American Chemical Society.25

Figure 1.17 (a) Schematic of CVD growth process, where CH₄ feeds as precursor. Reprinted with permission from ([120]). Copyright (2012) American Chemical Society. **(b)** Schematic of the oxidation and reduction before CVD process. Reprinted with

permission from ([121]). Copyright (2013) American Chemical Society.26

Figure 1.18 (a) Optical micrograph of monolayer h-BN nanosheets. The corresponding **(b)** SEM, **(c)** AFM, **(d)** low magnification TEM, **(e)** SAED pattern, and **(f)** Raman images of this h-BN single layer. ©IOP publishing. Reproduced with permission from [130]. All rights reserved.28

Figure 2.1 (a) HRTEM image of planar few-layer graphene (PFLG). **(b)** Image of the marked PFLG film in **(a)** by high magnification TEM. **(a-b)** Reprinted from [145], Copyright (2006), with permission from Elsevier. **(c-f)** Images of mono-, triple-, quadruple-, and octet-layer graphene films by high magnification TEM. Reprinted with permission from ([37]). Copyright (2009) American Chemical Society.33

Figure 2.2 (a) SEM and **(b)** Optical microscope images of wrinkled graphene films on SiO₂/Si substrate. **(c)** Raman spectra of the marked regions. From [6]. Reprinted with permission from AAAS.34

Figure 2.3 Process of the roll-to-roll production of large area graphene. **(a)** Copper foil used in a quartz reactor in the growth. **(b)** Graphene transfer at 120 °C. **(c)** A large area graphene on a PET sheet. **(d)** Screen printing on graphene film on a PET sheet. **(e)** A touch panel made with this graphene/PET film. **(f)** A real computer with this graphene-based touch panel. Reprinted by permission from Macmillan Publishers Ltd: Nature Nanotechnology ([36]), copyright (2010).37

Figure 2.4 (a) SEM image of the merging graphene domains. **(b)** HR-TEM image of

graphene with a highlighted domain boundary. **(c)** The highlighted boundary area in detail. Reprinted with permission from [167]. Copyright (2011) American Chemical Society.38

Figure 2.5 The dependence of average graphene domain size on the hydrogen partial pressure. SEM images of graphene domain shapes on different partial pressure of hydrogen. Reprinted with permission from [170]. Copyright (2011) American Chemical Society.40

Figure 2.6 (a) SEM image of various graphene domains. **(b)** Frequency counts for different orientation angles with hexagonal domains. Inset: definition of the orientation angle. **(a-b)** reprinted with permission from [171]. Copyright (2012) American Chemical Society. **(c)** Schematic of single-crystal graphene monolayer growth with the merging of aligned seeds. **(d)** SEM image of graphene domains during growth. **(e)** Graphene on a Ge/Si substrate. **(f)** HR-TEM image of single crystal graphene (SCG) monolayer. Inset: SAED pattern. **(c-f)** From [126]. Reprinted with permission from AAAS. **(g)** Photograph of large area SCG on a Cu-Ni substrate. The local feeding is presented above. Reprinted by permission from Macmillan Publishers Ltd: Nature Materials [172], copyright (2015).42

Figure 2.7 (a) Formation energy and **(b)** second derivatives of the carbon clusters on Ni(111), Cu(111), Ru(0001), and Rh(111) surfaces. **(c)** C₂₁ and **(d)** C₂₄ clusters on Rh(111). Simulated **(e-h)** and **(i, j)** experimental STM images of carbon clusters found during graphene growth. **(a-j)** Reprinted with permission from [179]. Copyright (2012)

American Chemical Society. **(k)** Several stable C_{13} clusters and their formation energies on Ni(111) surface. Reprinted with permission from [178]. Copyright (2012) American Chemical Society.46

Figure 2.8 Atomic structures of C_N clusters on **(a)** terrace and **(b)** step of Ni(111) surface. **(c)** The dependence of carbon cluster's Gibbs free energy on the cluster size. **(d)** The dependence of nucleus size and nucleation barrier on chemical potential difference of carbon in graphene and feedstock. Reprinted with permission from [181]. Copyright (2011) American Chemical Society. ... 47

Figure 2.9 (a-h) Atomic structures of various kinds of graphene edges. **(i)** Formation energy of different edges types in vacuum and on different surfaces. **(a-i)** Reprinted with permission from [183]. Copyright (2012) American Chemical Society. **(j)** Atomic structures of of ac edges on Cu(111) surface. Adding two carbon atoms into **(k)** ac edge and **(l)** Cu-terminated ac edge on Cu(111) surface. **(m)** Structure of graphene edge with an arbitrary tilt angle. **(j-m)** reprinted with permission from [184]. Copyright (2012) American Chemical Society. **(n)** Wulff construction of graphene with different edges on different metals. [186] Copyright (2012) National Academy of Science.49

Figure 2.10 (a-c) Edge epitaxial growth of SCG on polycrystalline substrate. **(d)** Epitaxial growth of graphene on a polycrystalline surface to form polycrystalline graphene film. **(e)** Distance Between graphene and copper surface, and the dependence of binding energy on the rotation angle. **(f)** Energy evolution of C_{24} and C_{54} on copper

surface with rotation. Reprinted with permission from [187]. Copyright (2012) American Chemical Society.51

Figure 2.11 Atomic structures of (a) black and (b) blue phosphorenes. (c) The transformation from black phosphorene to blue phosphorene by dislocations. (d) Distance of AB stacked blue phosphorus layers at equilibrium. Reprinted with permission from [188]. Copyright (2014) by the American Physical Society.53

Figure 2.12 (a-d) Optimized atomic structures of α -P, β -P, γ -P, and δ -P phosphorenes. Reprinted with permission from [189]. Copyright (2014) by the American Physical Society.54

Figure 2.13 (a) Atomic structures of black, blue, and red phosphorenes. ©IOP publishing. Reproduced with permission from [191]. All rights reserved. (b) Atomic structures of phosphorene isomers with 5 hexagonal structures (α , β , γ , δ , ϵ) and 4 non-hexagonal structures (ζ , η , θ , ι). From reference [192], copyright (2016) by John Wiley & Sons, Inc. Reprinted by permission of John Wiley & Sons, Inc.55

Figure 2.14 (a) AFM image of phosphorene monolayer. (b) PL spectra of both phosphorene monolayer and bulk BP. (a-b) Reprinted with permission from [20]. Copyright (2014) American Chemical Society. (c) Optical micrograph of phosphorene films with one, two, three, four, and five layers. (d) Raman spectra of phosphorene films with different layers. (c-d) Reprinted with permission of Springer from [193]. Copyright (2014) Tsinghua University Press and Springer-Verlag Berlin Heidelberg. (e)

Raman spectrum of thin phosphorene film. **(f)** AFM image of phosphorene thin film. **(g)** Height profiles of phosphorene films marked in **(f)**. Reproduced from reference [194] with permission from The Royal Society of Chemistry.58

Figure 2.15 (a-b) AFM image of few-layer BP with different area size. Inset: height profile. **(a-b)** ©IOP publishing. Reproduced with permission from [195]. All rights reserved. **(c)** Simulated STM image of the modeled BLP. **(d)** Experimental STM image of BLP. **(e)** dI/dV curve of BLP single layer film. **(c-d)** Reprinted with permission from [196]. Copyright(2016) American Chemical Society.59

Figure 3.1 NEB and CINEB calculations of the MEP for CH_4 decomposition on Ir(111) surface. Reprinted from [223], with the permission of AIP Publishing.77

Figure 4.1 (a) Schematic of graphene ultrafast CVD growth on an oxidized substrate and **(b)** its side view. **(c)** Auger electron spectroscopy (AES) of SiO_2/Si substrate at $\sim 1,000$ °C illustrating the releasing of oxygen. Optical micrographs of graphene **(d)** large round domains on the back of the copper foil and **(e)** the small star-like domains on the front with SiO_2/Si substrate. Optical micrographs of graphene **(f)** large domains on the back of copper foils with Al_2O_3 and **(g)** small star-like domains with graphite substrate. Reprinted by permission from Macmillan Publishers Ltd: Nature Nanotechnology [122], copyright(2016).81

Figure 4.2 (a) SEM image of graphene domains. **(b-d)** SAED patterns of T_1 , T_2 and T_3 .

(e-h) LEED patterns of graphene domains of 4 different areas. (i-l) STM images of different areas in one graphene domain. Reprinted by permission from Macmillan Publishers Ltd: Nature Nanotechnology [122], copyright(2016).83

Figure 4.3 (a-c) Optical images of graphene size at different times. (a) $t = 0$ s stands for the moment when the graphene domain was visible at first time. (b) 2 s and (c) 5 s mean the graphene domain had grown for 2 and 5 seconds from the moment graphene domain was large enough to be seen. (d) Graphene domain size vs growth time. The slope indicates a $60 \mu\text{m/s}$ growth rate. (e) Graphene coverage vs growth time. Reprinted by permission from Macmillan Publishers Ltd: Nature Nanotechnology [122], copyright(2016).84

Figure 4.4 PFT simulation of the graphene domain evolution with carbon flux (F) change. (a-c), Graphene domain change, and (d-f) concentration profile change with carbon flux from 0.001 (a,d) to 0.1 (b,e) and then to 4 (c,f) by the PFT calculations. (g) Concentration profiles of the carbon species as precursor along the lines marked in (d, e, f). (h) Width of the depletion zone and (i) time for growing a domain with the size of 1/4 coverage as a function of the carbon flux. Reprinted by permission from Macmillan Publishers Ltd: Nature Nanotechnology [122], copyright(2016).86

Figure 4.5 CI-NEB calculation of CH_4 dissociation reaction with and without the assistance of oxygen on Cu(100) surface. (a) The energy barriers of the CH_4 decomposition reactions of $\text{CH}_4 + \text{O} \rightarrow \text{CH}_3 + \text{OH}$ (1) and $\text{CH}_4 \rightarrow \text{CH}_3 + \text{H}$ (2) on the Cu(100) surface with (black line) and without (red line) oxygen, are 0.62 and 1.57 eV,

respectively. **(b)** The MEP of decomposition reaction (1) (lower figure with black arrowheads), and reaction (2) (upper figure with red arrowheads) on copper surface with and without oxygen atoms, respectively. The white, red, black, and orange spheres represent H, O, C, and Cu atoms, respectively. All the atomic structures of reactants, transition states (TS), and products are optimized.90

Figure 4.6 CI-NEB calculation of CH₃/CH₂/CH dissociation reaction with and without the assistance of oxygen on Cu(100) surface. **(a), (c), (e)** The energy barriers of decomposition reactions of **(a)** CH₃+O → CH₂+OH (3) and CH₃ → CH₂+H (4) with (black line) and without (red line) oxygen, **(c)** CH₂+O → CH+OH (5) and CH₂ → CH+H (6) with (black line) and without (red line) oxygen, **(e)** CH+O → C+OH (7) and CH → C+H (8) with (black line) and without (red line) oxygen, on the Cu(100) surface, respectively. **(b), (d), (f)** The MEP of decomposition reaction (3), (5), (7) (lower figure of **(b), (d), (f)** with black arrowheads), and reaction (4), (6), (8) (upper figure of **(b), (d), (f)** with red arrowheads) on copper surface with and without oxygen atoms, respectively. The white, red, black, and orange spheres represent H, O, C, and Cu atoms, respectively. All the atomic structures of reactants, transition states (TS), and products are optimized.94

Figure 4.7 Summary of CI-NEB calculations of CH₄ full dissociation reactions with and without the assistance of oxygen on Cu(100) surface. The energy barriers of the CH₄ decomposition reactions of CH₄+O → CH₃+OH (1), CH₃+O → CH₂+OH (3), CH₂+O → CH+OH (5), and CH+O → C+OH (7) on the Cu(100) surface with

(black line) oxygen, are 0.62, 1.29, 0.53 and 1.11 eV, respectively; the energy barriers of the CH₄ decomposition reactions of CH₄ → CH₃+H (2), CH₃ → CH₂+H (4), CH₂ → CH+H (6), and CH → C+H (8) on the Cu(100) surface without (red line) oxygen, are 1.57, 1.37, 0.59, and 1.47 eV, respectively.95

Figure 5.1 (a) Phosphorus atom's sp³ hybridized orbital model. One of the sp³ orbital is occupied by a lone electron pair and the other three orbitals form covalent bonds with other atoms. **(b)** Simple atomic structures of black phosphorene, graphene, and blue phosphorene. The grey, light blue, and dark blue spheres represent carbon atoms, upper level and lower level phosphorus atoms, respectively.101

Figure 5.2 Phosphorene isomer models found under our isomer searching method. For two-atom unit cell, **(a)** shows the isomer found in a (1,0)×(0,1) unit cell. For four-atom unit cell, **(b)** shows the isomers found in a (1,0)×(0,2) unit cell. For six-atom unit cell, **(c)** shows the isomers found in a (1,0)×(0,3) unit cell. For eight-atom unit cell, **(d)**, **(e)**, and **(f)** show the isomers found in (1,0)×(0,4), (2,0)×(1,2), (2,0)×(0,2) unit cell.103

Figure 5.3 Optimized atomic structures of all the 14 phosphorene isomers found with our global searching method. **(a-n)** show the atomic structures of the 14 phosphorenes after optimization, labeled in Roman numbers from I to XIV, in top and side views, respectively. The dashed line draws out the unit cell of each phosphorene isomer. All the spheres represent phosphorus atoms while they are on the upper level, their color lighter, and on the lower level, their color darker, except for the white spheres

that stand for the phosphorus atoms bonding with only two neighbor atoms.105

Figure 5.4 Schematic diagram of the searching method for finding the four most well-known isomers, α , β , γ , and δ -phosphorene, from the original graphene honeycomb lattice.107

Figure 5.5 A comparison of the isomers found with our searching method and the well reported α -, β -, γ -, δ -, and ϵ -phosphorene. (a-e) show the atomic structures of P-I, P-IV, P-VIII, P-VII, and P-IX after optimization, in top and side views, respectively. **(f-j)** show the atomic structures of α -, β -, γ -, δ -, and ϵ -phosphorene reported before. **(f-i)** Reprinted with permission from [189]. Copyright (2014) by the American Physical Society. **(j)** From reference [192], copyright (2016) by John Wiley & Sons, Inc. Reprinted by permission of John Wiley & Sons, Inc.110

Figure 5.6 (a) Energy differences between all the isomers found and the black phosphorene with both PBE and HSE06 methods. Taking an energy difference of 0.175 eV per atom as a criterion, isomers with energy differences lower than it are considered as the relatively stable ones, including the widely reported α , β , γ , δ , and ϵ -phosphorene. **(b), (c), (d), and (e)** are the optimized atomic structures of the four newly found stable phosphorene isomers labeled as P-II, P-III, P-V, and P-VI, in top and side view, respectively. The dashed lines draw out the unit cell of each phosphorene isomer.113

Figure 5.7 Structural comparison of the most stable phosphorene isomers. (a-f)

Structural simplifications of P-IV, P-II, P-I, P-V, P-III, and P-IV', respectively. **(g)** Schematic diagram of structural similarities and differences of isomer P-I, P-II, P-III, P-IV and P-V. Side view images of these phosphorene isomers are seen as simply composed of χ and χ' elements. The top and bottom red colored figures in **(g)** are two mirror symmetrical images of blue phosphorene **(a)** and **(f)**.114

Figure 5.8 Band structures of the phosphorene isomers. Electronic band structures of the eight most stable phosphorene isomers, **(a)** P-I (α), **(b)** P-II, **(c)** P-III, **(d)** P-IV (β), **(e)** P-V, **(f)** P-VI, **(g)** P-VII (δ), and **(h)** P-VIII (γ) with HSE06 method.116

Figure 5.9 Band gaps of all the 14 found phosphorene isomers. The blue space represents the conduction band while the red space represents the valence band. Thus the white space in the middle denotes the band gap of each phosphorene.117

Figure 6.1 Optimized atomic structures of α , β , γ , and δ -phosphorene in vacuum in top, front, and left views. Lattice parameters are denoted with black lines. The light blue spheres represent the upper level phosphorene atoms while the dark blue spheres represent the bottom level phosphorus atoms.122

Figure 6.2 Optimized atomic structures of Ag(111), Au(111), Cu(111), Ni(111), Pt(111), Ru(0001) and β -Sn(100) surfaces.123

Figure 6.3 Atomic structures of (a) α -, (b) β -, (c) γ -, and (d) δ -phosphorene on β -Sn(100) surface in top view, front view and left view. The green, light blue and dark

blue spheres represent tin, upper level and bottom level phosphorus atoms, respectively.125

Figure 6.4 Optimized atomic structures of α , β , γ , and δ -phosphorene on **(a-d)** Au(111) and **(e-h)** Ni(111) surfaces in top, front and left views. The yellow, purple, light blue and dark blue spheres represent the gold, nickel, upper level and bottom level phosphorus atoms.128

Figure 6.5 Charge Density Difference (CDD) Plots of phosphorenes on substrates. **(a)**, **(c)** and **(e)** are models of α -phosphorenes on β -Sn(100), Au(111) and Ni(111) surfaces, while **(b)**, **(d)** and **(f)** are β -phosphorenes on β -Sn(100), Au(111) and Ni(111) surfaces, respectively. The iso-surface levels are all set at $0.002 e^*a_0^{-3}$, where e is the elementary electron charge, and a_0 is the Bohr radius.129

Figure 6.6 Optimized atomic structures of α -phosphorene on β -Sn(100), Au(111), Ag(111), Cu(111), Ni(111), Pt(111), and Ru(0001) surfaces in top and front views, respectively. The distances between α -phosphorene and the substrates are 2.98, 2.63, 2.61, 2.24, 1.75, 2.20, and 1.95 Å, respectively.130

Figure 6.7 Formation energies (a) and binding energies (b) of α , β , γ , and δ -phosphorene on Ag(111), Au(111), Cu(111), Ni(111), Pt(111), Ru(0001) and β -Sn(100) surfaces, respectively.133

List of Tables

Table 1.1 A comparison of various methods for the graphene synthesis, where SLG, FLG and MLG stand for single, few (<i>i.e.</i> , 2-10) and many layer (>10) graphene, respectively.	30
Table 2.1 Graphene CVD growth on different transition metal substrates, where SLG, FLG and MLG stand for single, few (<i>i.e.</i> , 2-10) and multi-layer (>10) graphene, respectively.	36
Table 5.1 Optimized lattice parameters and energy differences of the phosphorene isomers: lattice parameters a_1 , a_2 (in Å), θ (°), and energy differences (eV/atom) between every isomer and isomer I (α -phosphorene) by PBE and HSE06.	109
Table 5.2 Band gap of the eight most stable phosphorene isomers with both PBE and HSE06 methods.	116
Table 6.1 Calculated parameters of the four phosphorene isomers used in this study. a , a_2 , and θ are the lattice parameters of the super cell models. E_f is the formation energy of the phosphorene isomer in vacuum.	123
Table 6.2 Calculated parameters of all the phosphorene-on-substrate models. a and b are the lattice parameters of the modeled super cells. a_p , b_p , a_m and b_m represent the lattice mismatches (along a and b directions) in percentage for phosphorene and the metal substrates, respectively, in comparison with the freestanding phosphorene and bulk metal; d is the distance between the phosphorene and the metal substrate after	

optimization; E_f and E_b are the formation energy and binding energy as defined in this
main text.130

List of Abbreviations

Å	Angstrom
AC	Armchair
AES	Auger Electron Spectroscope
AFM	Atomic Force Microscope
BLP	Blue Phosphorene
BP	Black Phosphorene
CBM	Conduction Band Minimum
CI-NEB	Climbing Image Nudged Elastic Band
CVD	Chemical Vapor Deposition
DFT	Density Functional Theory
eV	Electron Volt
FET	Field Effect Transistor
FLG	Few Layer Graphene
GGA	Generalized Gradient Approximation
GO	Graphite/Graphene Oxide
h-BN	Hexagonal Boron Nitride
HF	Hartree-Fock
HK	Hohenberg-Kohn
HRTEM/HR-TEM	High Resolution Transmission Electron Microscope
HSE	Heyd-Scuseria-Ernzerhof
KS	Kohn-Sham
LDA	Local Density Approxiamtion
LEED	Low-Energy Electron Diffraction
LPCVD	Low Pressure Chemical Vapor Deposition
MC	Monte Carlo
MD	Molecular Dynamics
MEP	Minimum Energy Path
ML	Monolayer
MLG	Multi Layer Graphene
NEB	Nudged Elastic Band

NMP	N-Methyl-2-pyrrolidone
PAW	Projected Augmented Wave
PBC	Periodic Boundary Condition
PBE	Perdew-Burke-Ernzerhof
PET	Polyethylene Terephthalate
PFLG	Planar Few Layer Graphene
PFT	Phase Field Theory
PL	Photoluminescence
PMMA	polymethylmethacrylate
P-P	Phosphorus-Phosphorus
P-P-P	Phosphorus-Phosphorus-Phosphorus
QHE	Quantum Hall Effect
SAED	Selected Area Electron Diffraction
SCG	Single Crystal Graphene
SEM	Scanning Electron Microscope
SLG	Single Layer Graphene
STM	Scanning Tunneling Microscope
TEM	Transmission Electron Microscope
TF	Thomas-Fermi
TMDs	Transition Metal Dichalcogenides
TS	Transition State
VASP	Vienna ab initio Simulation Package
VBM	Valence Band Maximum
ZZ	Zigzag
2D	Two Dimensional
3D	Three Dimensional
α -P	α -Phosphorene
β -P	β -Phosphorene
γ -P	γ -Phosphorene
δ -P	δ -Phosphorene
ε -P	ε -Phosphorene

Chapter 1. Research Background

This chapter starts with a brief introduction of some well-known 2D materials—graphene, phosphorene, hexagonal boron nitride (h-BN), and transition metal dichalcogenides (TMDCs). Their unique structures and properties are also presented. The most used methods for the synthesis of these 2D materials, including mechanical exfoliation, liquid-phase exfoliation, chemical synthesis, and CVD method, are then introduced. In the last part of this chapter, a discussion on their advantages and disadvantages is shown.

1.1 2D Materials and 2D Crystal Growth

The study of 2D materials has become a fashion among physicists, chemists, and materials scientists since the mechanical exfoliation of graphene from graphite with a Scotch tape by Geim and Novoselov, who were later awarded the Nobel Prize in Physics in 2010. [1-5] With its exceptional electronic properties that allow the electrons to flow freely along its 2D surfaces, currently, graphene stands out as the most extensively explored 2D material. [1, 6-9] While, its zero band gap nature prevents its application in semiconductor switches. The emerging of other 2D materials, such as h-BN, [10-14] silicene [15-19], phosphorene, [20-24] and TMDCs (M_nX_m , where $(n,m) = (1,1), (1,2), (2,2), (2,3)$ etc.) [25-29] etc. (Figure 1.1), enriches the family of 2D materials and

greatly expands the applications of 2D materials in electronic and photonic devices, energy storage and conversion, catalysis, seawater desalination and composite materials, *etc.* [30-35] It is highly expected that today's extensive study on 2D materials might lead to another industrial revolution and a great change of human life.

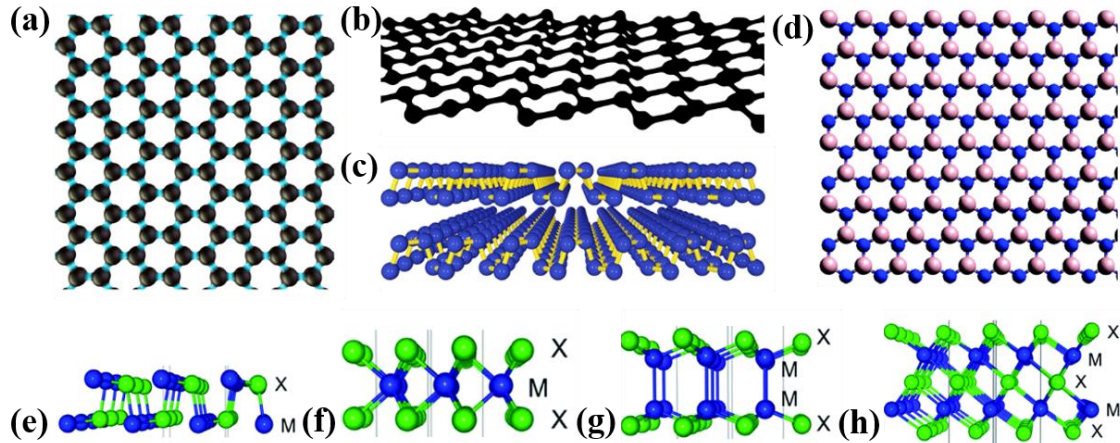


Figure 1.1 Some of the most studied 2D materials—(a) graphene, (b) silicene, (c) phosphorene, (d) h-BN, (e) MX with X = S, Se, ... and M = Sn, G, ..., (f) MX₂ with M = Mo, Nb, W, ... and X = S, Se, Te, ..., and (g) M₂X₂ with M = Ga, In, ..., X = S, Se, (h) M₂X₃ with M = Bi, ..., X = Se, Te, ...

(c) Reprinted with permission from [20]. Copyright (2014) American Chemical Society.

Although there's no well accepted definition yet, 2D materials are usually atomic thin along one direction and can be infinite large along another two directions. Most recently studied 2D materials are one or a few atomic layers thick ($d < 2$ nm). Both sides of a 2D material should be chemically inert or interact weakly with other materials, such as a substrate (binding energy ranges from $E_b \sim 0.03 - 0.2$ eV/atom). Due to its atomic scale thickness, a 2D material possesses extremely small bending rigidity of $EI \sim h^3$, which may lead to a high fluctuation along the thickness direction, while the in-plane

modulus can be as high as the corresponding bulk material (e.g., $E \sim 1,000$ GPa for graphene under stretch). [36] This large fluctuation along the thickness direction (Figure 1.2a), however, may cause serious problem in the synthesis of 2D materials, *i.e.*, a 2D material in large area cannot maintain its flatness in a 3D space and therefore a substrate support is required for the synthesis of all 2D materials in large area. Because a 2D material is atomic thick, there is a large percentage of atoms attached to the substrate and, as a consequence, the substrate must play an important role in 2D material synthesis.

2D crystal growth is very different from the growth of three dimensional (3D) crystals, whose mechanism has been exhaustively explored for more than 100 years. [37,38] In a 3D crystal growth, the addition of each atomic layer is on a lattice perfect matching substrate and all the added atoms/molecules interact strongly with the substrate, this ensure a perfect epitaxial growth behavior. While, the 2D crystal growth needs to form only one or a few layer of atoms on a hetero-surface and there is normally no lattice matching and the interaction between the added atoms/molecules and the substrate is usually very low.

As a consequence of above differences, the behaviors of 2D material growth are more complicated than that of 3D crystal. For example, a 3D crystal grown in solution or substrate normally is in regular polyhedral shape but graphene of various shapes can be formed on liquid copper surface by varying the pressure of H_2 in the carrier gas only

(Figure 1.2b) [39].

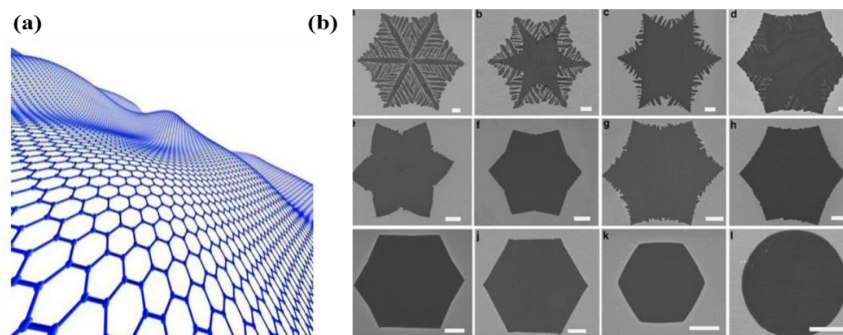


Figure 1.2 (a) Wrinkled graphene in 3D space. Retrieved from <http://eandt.theiet.org>. (b) Different graphene domain shapes on catalyst surface. From reference [40]. Copyright (2013), Rights Managed by Nature Publishing Group.

Above analysis indicates that the growth mechanism of 2D materials cannot be obtained by simply applying our knowledge of 3D crystal growth in a 2D space and there are many unrevealed fundamentals, for example how the symmetry substrate affect the growth of 2D materials, how the interaction between 2D material and substrate affect the growth, *etc.* Therefore, a careful exploration is pressing and important for improving our present techniques of 2D material synthesis and to enrich our knowledge of 2D crystal growth.

Next we further introduce several most studied 2D material briefly—graphene in section 1.1.1, phosphorene in section 1.1.2, h-BN and TMDCs in section 1.1.3.

1.1.1 Graphene

Graphene is a quick rising star of 2D materials since 2004. Due to its excellent electronic, thermal, chemical and mechanical properties, the single-atom-thick 2D material is believed to be one of the key materials for our sustainable future. This material is a unique member of carbon family, in the form of a two-dimensional, one-atomic-thick, honeycomb lattice. The word “graphene” was firstly introduced to describe single sheet of graphite in 1987 [41]. The early research of graphene, most theoretical studies, was for the understanding of the 3D graphite [42]. Later as the technology improved, few- and single-layer graphene were observed clearly by electron microscopies [43,44]. It was not until the isolation of free-standing single-layer graphene by Geim and Novoselov [1] that the star material has shot into prominence at a speed notably faster than its sisters, fullerenes (“born” in 1985 [45]) and carbon nanotubes (“born” in 1991 [46]).

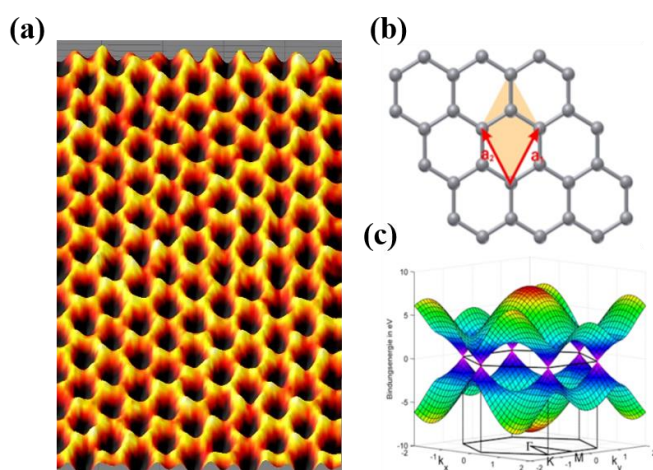


Figure 1.3 (a) Graphene image by scanning probe microscope. Retrieved from <http://flickr.com/photos/10393857@N03/6795812766>. [47] (b) Graphene lattice and unit cell. (c)

Graphene electronic band structure in 3D Brillouin zone. Retrieved from <http://www.uni-muenster.de/Physik.PI/Zacharias/research/graphene/graphene.html>. [48]

As shown in Figure 1.3a, the stability of graphene results from the preferred sp^2 orbital hybridization of C carbon atoms. In graphene, each atom connects its three neighbors by σ -bonds, and the π -electrons form a large aromatic π -bond on both sides of the graphene plane. The distribution of electrons among the π -orbitals, which are close to the Fermi level, determines graphene's most notable properties. As shown in Figure 1.3, perfect graphene is a zero band gap metallic material and possesses a linear density of state (DOS) near the Fermi level, which means the carriers of graphene are massless. Experimental observed DOS in graphene clearly proved the existence of massless Dirac quasiparticles in graphene. [3,5] As a result of this ambipolar electric field effect, the density of carriers can be easily tuned and the mobility exceeds $15,000 \text{ cm}^2\text{V}^{-1}\text{s}^{-1}$ at room temperature. [1] As a consequence of the high carrier mobility and its 2D nature of graphene, the quantum hall effect (QHE) was measured even at room temperature, which opens up a new field for research for the development of graphene-based quantum devices (Figure 1.4a, b, c). [49]

Besides the superior electronic properties, graphene also owns exceptional mechanical and thermal properties. Measured by nanoindentation method in an atomic force microscope (AFM), the Young's modulus of freestanding monolayer graphene is 1.0 TPa and its strength reaches 130 GPa (Figure 1.4 d, e). [50] Its thermal conductivity of $\sim 5,000 \text{ W}\cdot\text{m}^{-1}\cdot\text{K}^{-1}$ was also extracted from experimental measurements at room temperature. This extremely high thermal conductivity indicates the great potential of using graphene as thermal management materials (Figure 1.4f, g). [51]

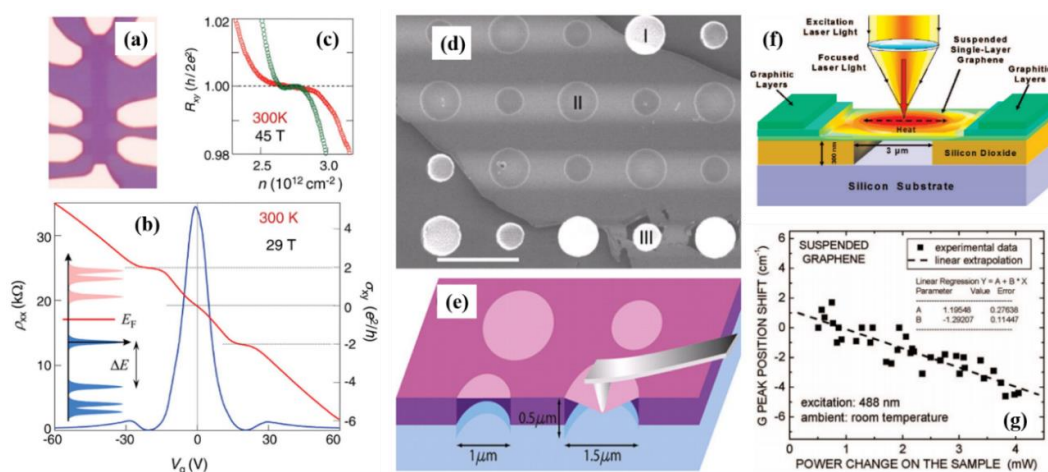


Figure 1.4 (a) Optical picture of the measured graphene-based quantum device. (b) σ_{xy} and ρ_{xx} vs gate voltages (V_g). (c) Hall resistance of the measured device. (a-c) From reference [49]. Reprinted with permission from AAAS. (d) SEM image of a large graphene film over a row of round holes. (e) Schematic of nanoindentation device. (d-e) From reference [50]. Reprinted with permission from AAAS. (f) Schematic of the experimental measured graphene based device with a graphene layer on a trench. (g) Shift of G peak as a function of the change in total dissipated power. (f-g) Reprinted with permission from [51]. Copyright (2008) American Chemical Society.

As a result of these exceptional mechanical, thermal, and electronic properties, graphene has been considered as the key material for many applications. Long before, graphene has been regarded as a new material for field effect transistor (FET) devices to replace silicon in the future. [1,3,5] Jiwoong Park *et al.* reported a graphene-based device, which presents promising electrical properties with a excellent carrier mobility of $700 \text{ cm}^2\text{V}^{-1}\text{s}^{-1}$ and superior current saturation characteristics. [52] The device is shown in Figure 1.5, in which we can see the patterned Cu/Ni electrodes and the graphene on them. Due to the surface adsorption dependent conductance, graphene can be used as a sensor to detect the absorbed molecules, such as gases. [53-55] Other potential applications of graphene, such as various sensors, transparent conducting films, energy storage and generation, catalysis, graphene-polymer nanocomposites, *etc.* are also widely explored. [56-59]

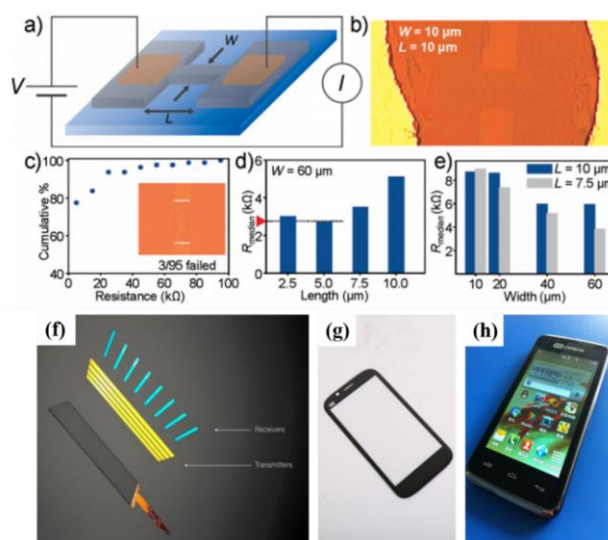


Figure 1.5 (a) Schematic of the graphene based device with Cu/Ni electrodes. (b) Optical microscope image of the measured device with SLG. (c) Cumulative probability as a function of

resistance of the device. **(d)** Median resistance plot of length **(e)** and width. **(a-e)** Reprinted with permission from [52]. Copyright (2008) American Chemical Society. **(f)** Schematic of a graphene-based touch sensor. **(g-h)** A real production of smartphone with graphene-based touch panel. **(f-h)** From Wikipedia: https://commons.wikimedia.org/wiki/File:Graphene_Touch_Screen.png.

Except for the great promise graphene holds for future device applications, including light-emitting diodes, solar cells, touch panels as well as smart phones [60], graphene has already been sold for commercial uses. As of 2015, a graphene-infused printer powder is available [61]. In areas like electronics, light/strong composite materials, filtration, biological engineering, energy storage and photovoltaic, many possibilities for use have been proposed or are under development [62]. Therefore, for these great potential in applications, both experimental and theoretical research works on the synthesis of graphene are essential.

1.1.2 Phosphorene

Recently, a newly emerged 2D material, phosphorene, has also interested many scientists of 2D materials due to its single element composition and excellent properties. In 2014, Yuanbo Zhang's research group in Fudan University firstly reported that the synthesized few-layer black phosphorus (BP) films with thickness of a few nanometers from bulk black phosphorus can be used to fabricate high performance FET (Figure

1.6). [63] The drain current modulation of FET reaches 10^5 and the charge-carrier mobility was found up to $\sim 1,000 \text{ cm}^2\text{V}^{-1}\text{s}^{-1}$. The outstanding performances in electronic device promise us a new star material and the research on phosphorene becomes exotic since then.

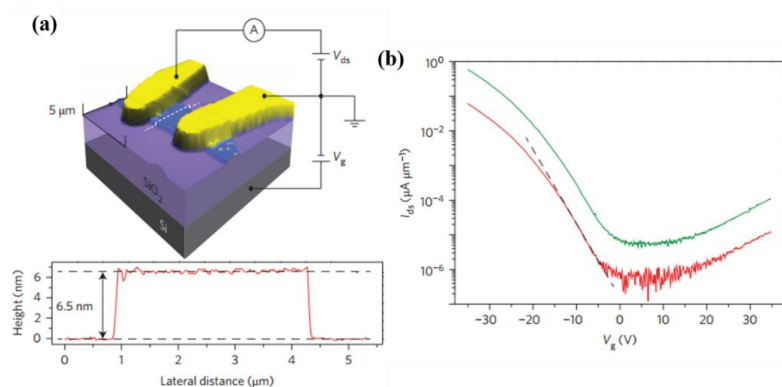


Figure 1.6 (a) Schematic of phosphorene-based FET device. (b) Source/drain current vs gate voltage measured with the FET device on a silicon substrate. Reprinted by permission from Macmillan Publishers Ltd : Nature Nanotechnology ([63]), copyright (2014).

Same as carbon in graphene, each phosphorus atoms in phosphorene is 3-fold coordinated. However, unlike sp^2 -bonded flat graphene monolayer, BP displays a unique anisotropic nature within the plane due to its sp^3 -bonded puckered structure. As indicated in Figure 1.7, the phosphorus-phosphorus-phosphorus (P-P-P) bonding angle is smaller than that in graphene, which results in the buckling of the phosphorene layer and the reduction of the symmetry of the 2D material. The bond angle along the zigzag direction is about 96° and the phosphorus-phosphorus (P-P) bond length is 2.224 \AA , while the bond angle (dihedral angle) along the armchair direction is about 103° and the corresponding bond length is 2.244 \AA . Resulting from this intrinsic anisotropy and

the particular puckered structure in contrast to graphene, BP possesses very unique mechanical, electronic, optoelectronic, and thermoelectric properties.

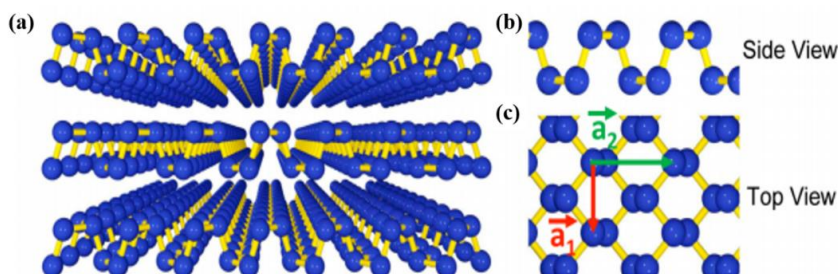


Figure 1.7 Atomic structure of few layer black phosphorene in (a) perspective view, (b) side view, and (c) top view. Reprinted with permission from [20]. Copyright (2014) American Chemical Society.

For example, the anisotropic structure of black phosphorene, first of all, directly leads to the difference in tensile strengths along the zigzag and armchair directions. Reported by Xihong Peng's group in 2014, the ideal monolayer phosphorene has the critical strains of 27% and 30% along the two directions, respectively, as shown in Figure 1.8a, b. [64] This work demonstrates the superior mechanical flexibility of phosphorene compared with other 2D materials, such as graphene. Besides, a negative Poisson's ratio was also observed in the out-of-plane direction under uniaxial deformation. [65]

Depending on the number of layers, the black phosphorene has a direct band gap ranging from 0.3 eV to 2 eV [63], which is larger than that of graphene (0 eV) [2] but smaller than that of MoS₂ series materials(1.1-2.5 eV) [28]. The band gap range bridges the gaps of the two important 2D materials. It is intriguing that the band gap of phosphorene, as well as the in-layer strain, depends on the number of layers as shown in Figure 1.8a, b, c. [20] The moderate gap enables BP based FETs to have a high on/off ratio of 10⁴-10⁵ [20,63] and high carrier mobility of ~ 1000 cm²/V·s [63,66], making it suitable for various high performance electronic applications. More interestingly, the anisotropic effective mass of phosphorene leads to anisotropic electrical conductance and electron mobility. As shown in Figure 1.8d, the mobility along the armchair direction is much larger than that along the zigzag direction. [20,67]

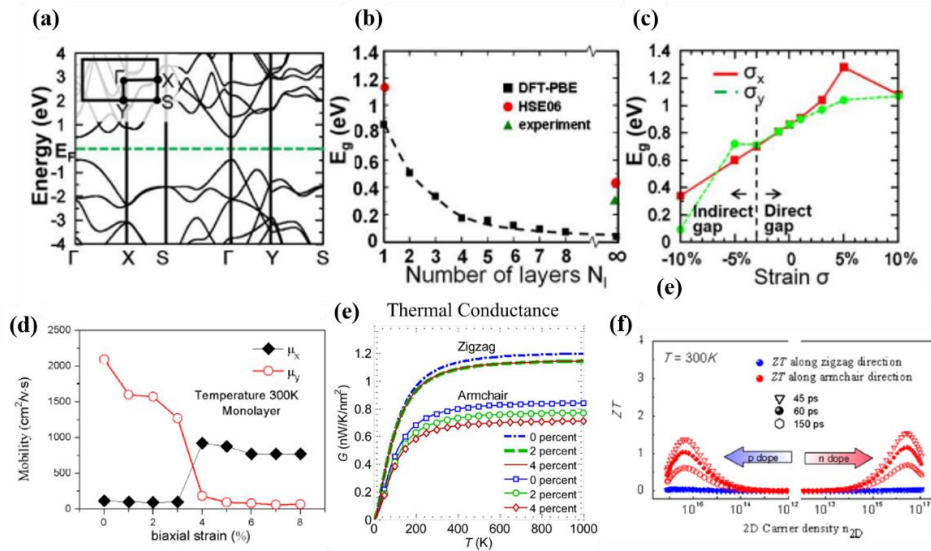


Figure 1.8 (a) Electronic band structure of single layer black phosphorene. The dependence of phosphorene’s band gap on (b) number of layers and (c) the strain applied to the phosphorene plane.

(a-c) Reprinted with permission from [20]. Copyright (2014) American Chemical Society. (d) The dependence of electronic mobility on the applied strain in the phosphorene plane. Reprinted with permission from [68]. Copyright (2014) American Chemical Society. (e) The difference of thermal conductivity along ac and zz directions. (f) Thermoelectric figure of merit vs doping carrier density. (e, f) Reprinted with permission from [72]. Copyright (2014) American Chemical Society.

Except for the well-known electronic properties, phosphorene also shows superiority in thermoelectricity. Along the armchair direction, phosphorene possesses prominent electron transport and poor thermal conductance of $\sim 36 \text{ W/m}\cdot\text{K}$ only. [69-72] This combination of high electrical conductance and poor thermal conductance gives phosphorene a significant promise for the thermoelectric devices compared with graphene and MoS_2 . [73-76]

Since the first synthesis of black phosphorus thin films as FET material, a large number of scientists have devoted into the field for the extensive device applications in electronics, optoelectronics, batteries, and so on. As mentioned above, phosphorene's moderate and tunable band gap with its relatively high mobility allow a high on/off ratio for phosphorene-based transistor with high operation effectiveness, which was demonstrated first by Yuanbo Zhang's group [63] experimentally. In contrast, the semi-metallic nature limits graphene to be with low on/off ratio and the moderate carrier mobility of TMDCs means low electronic performance. Further explorations greatly improved the performance of phosphorene based electronic devices, their stability and

reliability. [77-80] As shown in Figure 1.9, Peide Ye's group reported a gate-tunable p-n diode based on a p-type BP/n-type MoS₂ heterojunction, demonstrating a maximum photodetection responsivity of 418 mA/W and high capability of photovoltaic energy conversion (Figure 1.9a) [77]. Yong-Won Song *et al.* investigated the effect of Al₂O₃ passivation on phosphorene FET devices' current fluctuation reduction (Figure 1.9b) [78]. Flexible BP FETs with superior electron and hole mobilities was first reported by Deji Akinwande's team (Figure 1.9c) [79].

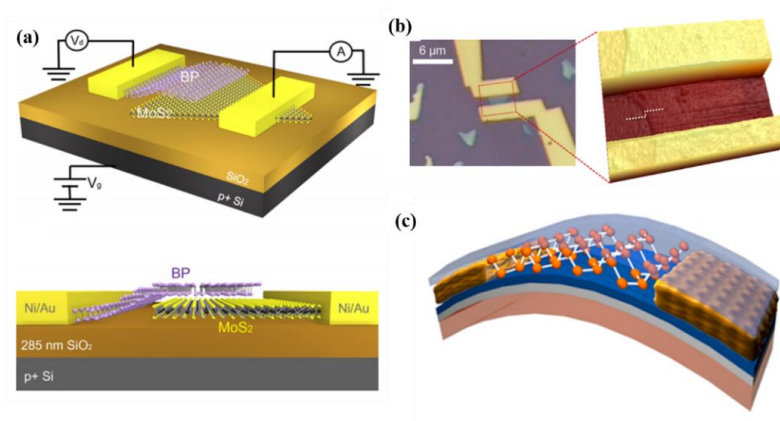


Figure 1.9 (a) Schematics of heterojunction device made of few-layer BP films on monolayer MoS₂. Reprinted with permission from [77]. Copyright (2014) American Chemical Society. (b) Optical micrograph of few-layer BP based device and its 3D image in detail. Reprinted with permission from [78]. Copyright (2014) American Chemical Society. (c) Schematic of a BP-based FET device. Reprinted with permission from [79]. Copyright (2015) American Chemical Society.

Phosphorene's potential for batteries, optoelectronics and photodetectors are also reported and demonstrated. [66,81-83] However, due to the high activity of phosphorus under ambient conditions, there is still few method of synthesizing phosphorene in high

quality and large area and more research efforts should be dedicated to that direction.

1.1.3 Hexagonal Boron Nitride (h-BN) and Transition Metal Dichalcogenides (TMDCs)

As shown in Figure 1.10, the 2D h-BN has very similar honeycomb lattice with graphene, while half of the carbon atoms are substituted by boron and another half by nitrogen.

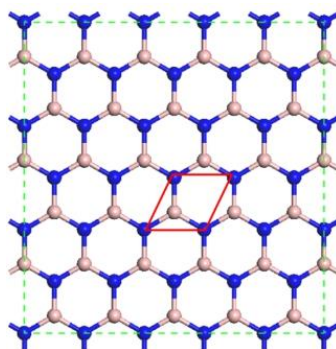


Figure 1.10 Structure and lattice of h-BN (marked by red line).

H-BN, due to its strong in-plane sp^2 bonds, shows great mechanical strength, thermal stability at high temperature and thermal conductivity as well as chemical stability. The Young's modulus of h-BN thin film with thickness of 1-2 nm was calculated to be in the range of $220-510 \text{ N}\cdot\text{m}^{-1}$. Further considering the stacking order, the Young's modulus of single h-BN layer is predicted to be $270 \text{ N}\cdot\text{m}^{-1}$ (Figure 1.11a, b). [50,84] Later, by calculating the phonon spectrum and the thermal conductance, it was found that h-BN nanoribbons have excellent thermal conductivity (Figure 1.11c, d). The thermal conductivity of h-BN nanoribbons is comparable with that of graphene

nanoribbons and even exceeds the latter at low room temperature. [85,86] Further research also found that h-BN nanotubes remain stable at 700 °C in air and the onset temperature of h-BN nanotube oxidation is as large as 800 °C (Figure 1.11e), much higher than that of carbon nanotube. [87] This high level of thermal and chemical stability indicates that h-BN can be used as important components of excellent devices.

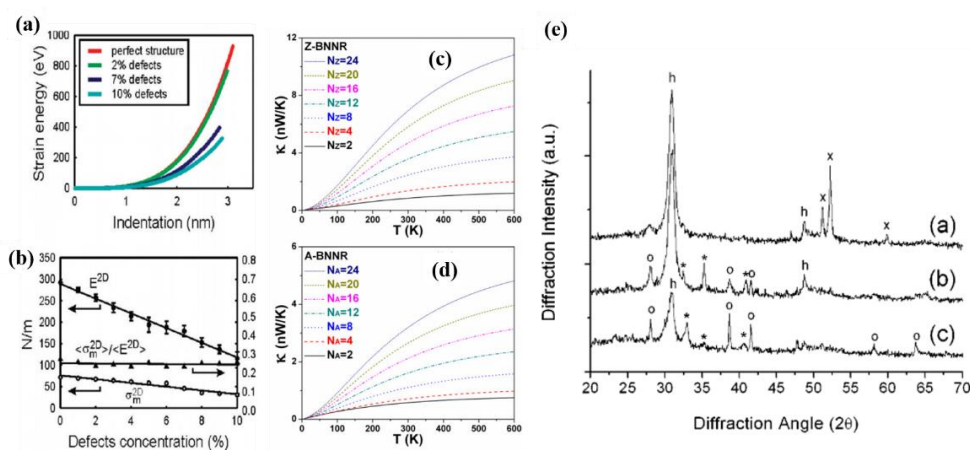


Figure 1.11 (a) The dependence of strain energy on the indentation depth of a h-BN sheet. (b) The breaking stress σ_m^{2D} , breaking strain ϵ_m^{2D} , and modulus E^{2D} as a function of the concentration of vacancies. (a-b) Reprinted with permission from [84]. Copyright (2010) American Chemical Society. (c), (d) The thermal conductance changes with the temperature with different widths of z and a h-BN nanoribbons. ©IOP publishing. Reproduced with permission from [85]. All rights reserved. (e) X-ray spectra for BN nanotube’s thermal stability before oxidation, heating to 700 °C and to 900 °C. Reprinted from [87], with the permission of AIP Publishing.

Unlike graphene, h-BN exhibits a very high bandgap of 6 eV, which can efficiently emits deep ultraviolet light [88]. This large band gap allows h-BN to be a high performance 2D insulator. Furthermore, a new form of hybrid h-BN-graphene material

with components ranging from pure h-BN to pure graphene was synthesized and characterized. [39] The scientist believed that this new material would promote the development of bandgap-engineered application in electronics and optics.

With all these exceptional properties, h-BN is considered to hold great potential in a wide range of device applications from high performance nano-electronics [10], deep ultraviolet emission [88], transparent membranes [86], to protective coatings [91].

A TMDC monolayer consists of three atomic layers, where one triangular lattice layer of metal atoms is sandwiched by two triangular lattice layers of chalcogen atoms (Figure 1.12). Therefore, the composition of TMDC is MX_2 . The stabilities and electronic properties of different TMDC monolayers have been investigated by Ataca *et al.* [90]. It is showed that MX_2 monolayer can exhibit various electronic properties from half-metallic, metallic to semiconducting, which depends on the combination of transition metal and chalcogen atoms as well as the structure of the 2D material. The study also demonstrated that the properties of TMDC thin films change with the number of layers.

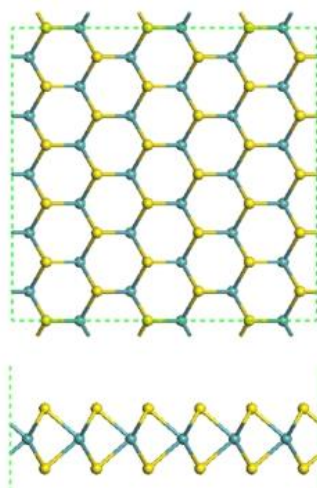


Figure 1.12 Atomic structure of TMDC monolayer from top view and side view. (Transition metal atoms are marked in green and chalcogen in yellow.)

This diversity in electronic properties of TDMC leads to many important implications such as electronics [91-92], photonics [93-94], spintronics [95], catalysts [96-98], *etc.* Single layer MoS₂ has been used in FET device with an oxide gate dielectric and the room temperature mobility was measured $> 200 \text{ cm}^2\text{V}^{-1}\text{s}^{-1}$, similar to that of graphene but with a very high on/off ratio up to 10^8 (Figure 1.13a). [25] Hua Zhang's group reported another very interesting application of MoS₂ as a phototransistor. [99] The phototransistor was based on single layer MoS₂ nanosheets and the photocurrent was examined. The study showed the fast generation of photocurrent, high stability, and superior photoresponsivity as compared to graphene-based transistors (Figure 1.13b, c).

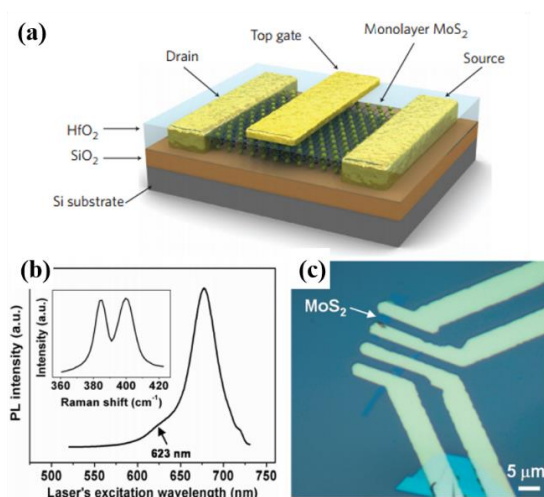


Figure 1.13 (a) Schematic of a FET device based on MoS₂ monolayer nanosheets. Reprinted by permission from Macmillan Publishers Ltd: Nature Nanotechnology ([25]), copyright (2011). (b) Photoluminescence (PL) spectra of MoS₂. Insert: Raman spectra. (c) Optical micrograph of MoS₂ based FET device. (b-c) Reprinted with permission from [99]. Copyright (2011) American Chemical Society.

Nowadays, with the increasing of interests in 2D materials, more and more investigations have been dedicated to understand their properties and realize their potential applications in both laboratory and industrial scales. As a high demand for these applications, the synthesis of high quality 2D materials in large area is essential.

1.2 The Synthesis of 2D Materials

With the rising of 2D materials, scientists have been enthusiastic in exploring an

effective method to synthesize high quality and large area 2D materials. Up to now, all these popular methods can be roughly divided into two major categories: top-down and bottom-up approaches. [100] The top-down synthesis of a 2D material is by separating the corresponding 3D layered materials into one or a few isolated atomic layers by either physical or chemical approaches. In contrast, the bottom-up method of 2D materials synthesis is to build a 2D crystal by stacking atoms mostly on a substrate, or in some cases, crystal planes further stack onto each other, leading to multi-layer 2D nano-films.

Among the methods of 2D materials, the exfoliation method, including mechanical exfoliation and chemical exfoliation, is the most popular and can be applied for the synthesis of nearly all 2D materials. Other methods, such as chemical vapor deposition (CVD), can be applied for the synthesis of certain 2D materials only. [67,101-103] Besides, plasma assisted method, and high-energy electron beam irradiation, also have been proposed. In this section, we will briefly introduce the most popular synthetic methods and simple discussions about their advantages and disadvantages will be given.

1.2.1 Mechanical Exfoliation

Proposed first by Novoselov and Geim in 2004 to fabricate freestanding graphene [1], mechanical exfoliation has been proven to work for many other 2D materials including

h-BN [14], TMDCs [104-106], and phosphorene [20,63]. The simple idea of this method is to break the weak van der Waals interaction between graphene layers by repeatedly applying the micro-mechanical cleavage method, or simply says, the scotch tape method. This straightforward method was able to yield one to a few layers of 2D crystalline flakes in crystal structure and properties eventually. As shown in Figure 1.14a, b, c, with the increasing times of cleavage, the graphene flake's thickness gradually decrease from ~ 3 nm to 0.8 nm. Similarly, other 2D materials like h-BN have also been successfully synthesized by mechanical exfoliation method. Pacileet *et al.* reported their synthesis of very thin sheets of h-BN in 2008 using this mechanical method [14]. As shown in Figure 1.14d, an AFM tapping mode topography image was used to determine the layer thickness of 2D h-BN sheet by the contrasting colors. Except for AFM, nowadays, optical microscopy and transmission electron microscopy (TEM) have also been employed to characterize the morphology of the samples and to distinguish the regions of different thickness.

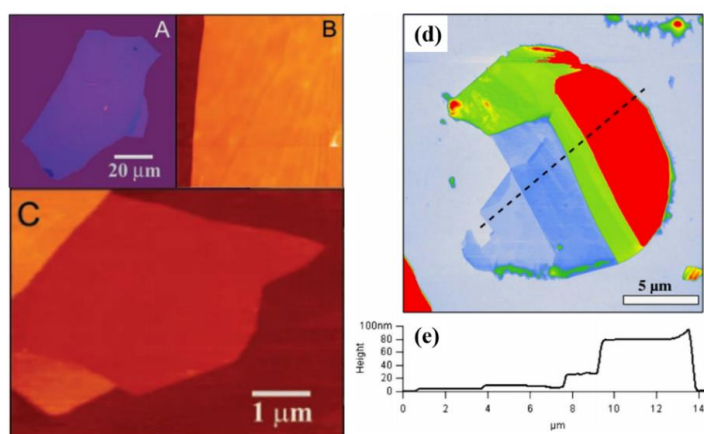


Figure 1.14 (a) Optical micrograph of a large few-layer graphene film on Si wafer. (b) AFM image

of the graphene film's edge with a 2 μm by 2 μm area. (c) AFM image of a graphene monolayer. (a-c) From reference [1]. Reprinted with permission from AAAS. (d) AFM image of h-BN nanosheets. (e) Height profile as a function of position marked with dashed lines in (d). (d-e) Reprinted from [14], with the permission of AIP Publishing.

Later, a few other researchers reported a new way of synthesizing large scale mechanically exfoliated 2D materials by using low-energy ball milling to increase the yield and the efficiency. Li *et al.* tailored ball milling conditions to produce shear force for high quality h-BN fabrication and milling agent was used to reduce the ball impacts and milling contamination. [107] Other improved fabrication methods such as plasma-assisted process, for mechanically exfoliation of 2D nanosheets have also been suggested.

Mechanical exfoliation method has the advantage to produce single-crystal flakes of high purity and high quality with few defects. The products are suitable for further exploration of the intrinsic properties of the 2D materials. However, with an extremely low yield, this method is not suitable for the mass production of 2D materials in industrial scaled applications.

1.2.2 Liquid-Phase Exfoliation

Liquid-phase exfoliation is another top-down exfoliation method to increase both the efficiency and size of the 2D materials. The bulk layered materials were firstly dispersed into a liquid solvents. Ionic in the solvents may intercalate into the layers of the 2D materials. With the assistance of sonication of sufficient intensity, the interlayer van der Waals bonding can be broken down and the layered 2D materials can be obtained after a centrifugation process.

By using the N-methyl-pyrrolidone (NMP) as solvent, solution of graphene with a concentration of ~ 0.01 mg/ml was produced after the exfoliation of graphite. [108] The interaction between these solvents and graphene is strong enough to exfoliate the 2D layers from graphite and stabilize them in the solution. The yield of monolayer graphene of ~ 1 wt% was reported and the high quality of the graphene sheets was demonstrated by X-ray, infrared, Raman spectroscopies and transmission electron microscope (Figure 1.15). Han *et al.* prepared mono- or few-layer h-BN nanosheets with this liquid-phase exfoliation method. [109] They found that with too much sonication, the crystal structure of h-BN nanosheets was broken down. Thus the duration and intensity of the sonication should be further optimized for both higher yield and quality.

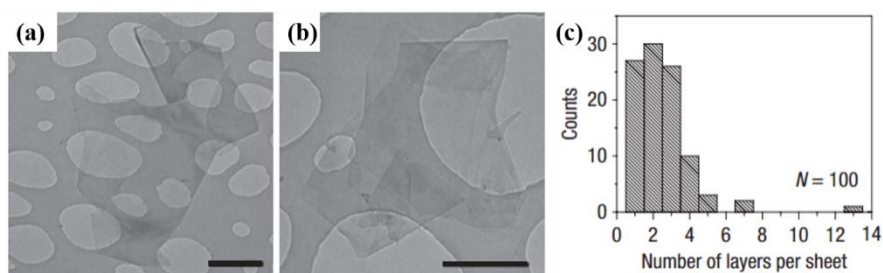


Figure 1.15 (a-b) TEM image of multilayer graphene nanosheets with both 500 nm scale bar. **(c)**

The number of graphene flakes vs the number of graphene monolayers per flake. Reprinted by permission from Macmillan Publishers Ltd: Nature Nanotechnology ([108]), copyright (2008).

Since the mechanical exfoliation is very inefficient for mass production, this solvent-assisted method has been investigated for large scale synthesis of many 2D materials such as graphene, phosphorene, TMDCs, and h-BN. [110-114] It is in general very quick and easy, and the yield is magnitudes higher in compare with that made by mechanical method. But the highest concentration, however, is no larger than 0.1 mg/ml of the solvent, which is still far from large production that is required for industrial production. Besides, the controlling of the number of the layers of the exfoliated nanosheets is complicated and need further improvements.

1.2.3 Chemical Synthesis

Chemical synthesis is another top-down approach with advantages such as low cost, low temperature, and easy process. One of the well-known techniques of this kind is graphite oxide (GO) reduction, which is employed to produce graphene thin films from GO. The approach combines the exfoliation method and chemical reaction. Firstly graphite was oxide to GO. Then the GO was exfoliated into GO solution in water. After centrifugation, graphene can be made by GO reduction at a high temperature. [115-117]

Nag *et al.*, in 2010, reported a new chemical synthesis of 2D h-BN nanomaterials involving the reaction of boric acid and urea. [118] This technique was able to produce 2D h-BN nanosheets with a majority of 1-4 layers. Furthermore, the author found that with the increase of the molar ratio of boric acid and urea (1:12, 1:24, 1:48), the number of the layers of the produced h-BN films reduces. As shown in the Figure 1.16a and b, with 1:12 and 1:24 boric acid/urea ratio, the layer number of h-BN is 6 and 8. While, in Figure 1.16c, with 1:48 boric acid/urea ratio, the layer number decreases to be 1 and 2. Thus the method was believed to be able to control the layer number of the produced h-BN.

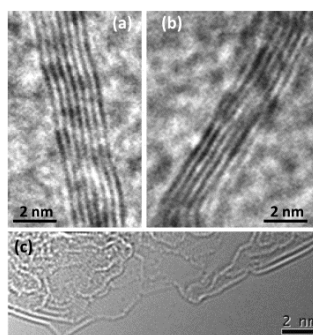


Figure 1.16 TEM images of few-layer BN nanosheets. The samples were prepared with different boric acid/urea mixture: **(a)** 1:12, **(b)** 1:24, and **(c)** 1:48. Reprinted with permission from ([118]). Copyright (2010) American Chemical Society.

Although this method is cost effective and easy to process, much of the chemical reactions contain uncertainties and therefore, enough defects are to be expected to degrade the materials' physical properties.

1.2.4 Chemical Vapor Deposition (CVD)

CVD is probably the most widely researched method for the synthesis of 2D materials and is the most likely method to be used for the industrial synthesis of high quality 2D materials. A standard CVD procedure includes four steps: i) Adsorption of the precursors from the atmosphere onto the substrate surface; ii) Decomposition of the precursors into the surface species; iii) Diffusion of the surface species or the desorption of these species; iv) Nucleation into small surface clusters and then continuously grow into large area domains. [119] The procedure can be illustrated clearly by the below Figure 1.17.

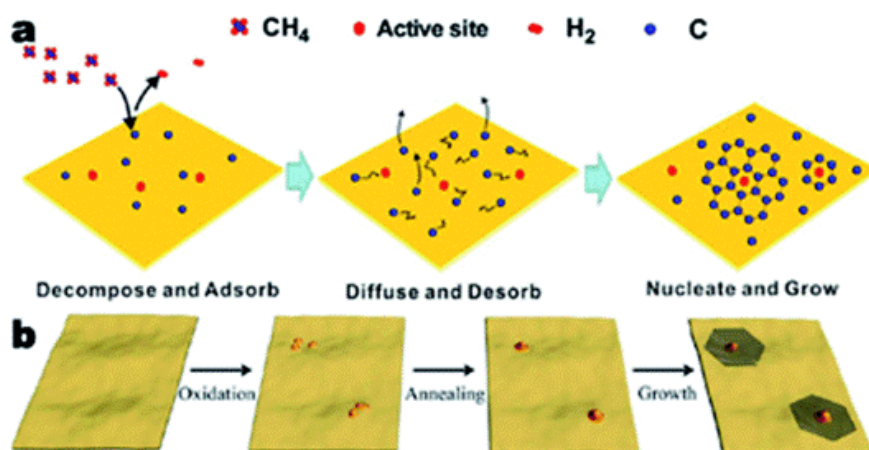


Figure 1.17 (a) Schematic of CVD growth process, where CH_4 feeds as precursor. Reprinted with permission from ([120]). Copyright (2012) American Chemical Society. (b) Schematic of the oxidation and reduction before CVD process. Reprinted with permission from ([121]). Copyright (2013) American Chemical Society.

Since 2009, when Li *et al.* reported their successful synthesis of uniform graphene films with high quality of the size of centimeter magnitude on copper substrate using CVD method, this technique has been recognized as one of the most important synthesis approaches for graphene and a vast number of material scientists have devoted into the field. [6] Up to now, very large area graphene film up to 30 inches has been synthesized. [36] Synthesis of ultrafast growth of single crystal graphene with a growth rate of 60 $\mu\text{m/s}$ has been realized. [122] Techniques of monolayer graphene to be fabricated on substrates of Cu, Ni, Pt, Ge, Ir, Ru, and Cu-Ni alloy with different kinds of precursors have been accomplished. [123-129]

Except for graphene, CVD growth for h-BN, TMDCs films is also widely investigated. As an example, Wen *et al.* showed an ultraclean and large-area single-layer h-BN growth on copper foils *via* low pressure chemical vapor deposition (LPCVD) method. [130] In Figure 1.18, the optical microscopy, scanning electron microscope (SEM), AFM, and TEM images all show a uniform and high quality h-BN single layer region. The selected-area electron diffraction (SAED) pattern in Figure 1.18e clearly indicates the high crystallinity of the measured material. The 0.55 nm thickness of the h-BN monolayer in Figure 1.18c corresponds well with reported data, further confirming the successful synthesis of monolayer h-BN of high purity and large size.

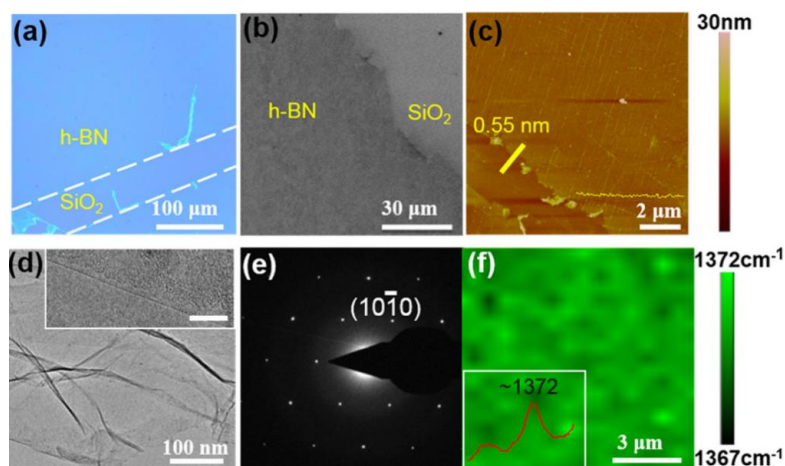


Figure 1.18 (a) Optical micrograph of monolayer h-BN nanosheets. The corresponding (b) SEM, (c) AFM, (d) low magnification TEM, (e) SAED pattern, and (f) Raman images of this h-BN single layer. ©IOP publishing. Reproduced with permission from [130]. All rights reserved.

Although high quality, high purity, and large area synthesis of 2D materials are attainable *via* CVD method, there are still many variables for controlling the morphology, crystallinity, and defects of the 2D films such as growth temperature, precursor pressure, substrate morphology, hydrogen partial pressure and so on. Further optimizations of these key factors are essential for the understanding of the growth mechanism and better development of the CVD process.

1.2.5 Summary of the Synthetic Methods

As mentioned above, mechanical and liquid-phase exfoliation, chemical synthesis, CVD methods are all commonly used for the synthesis of 2D materials. Here, after

quick overview, we make a comparison of these methods, taking graphene as an example. The details are all shown in Table 1.1. As it can be seen clearly, CVD method is of the highest potential to produce high quality graphene with large area and controllable number of layers at large scale and relatively low cost. This is also the reason why CVD, nowadays, is the most widely used way for 2D materials synthesis. As an advanced and complicated synthetic method, however, a comprehensive understanding on the mechanism of the entire CVD process is still lacking. Investigations and improvements are required for realizing its excellent properties in industrial applications. Beside, studies on CVD synthesis of phosphorene, one of the most promising 2D material, are still lacking probably due to its chemical activity. Thus its development needs more efforts and devotion.

Table 1.1 A comparison of various methods for the graphene synthesis, where SLG, FLG and MLG stand for single, few (*i.e.*, 2-10) and many layer (>10) graphene, respectively.

	mechanical exfoliation	GO reduction	SiC sublimation	Graphene intercalation	CVD
C source	graphite	GO	SiC	GO	hydrocarbon
Temperature of synthesis	room temperature	373K	1900-2300K	room temperature	~ 1300K
Thickness	SLG, FLG and MLG	SLG and FLG	SLG and FLG	SLG (> 90%)	SLG or FLG
Domain size	~100 μm	1-5 μm	< 1-10 μm	N/A	~10-1000 μm
Layer Size	~100 μm	~10 μm	1 cm	~20 μm	30 inch
Carrier mobility	very high (15,000 $\text{cm}^2/\text{V.s}$)	low (2-200 $\text{cm}^2/\text{V.s}$)	high (1100 $\text{cm}^2/\text{V.s}$)	low (300 $\text{cm}^2/\text{V.s}$)	high (5000 $\text{cm}^2/\text{V.s}$)
Quantity	small	Large	medium	large	Large
Condition of synthesis	on graphite surface	in solution	on SiC surface	In solution	on catalyst surface
Cost	Cheap	Very cheap	Expensive	Very cheap	Cheap
reference	1,131	132-134	135-139	140,141	37,38,142-144

Chapter 2. Literature Review

This chapter begins with a review of the literature on recent status of the CVD growth of graphene. Both experimental works and theoretical investigations of graphene CVD synthesis will be introduced in detail. The studies on the structure of newly emerged 2D material—phosphorene will then be presented, followed by a discussion of the CVD growth of phosphorene. Finally, we will give a brief conclusion of the research gap in the field of CVD growth of 2D materials and then propose our aims and objectives for this research work.

2.1 CVD Growth of Graphene

Recently, graphene CVD synthesis has provoked great interest because of its potential in electronic devices. Compared with other methods (Table 1.1), graphene CVD synthesis has many advantages: i) A relatively low temperature during the growth (*i.e.*, ~1000-1300 K); ii) Feasibility in synthesizing single-layer or few-layer graphene with very high quality; iii) Very large graphene domain size up to 100-1000 square inches; iv) Capability of being easily transferred onto other substrates for further processing; v) Available experimental parameters for experimental control.

Although the samples made by the mechanical peeling technique still have the highest

quality (indicated by the carrier mobility, see Table 1.1), it highly depends on the quality of the used graphite and unfortunately, with very limited efficiency. Thus, the scope for its further improvement is also limited. Especially, it is nearly impossible to synthesize wafer sized graphene by the mechanical peeling method. Liquid-phase exfoliation, as well as chemical synthesis, though, has much higher efficiency but the size of the produced 2D films is usually small and the quality usually not desirable enough. In contrast, with so many tunable experimental parameters (substrates, catalysts, precursors, temperatures, pressures, atmospheres, and so on), the quality of wafer sized CVD graphene is expected to be dramatically improved by proper experimental design. Thus below, along the history of CVD growth of graphene, we will discuss with details how far this research field has been reached and what is still waiting for exploration.

2.1.1 From Multilayer to Monolayer Graphene

Except for conducting polymers and carbon nanotubes, the earliest successful synthesis of graphene *via* CVD method was reported by Somani *et al.* in 2006, in which they grew planar few layer graphene on Ni substrates in a one-meter long quartz tube at 700-850 °C in the atmosphere of Ar. [145] The synthesis was simple, economical and reproducible. But with this cost effective thermal CVD method used for carbon nanotubes before, few layer graphene was able to be fabricated. As we can see in Figure 2.1a and b, with high resolution transmission electron microscope (HR-TEM), the interlayer

spacing of about 0.34 nm of graphite was clearly visible, matching well with graphite structure. Thus with this images, we are allowed to estimate that the graphene film contains about 35 layers. This research opens the possibility to controllably synthesize large area graphene films *via* CVD method. However, the role of the Ni substrate is not well understood and the quality of the produced graphene films is poor. More importantly, further optimizations need to be done to reduce the thickness of the graphene films for further electronic and optoelectronic applications.

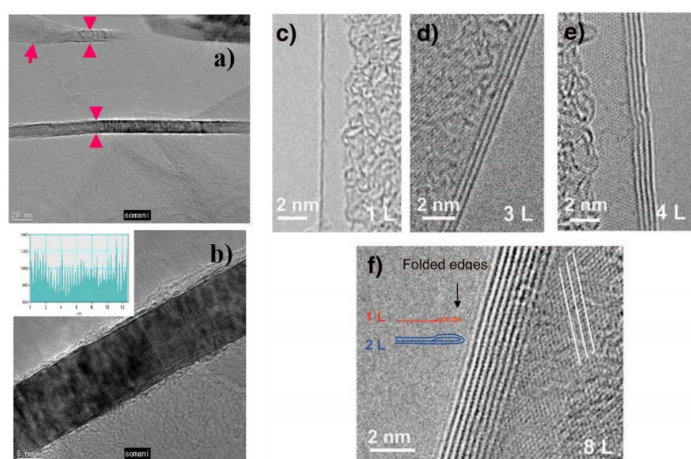


Figure 2.1 (a) HRTEM image of planar few-layer graphene (PFLG). (b) Image of the marked PFLG film in (a) by high magnification TEM. (a-b) Reprinted from [145], Copyright (2006), with permission from Elsevier. (c-f) Images of mono-, triple-, quadruple-, and octet-layer graphene films by high magnification TEM. Reprinted with permission from ([37]). Copyright (2009) American Chemical Society.

Among the scientists devoted into the field, Reina *et al.* succeeded to reduce the thickness to 1-12 layers in 2009. [37] The whole graphene sheet was synthesized on polycrystalline Ni film to a large size up to centimeter magnitude while the single- or bilayer regions were up to 20 μm . The TEM characterization of the graphene clearly shows the mono (Figure 2.1c), triple (Figure 2.1d), quadruple (Figure 2.1e), and octet-layer (Figure 2.1f) graphenes in the region. Later that year, Li *et al.* reported their exploration on the CVD synthesis of graphene by using copper substrates. [6] With the change of the substrate and optimization of other parameters, they were able to grow large-area graphene films with the size of centimeter order. Most importantly, the films were predominantly monolayer graphene with a large percentage (larger than 95%), where the single layer was even able to cross the copper surface steps and grain boundaries continuously. As shown in Figure 2.2a and b, only a few little spots are two or three layers of graphene. This could be one of the most important advances in the field of CVD synthesis of graphene since the sample is in the largest area, single layer graphene ever reported. In the study, they also proposed a transfer technique to arbitrary substrates where the electron mobility remains high at room temperature which would be of great advantage for the further electronic applications.

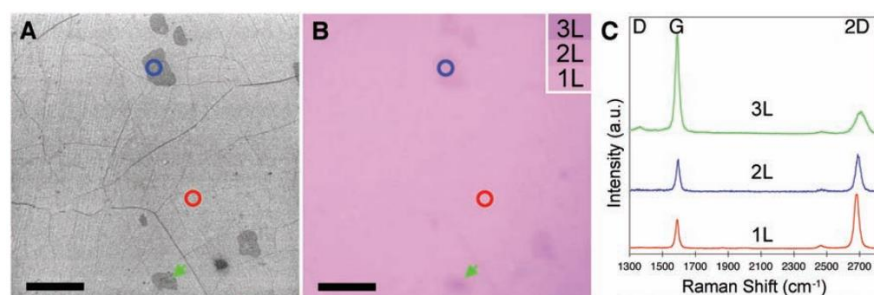


Figure 2.2 (a) SEM and (b) Optical microscope images of wrinkled graphene films on SiO₂/Si substrate. (c) Raman spectra of the marked regions. From [6]. Reprinted with permission from AAAS.

As for why they would succeed, the author claimed that it was because of the low solubility of carbon in copper that appeared to help. So far, many transition metals, rare earth metals, and noble metals have been used as catalyst/substrate for the graphene CVD synthesis including Ni, Co, Cu, Ru, Ir, Rh, Pd, Pt, Pt, *etc.* It was noticed that these metals show very different behaviors in graphene growth (see Table 2.1). Up to date, Cu is recognized the best catalyst for graphene synthesis. With the help of carbon isotope labeling, scientists demonstrated that because of the low solubility of carbon in Cu, the CVD growth of graphene with Cu as substrates is a self-limiting process, while on the contrary, resulting from the high carbon solubility, CVD growth of graphene with Ni as substrates is a diffusion followed by segregation and precipitation process.

[119,143]

Table 2.1 Graphene CVD growth on different transition metal substrates, where SLG, FLG and MLG stand for single-, few- (*i.e.*, 2-10) and multi-layer (>10) graphene, respectively.

	Temp.	C source	# of layers	carbon solubility	carrier mobility	Graphene domain size	References
Ni	> 800K	ethylene	Mainly MLG	high	N/A	N/A	146-148
Co	> 600K	hydrocarbon	Mainly MLG	high	N/A	(N/A)	149,150
Cu	1300K	hydrocarbon	Mainly SLG	low	~ 4000 (cm ² /V • s)	~1-1000 μm	6,143,151,152
Ru	1400K	CO or hydrocarbon	SLG & FLG	medium	N/A	~100 μm	125,144,154-158
Rh	1100K	hydrocarbon	SLG & FLG	medium	N/A	~ 0.1μm	159,160
Ir	1300K	hydrocarbon	SLG & FLG	low	N/A	~1μm	127,161,162
Pt	1100K	Hydrocarbon	SLG & FLG	low	N/A	~50 μm	163-165
Pd	1000K	ethylene	SLG & FLG	medium	N/A	N/A	166

With this understanding, scientists were able to go further. In 2010, Bae *et al.* reported a roll-to-roll production of graphene proceeding the synthesis, transfer and doping of graphene with larger area and high quality to make transparent conducting films for real applications. [36] With the help of ultra-large and flexible copper substrates, they successfully produced predominantly single-layer graphene films at the size of 30 inches *via* CVD method. The flexibility of the graphene films and copper substrates further enables the transfer of the products, as called roll-to-roll: they adhered the graphene together with the copper to the polymer supports, etched away the copper layers, and then released and transferred the graphene films to an arbitrary substrate.

This CVD method, as well as the following transfer process, is of great scalability and processability that we can even foresee the commercial production of such large area, monolayer graphene.

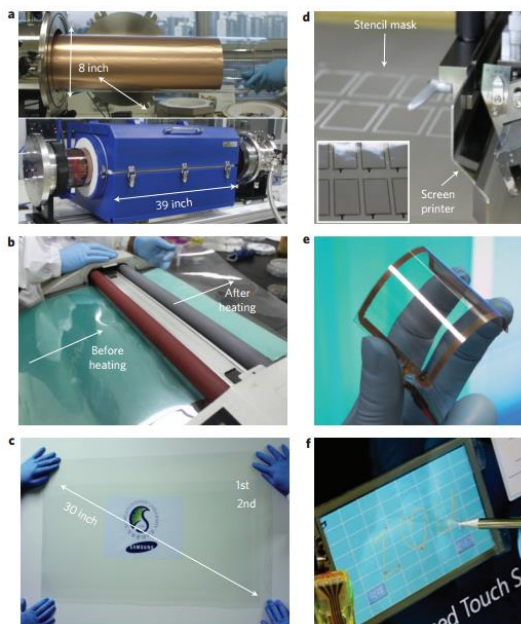


Figure 2.3 Process of the roll-to-roll production of large area graphene. **(a)** Copper foil used in a quartz reactor in the growth. **(b)** Graphene transfer at 120 °C. **(c)** A large area graphene on a PET sheet. **(d)** Screen printing on graphene film on a PET sheet. **(e)** A touch panel made with this graphene/PET film. **(f)** A real computer with this graphene-based touch panel. Reprinted by permission from Macmillan Publishers Ltd: Nature Nanotechnology ([36]), copyright (2010).

2.1.2 From Polycrystalline to Single Crystal Graphene

Although the reporters in the last section are already able to fabricate large area graphene single layers, the way to real industrial production is still challenging since the graphene films prepared are typically polycrystalline. This inevitably means a great degradation of quality, resulting from the defects along the grain boundaries. [167-169] An *et al.* once carefully studied the fundamental of the domain boundaries with TEM, HR-TEM, and dark field TEM techniques. [167] They found that, for the graphene films grown in the study, the misorientation angles of the domains were all between 11° and 30° , and the defects at the boundaries, as shown in Figure 2.4, were very likely to bind with adsorbates since usually there were dangling bonds in these defects. With this kind of observations, scientists believed that heavy contamination of adsorbates could happen at the grain boundaries and thus these grain boundaries in polycrystalline graphene may be the major cause for the inferiority of graphene's quality and properties.

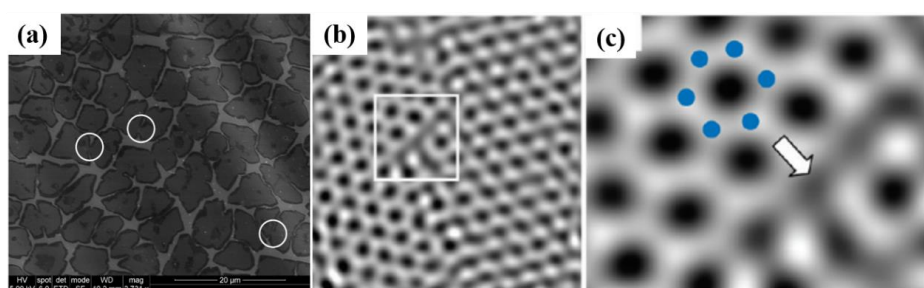


Figure 2.4 (a) SEM image of the merging graphene domains. (b) HR-TEM image of graphene with a highlighted domain boundary. (c) The highlighted boundary area in detail. Reprinted with permission from [167]. Copyright (2011) American Chemical Society.

Therefore, one of the main challenges for the production of large-area high-quality

graphene was raised to be the synthesis of single crystal graphene. Many efforts have been devoted. Among all, one of the common approaches is to modify the substrates to be with large grains. Normally, substrates with larger grains are with less grain boundaries and thus may produce larger area single crystals of graphene. [125] However, this kind of substrates is usually too expensive and should be infeasible for commercial production.

Another way scientists think of is to suppress the number of nucleation sites, which would allow each graphene domain to grow for a longer time period and with a larger space. Copper, usually, is the most favorite substrate for the synthesis of single crystal graphene because of the low solubility of carbon in copper, as well as the low catalytic power, which would undoubtedly reduce the nucleation sites, as we can see that most of the scientists like to use copper as their substrates/catalysts for the CVD growth of graphene. Besides, there are many factors that will affect the graphene nucleation including the hydrocarbon/hydrogen ratio, the growth temperature, the pretreatment of the substrates, and the pressure of the system. Vlassioug *et al.* investigated the role of hydrogen in CVD growth of single-crystal graphene on the Cu foils using methane as a precursor. [170] With a careful control of the hydrogen pressure, they were able to grow perfect single crystal graphene hexagons with a large domain size up to $\sim 10 \mu\text{m}$, while with the change of the hydrogen pressure, the graphene with such well-defined morphology and size could become irregular shaped incomplete bilayers. The authors believed that the function of hydrogen in the study is dual: it helps in the formation of

active surface bound carbon species as a cocatalyst and controls the grain size and shape as a terminator at the edge of the domains.

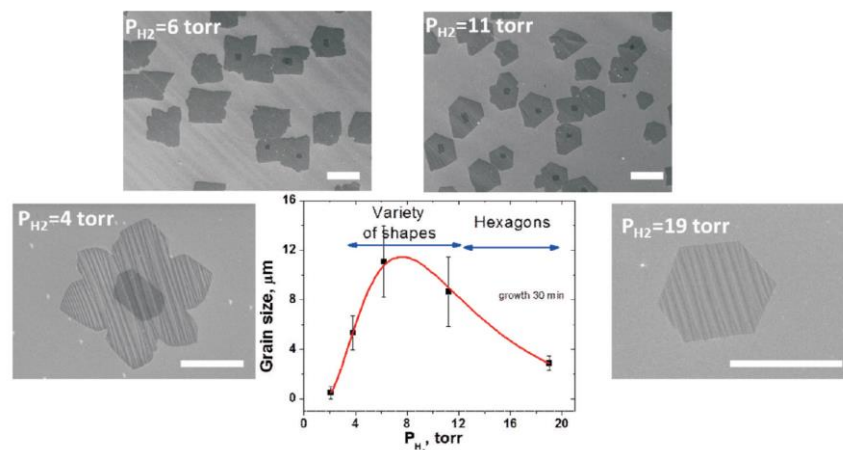


Figure 2.5 The dependence of average graphene domain size on the hydrogen partial pressure. SEM images of graphene domain shapes on different partial pressure of hydrogen. Reprinted with permission from [170]. Copyright (2011) American Chemical Society.

By controlling the hydrogen pressure also, in their simple one-step CVD method of growing graphene, Wu *et al.* further raised the temperature to 1090 °C, slightly above the melting point of Cu, and used a Mo or W substrate to prevent balling of Cu from dewetting. [171] With these optimizations, they successfully produced single crystal hexagonal domains of graphene single layer with a size of 200 μm (Figure 2.6 a, and b). At 1090 °C, the copper melts which means the liquid state of copper during the growth. It is interesting that, as in Figure 2.6b, the distribution of measured orientation angles matches the Lorentzian distribution, where the center point is 10.27°. This indicates the orientated alignment of the graphene domains. Although there is a ~ 9% deviation in the orientation angle which means if the graphene domains merged together,

there would be defects, it is still possible that two domains merge to become a single crystal domain of graphene if the alignment of these two domains could be perfect. This idea of the alignment of graphene domains provides a hint to the synthesis of wafer scale single crystal monolayer graphene. Later in 2014, Lee *et al.* realized the unidirectional alignment of graphene domains, using the hydrogen-terminated germanium (110) surface, to grow wafer-scale single-crystal graphene *via* CVD method (Figure 2.6c, d, e, and f). [126] The anisotropic two-fold symmetry of Ge(110) surface allows the perfect alignment of the graphene domains; The high barrier of graphene domain rotation, as well as the high formation energy for grain boundaries resulting from the pseudo-free-standing nature of graphene domains on H-terminated Ge surface, ensures the coalescence without grain boundaries, thus leading to the synthesis of a centimeter-size single-crystal graphene. In addition, the free-standing nature of the H-terminated surface enables the wrinkle-free growth of graphene films, further improving the quality of graphene for diverse electronic applications, and also allows the facile etch-free transfer of the graphene films because of the weak adhesion. This is another big step to the commercial realization of single crystal graphene for various applications.

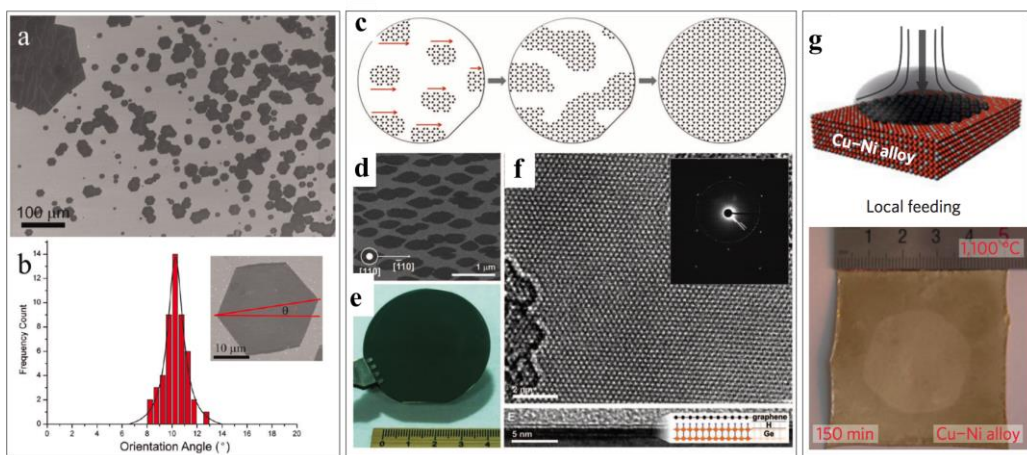


Figure 2.6 (a) SEM image of various graphene domains. (b) Frequency counts for different orientation angles with hexagonal domains. Inset: definition of the orientation angle. (a-b) reprinted with permission from [171]. Copyright (2012) American Chemical Society. (c) Schematic of single-crystal graphene monolayer growth with the merging of aligned seeds. (d) SEM image of graphene domains during growth. (e) Graphene on a Ge/Si substrate. (f) HR-TEM image of single crystal graphene (SCG) monolayer. Inset: SAED pattern. (c-f) From [126]. Reprinted with permission from AAAS. (g) Photograph of large area SCG on a Cu-Ni substrate. The local feeding is presented above. Reprinted by permission from Macmillan Publishers Ltd: Nature Materials [172], copyright (2015).

Soon in 2016, Wu *et al.* developed a new strategy for synthesizing wafer-scale single-crystal monolayer graphene with CVD method by locally feeding carbon precursors to a certain position of optimized $\text{Cu}_{85}\text{Ni}_{15}$ surface (Figure 2.6g). [172] Most importantly, the technique is able to speed up the normal graphene CVD synthesis. Before then, the old methods of growing centimeter-sized single-crystal graphene cost about 12 hours, while in this study, the authors succeeded to synthesize a ~1.5-inch-large single-crystal graphene in 2.5 h. It is known that growth of graphene on Cu is surface-mediated

because of the low carbon solubility, while the poor catalytic power limits the graphene growth. In contrast, Ni is too powerful as catalysts and its high carbon solubility together, determines the graphene growth strategy on Ni should be mainly the segregation of the dissolved carbon, which leads to the formation of graphene multilayers. While in this study, taking both advantages, the authors were able to boost the growth rate since the local precursor feeding ensures the nucleation only at the desired site and most importantly, the Cu-Ni alloy enables the isothermal segregation.

Besides the above optimizations, many researchers began to realize the important role of oxygen in the CVD growth of graphene. [121,123,173] Gan *et al.* succeeded to obtain copper nanoparticles of proper size by the oxidation and reduction of copper surface. [121] In this way, they were able to control the nucleation density by controlling the oxidation process and thus accomplished the control of the graphene domain size. Hao *et al.* found oxygen enabled the growth of wafer-scale single-crystal graphene. [123] They claimed that oxygen first passivated the Cu surface active sites to decrease the nucleation sites, and then accelerated the graphene growth by modifying the growth kinetics into the diffusion-limited regime. However, how it is able to modify the growth kinetics remains unknown, and a deeper understanding of the role of oxygen in the CVD growth of graphene is still needed. To further explore the underlying reasons, we will first give a review of the current theoretical studies of graphene CVD growth in the next section.

2.1.3 Mechanistic Insight into the Graphene CVD Growth

Due to the great potential of synthesizing high quality graphene with large area and inadequate understanding of the experimental design, the mechanism of graphene CVD growth has drawn considerable attention recently. In a CVD experiment, the graphene growth can be briefly divided into three sections: i) initial stage; ii) nucleation stage and iii) the expansion of graphene islands.

In stage i), carbon precursors (*i.e.* C_xH_y) [6,136,174] decompose into carbon monomers or dimers on transition metal catalyst substrates. For transition metals with various stable carbide phases (e.g., Ni, Fe, Co...), [75] carbon atoms could dissolve into the substrate at high temperature and later precipitate to the surface after cooling down. With transition metals that have no carbide phase (e.g., Cu, Au, Ir...), the dissociated carbon atoms could only diffuse on the catalyst surfaces. [176,177]

When carbon monomers or dimers saturate the transition metal substrate, graphene nucleation begins. In this stage ii), carbon monomers or dimers will aggregate and form carbon clusters on the catalyst surface, while some of them with relatively low stability will decompose back into monomers or dimers. Once reaching a critical size, carbon clusters continue to grow and stage iii) starts.

Gao *et al.* examined the structures and formation energies of $C_2\sim C_{24}$ clusters with relatively high stability on Ni(111) surfaces. [178] Taking C_{13} isomers as an example (Figure 2.7k), they were surprised to find that structures, like C_{13-3} in this figure, which contain pentagons are always more favorable. They assumed that this was because sp^2 carbon network are energetically more stable, and thus the reduction of the non- sp^2 carbon number would be energetically more preferred. The incorporation of pentagons will result in a bowl-like shape that forms a cluster island on the transition metal whose edge interacts strong with the transition metal. Similarly, Yuan *et al.* theoretically proved that a core-shell structured C_{21} cluster (Figure 2.7c) is of higher stability than the pure hexagonal structure (Figure 2.7d), which was first suspected to be the experimentally observed uniformed carbon clusters with a diameter of 1 nm. [179,180] Further experimental and simulation works confirm the validation of their finding as shown in Figure 2.7e-j.

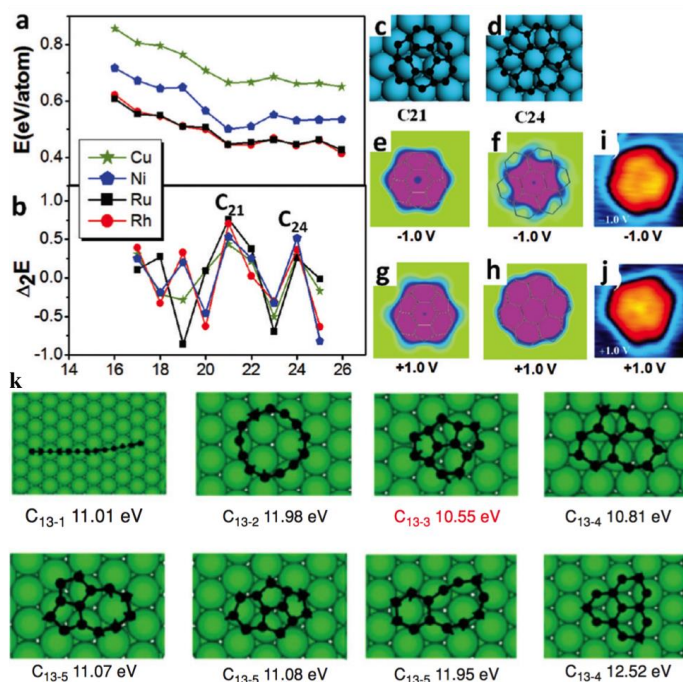


Figure 2.7 (a) Formation energy and (b) second derivatives of the carbon clusters on the Ni(111), Cu(111), Ru(0001), and Rh(111) surfaces. (c) C_{21} and (d) C_{24} clusters on Rh(111). Simulated (e-h) and (i, j) experimental STM images of carbon clusters found during graphene growth. (a-j) Reprinted with permission from [179]. Copyright (2012) American Chemical Society. (k) Several stable C_{13} clusters and their formation energies on Ni(111) surface. Reprinted with permission from [178]. Copyright (2012) American Chemical Society.

On the basis of the above work on carbon cluster evolution, Gao *et al.* further considered the graphene nucleation both on terrace and near a step (Figure 2.8 a, and b). [181] As shown in Figure 2.8c and d, there is a structure transformation from a carbon chain to a sp^2 carbon network at $N=12$ and 10 for carbon on terrace and near a step respectively. Further comparing the energies, nucleation barriers, nucleation size and other crucial parameters of C clusters on the terrace and near a step, it was indicated

that nucleation near a step is preferred, which is correspondent with the previous experimental observations.

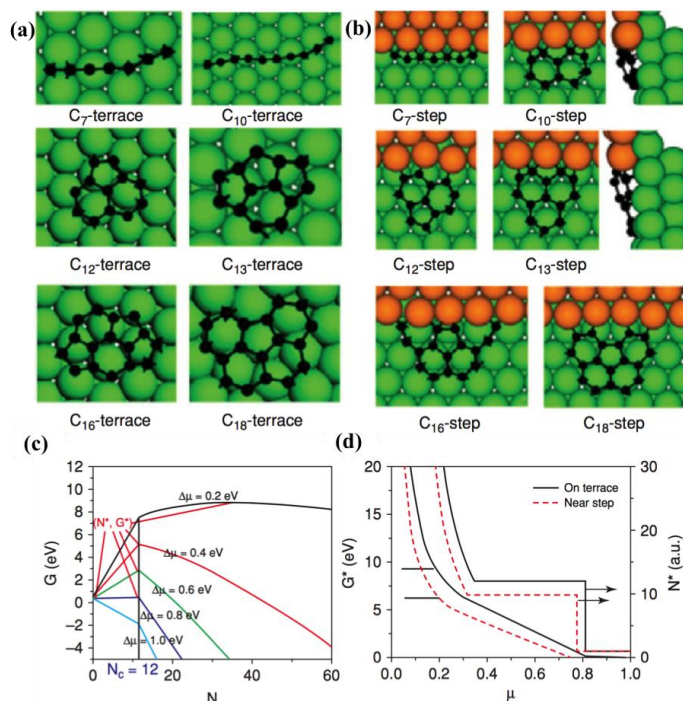


Figure 2.8 Atomic structures of C_N clusters on (a) terrace and (b) step of Ni(111) surface. (c) The dependence of carbon cluster's Gibbs free energy on the cluster size. (d) The dependence of nucleus size and nucleation barrier on chemical potential difference of carbon in graphene and feedstock. Reprinted with permission from [181]. Copyright (2011) American Chemical Society.

After nucleation, the graphene continues to expand as the feedstock keeps decomposing and the carbon monomers or dimers attach to the edge of the nuclei. [182] Thus, the edge of graphene becomes the new highlight as the growing front. The growing rate and the morphology of graphene are all affected by the edges. Gao *et al.* investigated the edge reconstruction of graphene on transition metal surface by examining many typical graphene edges on different kinds of transition metal surfaces (Figure 2.9a-h).

[183] They found that transition metals significantly passivated the graphene edges since formation energies for various edges on transition metals are much lower than those in vacuum (Figure 2.9i). It is interesting that the way how graphene edges reconstruct on transition metals is quite different from that in vacuum. In vacuum, zigzag (zz) edge is usually reconstructed into pentagon-heptagon (5|7) pairs while armchair (ac) edge tends to remain unchanged. However, zz edge seems quite stable that no reconstruction is going to occur on transition metals according to the formation energies, while ac edge on transition metals is energetically unfavorable and will reconstruct to a new structure (Figure 2.9h) with dangling carbon atoms on Co(111) and Ni(111). Besides, the equilibrium shape of graphene on transition metals will also be affected on the edge reconstruction of graphene. Further investigation by Shu *et al.* indicates that the Cu atom on Cu(111) surface as passivation media shown in Figure 2.9j, k, and l, could greatly lower the barrier of adding a carbon atom onto the edge.

[184] This is believed to be the reason why ac edge grows faster than zz edge, which corresponds well with the experimental phenomenon that zz edge is the dominating edge of the equilibrium graphene domain. On the basis of these considerations, they wrote the fomula for the growth rate of graphene derived from carbon nanotube [185] as

$$R(\theta) = (4/\sqrt{3}) \times R_{ac} \times \sin(\theta) + 2 \times R_{zz} \times \sin(30^\circ - \theta) \quad (2.1)$$

Then the morphologies of the growing graphene domains can be finally obtained by kinetic Wulff construction (Figure 2.9m, n). Adding all the details, Artyukhov et al. finally gave a comprehensive picture of the step-flow crystal growth of graphene. [186]

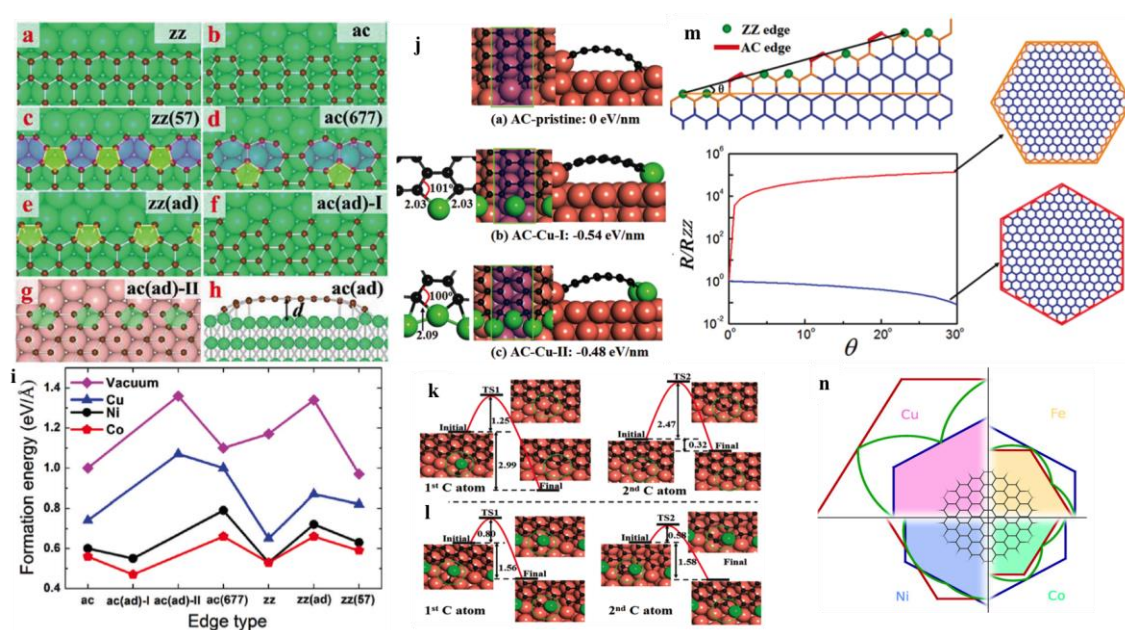


Figure 2.9 (a-h) Atomic structures of various kinds of graphene edges. (i) Formation energy of different edges types in vacuum and on different surfaces. (a-i) Reprinted with permission from [183]. Copyright (2012) American Chemical Society. (j) Atomic structures of ac edges on Cu(111) surface. Adding two carbon atoms into (k) ac edge and (l) Cu-terminated ac edge on Cu(111) surface. (m) Structure of graphene edge with an arbitrary tilt angle. (j-m) reprinted with permission from [184]. Copyright (2012) American Chemical Society. (n) Wulff construction of graphene with different edges on different metals. [186] Copyright (2012) National Academy of Science.

For the growth of graphene domain, one of the most important issues raised is the orientation of the synthesized graphene layer which determines the later merging of the

domains, the defects along the grain boundaries, and the quality of the final graphene films. Zhang *et al.* made a deep investigation into the determination of the orientation of graphene during the CVD growth. [187] Figure 2.10e shows the optimized adhesion energy between the graphene wall and the copper surface, where at $\theta = 0^\circ$, it reaches the largest end as 35 meV, which is much smaller than the thermal activation energy at 1000 °C. While Figure 2.10f, shows the strong interaction between graphene edge and copper substrates. Thus, the study demonstrated that the graphene wall-substrate interaction is weak which is not able to determine the orientation of the graphene domain, while the graphene edge-substrate interaction is large enough to affect the orientation. Because of the high rotation barrier, it is reasonable to assume that the orientation determination of graphene depends on the graphene edge-substrate interaction at the early stage of the growth of graphene and once the graphene grows to a certain size, the orientation is fixed. On the basis of this theory, the authors were able to explain many experimental phenomenon and strategies for the synthesis of high-quality graphene was proposed.

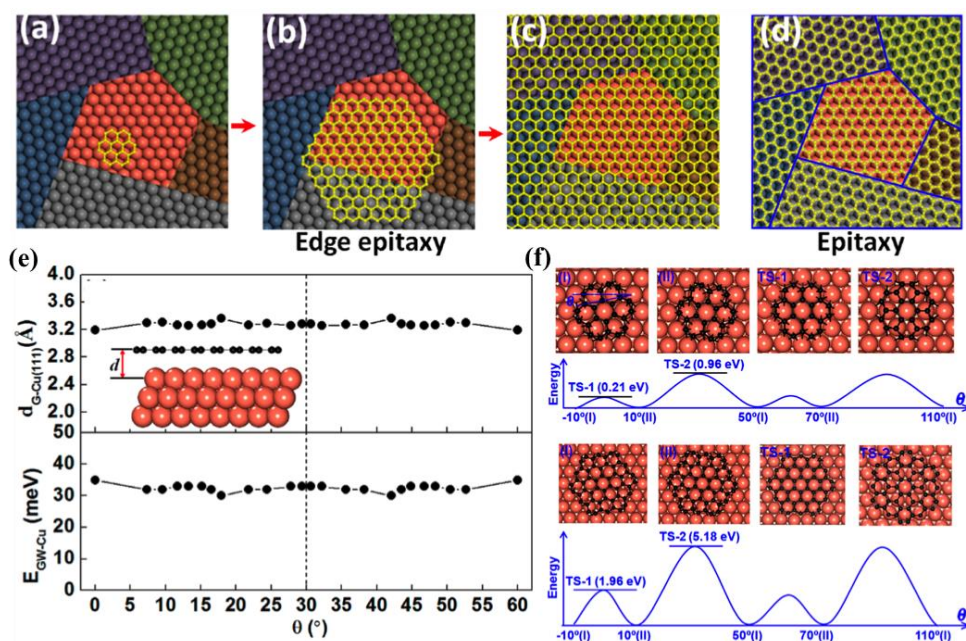


Figure 2.10 (a–c) Edge epitaxial growth of SCG on polycrystalline substrate. (d) Epitaxial growth of graphene on a polycrystalline surface to form polycrystalline graphene film. (e) Distance between graphene and copper surface, and the dependence of binding energy on the rotation angle. (f) Energy evolution of C_{24} and C_{54} on copper surface with rotation. Reprinted with permission from [187]. Copyright (2012) American Chemical Society.

So far, to our limited knowledge, we have reviewed recent progress on the CVD synthesis of graphene and presented some fundamental understanding of its mechanism. Although the CVD growth of graphene has attracted focused attention for several years, the controlling of the quality of the produced graphene, the efficiency and scalability of the synthetic methods, and a deeper understanding of the CVD growth mechanism still need scientists' efforts.

2.2 Structure of Phosphorene

Phosphorene has attracted enormous attention since 2014, especially for its outstanding electronic, mechanical and thermoelectric properties as mentioned above, which might all result from its unique anisotropic structure. Phosphorus atom has one more valence electron than carbon, and thus in most of the phosphorus structures, phosphorus atoms are sp^3 bonded--three σ bonds to another phosphorus atom and one lone electron pair. The existence of this lone electron pair leads to the deformation of the origin configuration of sp^3 and the bond angle varies in a range (from about 90° to 109.5°) as well as the bond length (from about 2.2 \AA to 2.3 \AA). This variation of the two parameters brings about the diversity of phosphorene isomers.

Only two months after the experimental synthesis of monolayer black phosphorene, in May 2014, Zhu *et al.* was able to publish their prediction of a previously unknown phase of phosphorus and named it as blue phosphorus which shares the black phosphorus' layered structure and high stability. [188] As shown in Figure 2.11, they saw the black phosphorus single layer as armchair ridges in the side view (panel a). By flipping some of the phosphorus atoms from a "down" to an "up" position without changing any bond length or bond angle (panel c), they converted the armchair ridges to zigzag ridges which is just the side view of blue phosphorus single layer (panel b). Thus the transformation of the two phases of phosphorus is just the introduction of dislocation. Interestingly, blue phosphorene is structurally very similar with silicene

and germanene, and unlike black phosphorene, it exhibits isotropic structure. Further computational calculations have been done to verify the stability of this new phase and also unveil the electronic properties. Their results indicated a 2 eV indirect band gap of the blue phosphorus monolayer, and that the band gap is inversely proportional to the number of the layers and the in-layer strain. They also suggested that exfoliation could be the possible synthesis method for monolayer blue phosphorene since the interlayer interaction of blue phosphorus is even weaker than that of black phosphorus.

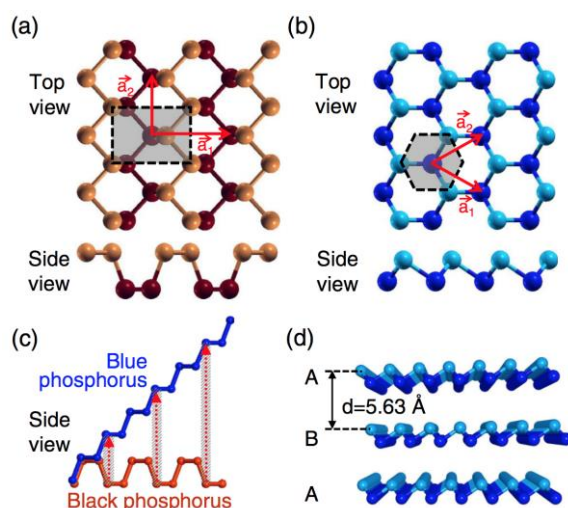


Figure 2.11 Atomic structures of (a) black and (b) blue phosphorenes. (c) The transformation from black phosphorene to blue phosphorene by dislocations. (d) Distance of AB stacked blue phosphorus layers at equilibrium. Reprinted with permission from [188]. Copyright (2014) by the American Physical Society.

Very soon, Guan *et al.* proposed two another new phases of phosphorus layers, named as γ and δ -P both with relative stability and the old two phases were then also called as

α -P (black) and β -P (blue) (Figure 2.12). [189] The theoretical calculations showed that the cohesive energies of β -, γ -, and δ -P are 0.04, 0.09, and 0.08 eV per atom lower than that of the most stable phase of phosphorus— α -P. The fundamental band gaps of α -, β -, γ -, and δ -P, based on density functional theory (DFT) calculations, are 0.90, 1.98, 0.50 and 0.45 eV, respectively. Later they talked about the connection between the different phases and argued that it would be valuable in assembling heterostructures with metallic and semiconducting regions. To further verify their predictions of the isomers, they presented a scheme to categorize the structure of α -, β -, and γ -P by a tiling model, which in return predicted another new phase named as θ -P. [190]

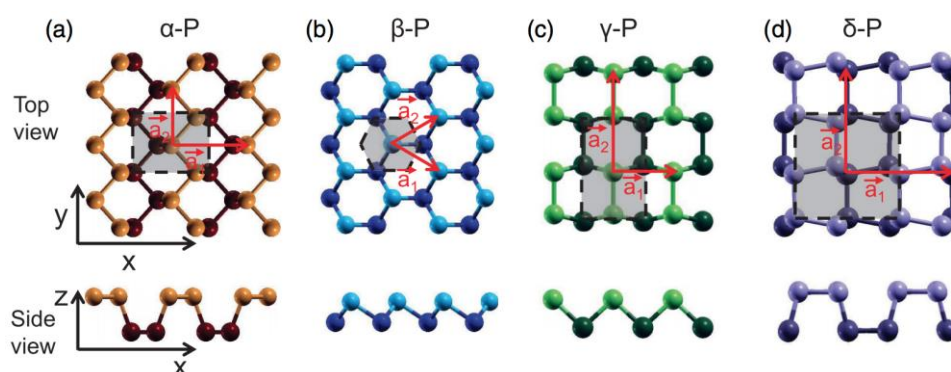


Figure 2.12 (a-d) Optimized atomic structures of α -P, β -P, γ -P, and δ -P phosphorenes. Reprinted with permission from [189]. Copyright (2014) by the American Physical Society.

A year later in 2015, Zhao *et al.* published their work about another prediction of a new 2D phosphorene, which they call red phosphorene. [191] As we can see in the below figure, the new red phosphorene is a combination of segments of the previously proposed black and blue phosphorenes. The theoretical study indicated that the red phosphorene is with great dynamic and thermodynamic stability. The cohesive energy of red

phosphorene is just 0.003 eV higher than black phosphorene, even 0.003 eV lower than blue phosphorene. The band gaps of this new phase of phosphorus based on Perdew-Burke-Ernzerh (PBE) and Heyd-Scuseria-Ernzerhof (HSE) calculations are 1.19 and 1.96 eV, respectively. Very recently, a new work about the phosphorene isomer prediction was reported by Zhang *et al.* [192] They searched in a broad range of monolayers composed of Group 15 elements (phosphorene, arsenene, antimonene, bismuthene). Among all the 2D materials talked about, there were 9 phosphorene isomers with 5 typical honeycomb (α , β , γ , δ , ϵ) and 4 non-honeycomb (ζ , η , θ , ι) structures. However, except for the 4 widely reported phases (α , β , γ , δ), some of the other fancy structures are not that favorable as to the stability.

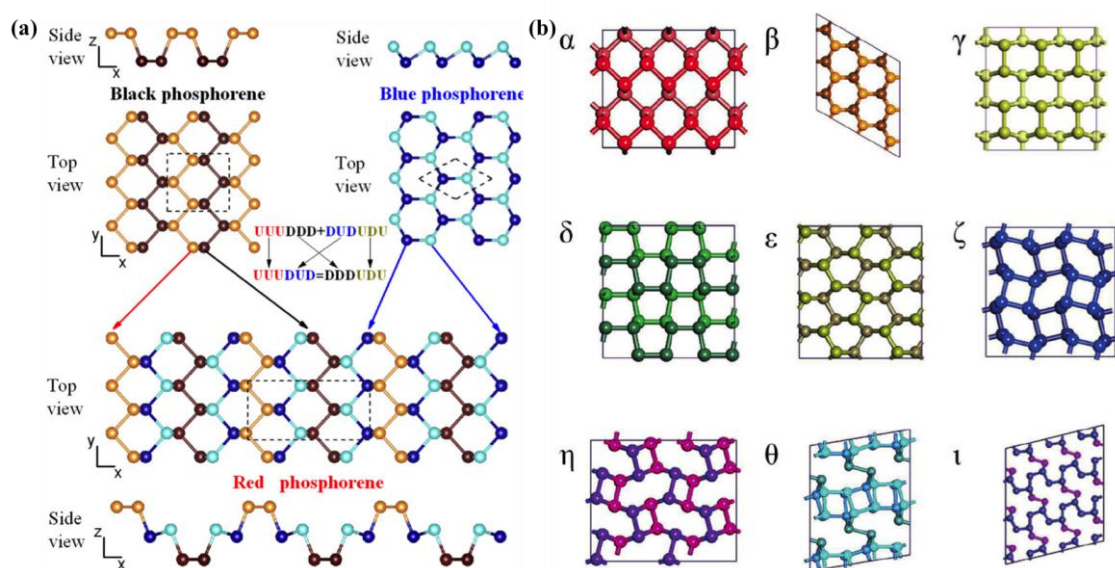


Figure 2.13 (a) Atomic structures of black, blue, and red phosphorenes. ©IOP publishing.

Reproduced with permission from [191]. All rights reserved. (b) Atomic structures of phosphorene isomers with 5 hexagonal structures (α , β , γ , δ , ϵ) and 4 non-hexagonal structures (ζ , η , θ , ι). From reference [192], copyright (2016) by John Wiley & Sons, Inc. Reprinted by permission of John

Wiley & Sons, Inc.

Although most of the above phosphorene isomers are currently just being discussed at the theoretical level, the calculations by DFT, molecular dynamics (MD) and Monte Carlo simulations (MC) all indicate the comparable stability and feasibility of the growth of these new phases. Considering the large range of band gap of these isomers and the unique properties, it is worthwhile for the exploration of new phosphorenes. However, most of the isomer predictions of phosphorene, to date, are not systematic but only random guesses come up by intuitions. A global searching method is not available until now.

2.3 Synthesis of Phosphorene

As mentioned before, band gap, as well as many other properties of phosphorene highly depends on the quality of the products, for example the thickness of the phosphorus films. Therefore, it is of great importance to study the synthesis of phosphorene and to deeply explore the mechanism of the phosphorene growth.

However, up to now, most of the experimental fabrications of phosphorene are exfoliations with limited efficiency. Very soon after Li *et al.* first synthesized few-layer black phosphorus crystals for FET devices, [63] single-layer black phosphorene was

isolated by Liu *et al.* via mechanical exfoliation of commercial bulk black phosphorus. [20] As shown in Figure 2.14a, phosphorene monolayer with thickness of ~ 0.85 nm is clearly seen in the AFM image. For the protection of the single layer phosphorene from reacting with the environment, it is then covered by polymethylmethacrylate (PMMA) for the further study of the properties. With the monolayer product, the pronounced photoluminescence (PL) peak around 1.45 eV revealed its band gap first time experimentally (Figure 2.14b). Later on, some improvements have been made to develop the technique. Lu *et al.* further processed the samples fabricated by the mechanical exfoliation with Ar^+ plasma to get a monolayer phosphorene as used in graphene and MoS_2 synthesis. [193] The thickness of phosphorene was confirmed by the optical contrast of AFM and the Raman shifts indicated the decreasing of the layer number as shown in Figure 2.14c and d. This method is promising as it provides a way of improving the quality of the produced phosphorenes by thickness control. But the requirement of the plasma for thinning process is not scalable and costs much, and thus is only feasible in the labs.

To improve the efficiency, liquid-phase exfoliations have been applied to grow single layer phosphorenes. Black phosphorus was exfoliated in NMP for 24 h. [194] With the help of ultrasonication, the dispersions were further centrifuged to collect the nanosheets. The Raman shifts of the samples indicated that these were not single layer phosphorenes while AFM and the height-profiling reveals a thickness of 3.5 – 5 nm, which suggested that the nanosheets are composed of 3 to 5 layer phosphorene (Figure

2.14e, f, and g). This study presents a new possible way for the fabrication of thin BP films on large scale for a wide range of applications. However, the quality of the products need further improvements.

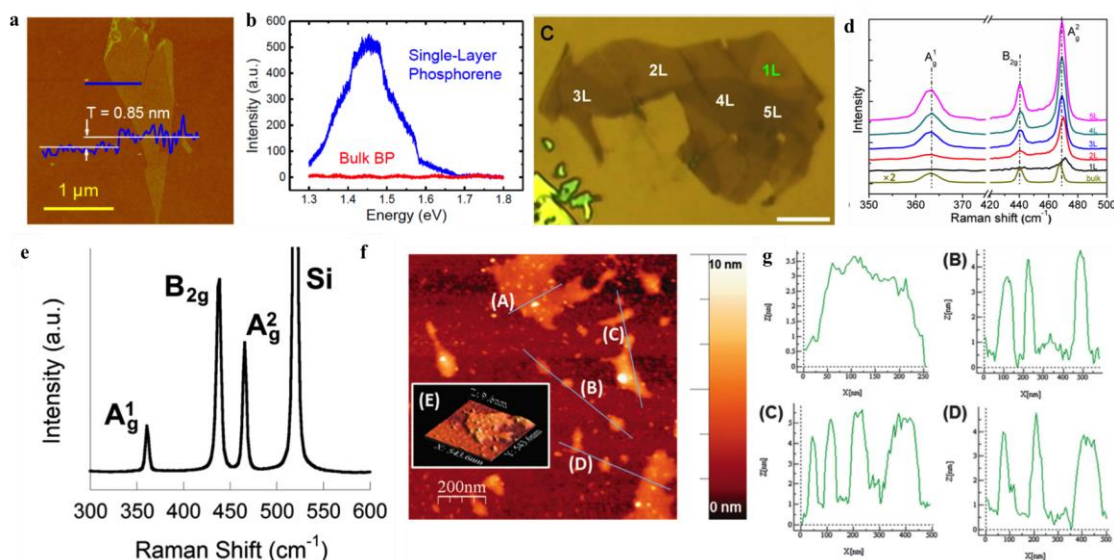


Figure 2.14 (a) AFM image of phosphorene monolayer. (b) PL spectra of both phosphorene monolayer and bulk BP. (a-b) Reprinted with permission from [20]. Copyright (2014) American Chemical Society. (c) Optical micrograph of phosphorene films with one, two, three, four, and five layers. (d) Raman spectra of phosphorene films with different layers. (c-d) Reprinted with permission of Springer from [193]. Copyright (2014) Tsinghua University Press and Springer-Verlag Berlin Heidelberg. (e) Raman spectrum of thin phosphorene film. (f) AFM image of phosphorene thin film. (g) Height profiles of phosphorene films marked in (f). Reproduced from reference [194] with permission from The Royal Society of Chemistry.

All the above methods are top-down approaches, facing the problems of low efficiency and low product quality. As the development of wafer-scale single-crystal methods *via*

CVD growth on transition metal surfaces has enabled the large-area high-quality synthesis of graphene as well as other 2D materials, experimental scientists are making great efforts to explore the CVD synthesis of phosphorene. Very recently, two of them made great progress. Smith *et al.*, in 2016, demonstrated a CVD type growth of large area 2D BP films with average areas $> 3 \mu\text{m}^2$ and thickness of 4 layers from red phosphorus on a silicon substrate at 600°C (Figure 2.15a). [195] Almost at the same time, Zhang *et al.*, in 2016, reported a molecular beam epitaxial growth of blue phosphorene single layer on Au(111) by using black phosphorus as a precursor at 230°C [196]. Blue phosphorene has only been theoretically predicted as a stable isomer of BP recently but never found in real experiments. This report, however, not only confirms the existence of this specific phase of phosphorene, but also at the first time develops a method to synthesize monolayer blue phosphorene with large area and high quality. As shown in Figure 2.15b, we can clearly see the simulated STM image of blue phosphorene corresponds well with the experimental STM image and a band gap of 1.1 eV is also observed.

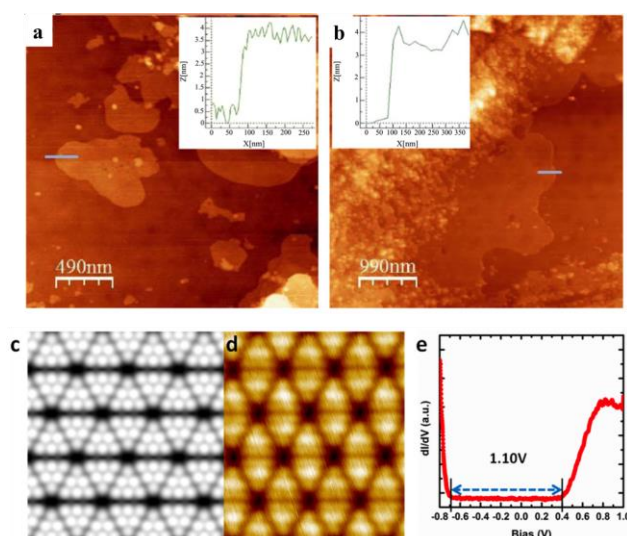


Figure 2.15 (a-b) AFM image of few-layer BP with different area size. Inset: height profile. **(a-b)** ©IOP publishing. Reproduced with permission from [195]. All rights reserved. **(c)** Simulated STM image of the modeled BLP. **(d)** Experimental STM image of BLP. **(e)** dI/dV curve of BLP single layer film. **(c-d)** Reprinted with permission from [196]. Copyright(2016) American Chemical Society.

These experimental results fully support the potential for large-area high-quality phosphorene synthesis by CVD method and the ongoing aiming at the production of phosphorene for a variety of practical applications. However, the investigation on the CVD synthesis of phosphorene is just beginning. For the wafer-scale high-quality single-crystal synthesis of phosphorene, both experimental and theoretical works are further expected.

2.4 Research Gap and Motivation

As stated above, experimental approaches have been able to successfully synthesize monolayer graphene with a large size of 30-inch *via* CVD method, and following a convenient transfer process, the commercial production of large-area single-layer graphene can be expected. With further optimizations, growth of centimeter-sized single-crystal graphene has been realized.

However, previous works on the growing of uniform single-crystal graphene focus on

the reduction of nucleation sites to control the domain size and then lower the defect concentration while this suppression of nucleation usually comes with the reduction of the feedstock concentration which would obviously lower the growth rate of these CVD methods. Typically the growth of a wafer-size single-crystal graphene would take a long growth time of hours to days. [121,123,197] Even the fastest CVD synthesis of graphene on the Cu-Ni alloys to date is with a growth rate of only 4.23 $\mu\text{m/s}$. [172] Compared with the CVD growth rate of carbon nanotubes, there is still much room to improve the speed of graphene CVD growth. Besides, the role of oxygen in the graphene CVD growth has been realized to be of great importance. [121,173] However, the increasing of growth rate is still very limiting in these investigations, 100 times slower than that has been achieved in the growth of carbon nanotube. And the mechanism how oxygen can accelerate the graphene growth is mysterious.

Thus, with the observations of our experimental collaborators, we are going to explore the mechanism of how oxygen modifies the growth kinetics and then greatly increases the growth rate of graphene. By theoretical calculations, we will first simulate the shape evolution of the CVD graphene domain to explore the mechanism that governs this process with a continuous supply of oxygen. Further with the understanding of the mechanism, we will then investigate what oxygen does to attribute to this increasing of graphene growth.

Except for the growth mechanism of graphene, 2D phosphorene recently has attracted great interest in the field due to its exciting electronic properties and potential

applications. In contrast to graphene, as the most popular semiconductor, it displays a direct band gap while still maintaining high carrier mobility.

However, its synthesis in large area and with high quality remains a significant challenge as a result of the chemical activity of phosphorus in the environment. Besides, is there any reason for the first successful CVD synthesis of monolayer phosphorene to be the growth of blue phosphorene but not black phosphorene since it is well-known as the most stable phase of phosphorene?

Thus, here we propose to explore the formation mechanism of phosphorene during the CVD growth by *ab initio* calculations. We will first propose a buckled honeycomb lattice strategy to search for all the possible isomers of phosphorene with high stability by carefully considering the bonding characteristics of phosphorus atoms. Secondly, we explore the potential of CVD synthesis of large area 2D phosphorene films by finding the proper metal substrates that are most probably to be efficient in phosphorene CVD growth and the most likely phases of phosphorene to be synthesized during the growth. With these theoretical works, the experimental synthesis of phosphorene could go on with a distinct direction.

Chapter 3. Methodology

This chapter describes the research methods for the study. In section 3.1, the most important method—DFT, is presented in detail. Since this is used in all of the three later chapters (chapter 4, 5, and 6) and is the central method for our research, the basic theorems, equations, and functionals are well explained. The second section briefly introduces the nudged elastic band (NEB) method used only in chapter 4. Since the method is already implanted into the DFT code VASP, only the essential concepts will be described as well as how it works.

3.1 Density Functional Theory (DFT)

Scientists have been trying to investigate the electronic structure of matter to further explore the properties (usually the ground states). So far they have proposed kinds of theories that could be employed to address the problem in specific areas, including some valence bond theories (generalized valence bond [198], modern valence bond [199, 200], *etc.*), molecular orbital theories (Hartree-Fock method [201], semi-empirical quantum chemistry methods [202], *etc.*), and electronic band structure (tight binding [204], DFT [204], *etc.*). Among various methods, DFT is one of the most popular and versatile theories to determine the properties of a many-electron system based on quantum mechanics. It has been widely used for the calculations in physics,

chemistry, and materials science.

DFT describes a system by using functionals, which are defined as functions of another function, in this case, the electron density. As the theory doesn't directly address the problem by solving the Schrödinger equation, [205] the method was suspected with low accuracy until the 1990s, when further approximations were employed to greatly improve the reliability by some new models of the exchange and correlation interactions. The relatively low computational cost, compared with some earlier methods, such as Hartree-Fock theory, as well as the relatively high accuracy, compared with methods like tight binding, allows the wide use of DFT method, ranging from atoms, molecules and crystals to nuclei and quantum and classical fluids.

3.1.1 Basic Quantum Mechanics

To fully describe a many-body system, the ultimate goal is to solve the time-independent, non-relativistic Schrödinger equation [205], written as below:

$$\hat{H}\Psi_i(\vec{x}_1, \vec{x}_2, \dots, \vec{x}_N, \vec{R}_1, \vec{R}_2, \dots, \vec{R}_M) = E_i\Psi_i(\vec{x}_1, \vec{x}_2, \dots, \vec{x}_N, \vec{R}_1, \vec{R}_2, \dots, \vec{R}_M). \quad (3.1)$$

In the equation, \hat{H} is the well-known Hamiltonian for a system consisted of M nuclei and N electrons. Usually the Hamiltonian can be written as

$$\hat{H} = -\frac{1}{2}\sum_{i=1}^N \nabla_i^2 - \frac{1}{2}\sum_{A=1}^M \frac{1}{M_A} \nabla_A^2 - \sum_{i=1}^N \sum_{A=1}^M \frac{Z_A}{r_{iA}} + \sum_{i=1}^N \sum_{j>i}^N \frac{1}{r_{ij}} + \sum_{A=1}^M \sum_{B>A}^M \frac{Z_A Z_B}{R_{AB}} . \quad (3.2)$$

Here, A and B stand for the M nuclei, while i and j indicate the N electrons in the system. In the right part of the formula, the first two terms denote the kinetic energies for the nuclei and electrons, respectively, while the latter terms describe the nucleus-electron, electron-electron, and nucleus-nucleus electrostatic interactions, respectively.

For a system in state Ψ , the expected energy of this system can be obtained by the below formula:

$$E[\Psi] = \frac{\langle \Psi | \hat{H} | \Psi \rangle}{\langle \Psi | \Psi \rangle}, \quad (3.3)$$

Where $\langle \Psi | \hat{H} | \Psi \rangle = \int \Psi^* \hat{H} \Psi d\vec{x}$. For a system of N electrons and M nuclei, and a given external potential, *the energy computed from a guessed Ψ is an upper bound to the true ground-state energy E_0 , stated as the variational principle.* This means with a “trial wave function” described with a set of parameters, we can find a best combination of these parameters for which the energy is the lowest.

Although, with equation 3.1 and 3.2, the state of the system can be described with the wave function of the system $\Psi_i(\vec{x}_1, \vec{x}_2, \dots, \vec{x}_N, \vec{R}_1, \vec{R}_2, \dots, \vec{R}_M)$ in principle, the $3M+3N$ degrees of freedom, as well as the multiple interactions between electrons and nuclei,

make it impossible to solve the equation analytically. Even with numerical calculations, the computational complexity is beyond our expectation. Therefore, scientists thought of some approximations to simplify the model. In 1927, Born and Oppenheimer proposed their model for Hamiltonian based on the fact that the nuclei move much slower than the electrons due to their great mass difference. [206] The system, then, can be considered with the fixed nuclei while the electrons moving fast around them. Thus, the kinetic energy of the nuclei is zero and their potential energy is a constant that can be viewed as zero too. The Hamiltonian, then, can be reduced to

$$\hat{H}_{elec} = -\frac{1}{2}\sum_{i=1}^N \nabla_i^2 - \sum_{i=1}^N \sum_{A=1}^M \frac{Z_A}{r_{iA}} + \sum_{i=1}^N \sum_{j>i}^N \frac{1}{r_{ij}} = \hat{T} + \hat{V}_{Ne} + \hat{V}_{ee}. \quad (3.4)$$

With the electronic Hamiltonian, the solution of the Schrödinger equation is the electronic wave function Ψ_{elec} and the corresponding energy is also electronic, E_{elec} . Thus the total energy should be the sum of the electronic one, and the constant nuclear repulsion term. Usually the latter term can be written as the nuclear potential \hat{V}_{ext} .

To further simplify the calculation, the wave function Ψ is also approximated as a product of spin orbitals $\psi_i(\vec{x})$, further consisting of a spatial orbital $\phi_k(\vec{r})$ and a spin function $\sigma(s)$. The Slater determinant is as below:

$$\Psi \approx \Psi_{HF} = \frac{1}{\sqrt{N!}} \begin{vmatrix} \psi_1(\vec{x}_1) & \psi_2(\vec{x}_1) & \dots & \psi_N(\vec{x}_1) \\ \psi_1(\vec{x}_2) & \psi_2(\vec{x}_2) & \dots & \psi_N(\vec{x}_2) \\ \vdots & \vdots & \vdots & \vdots \\ \psi_1(\vec{x}_N) & \psi_2(\vec{x}_N) & \dots & \psi_N(\vec{x}_N) \end{vmatrix}. \quad (3.5)$$

This is called the Hartree-Fock approximation method where the expectation value of the Hamiltonian operator with Ψ_{HF} is give as

$$E_{HF} = \langle \Psi_{HF} | \hat{H} | \Psi_{HF} \rangle = \sum_{i=1}^N H_i + \frac{1}{2} \sum_{i,j=1}^N (J_{ij} - K_{ij}), \quad (3.6)$$

where

$$H_i = \int \psi_i^*(\vec{x}) \left[-\frac{1}{2} \nabla^2 - V_{ext}(\vec{x}) \right] \psi_i(\vec{x}) d\vec{x}, \quad (3.7)$$

$$J_{ij} = \int \int \psi_i(\vec{x}_1) \psi_i^*(\vec{x}_1) \frac{1}{r_{12}} \psi_j^*(\vec{x}_2) \psi_j(\vec{x}_2) d\vec{x}_1 d\vec{x}_2, \quad (3.8)$$

$$K_{ij} = \int \int \psi_i^*(\vec{x}_1) \psi_j(\vec{x}_1) \frac{1}{r_{12}} \psi_i(\vec{x}_2) \psi_j^*(\vec{x}_2) d\vec{x}_1 d\vec{x}_2. \quad (3.9)$$

Equation 3.7 represents the kinetic energy and the electron-nucleus attraction. Equation 3.8 and 3.9 are the Coulomb integrals and exchange integrals.

3.1.2 Basic Density Functional Theories

Already understanding the elementary concepts of quantum mechanics, this section gives a brief introduction of the basic quantity and theorem of DFT.

In density functional theory, “density” represents the electron density of the system,

which is the central quantity of this method. The definition of this important term is described as the below formula:

$$\rho(\vec{r}) = N \int \dots \int |\Psi(\vec{x}_1, \vec{x}_2, \dots, \vec{x}_N)|^2 ds_1 d\vec{x}_2 \dots d\vec{x}_N. \quad (3.10)$$

The equation indicates that the electron density is the integral of the spin coordinates of all electrons but one of the spatial variables ($\vec{x} \equiv \vec{r}, s$). For a common interpretation, $\rho(\vec{r})$ stands for the probability of electrons being present within a small region of $d\vec{r}$. This determines $\rho(\vec{r})$ to be a non-negative function, vanishing at infinity and integrating to the total number of electron as shown below:

$$\rho(\vec{r} \rightarrow \infty) = 0, \quad \int \rho(\vec{r}) d\vec{r} = N. \quad (3.11)$$

The electron density also shares a very superior advantage as it is practically observable and is able to be measured with experimental approaches.

Having known the term--electron density, it is much easier to understand the first and most fundamental DFT developed by two predecessors, Thomas and Fermi in 1927. [207, 208] The theory is named after these two scientists as Thomas-Fermi (TF) model. The initial intention for this model is to describe the system in a much feasible way while the original wave function Ψ contains all the information of the studied system. Instead of the conventional approaches for the Schrödinger equation problem, this theory formulated the equation completely in terms of the electron density. For the

kinetic energy, the term can be derived as

$$T_{TF}[\rho(\vec{r})] = \frac{3}{10} (3\pi^2)^{2/3} \int \rho^{5/3}(\vec{r}) d\vec{r}. \quad (3.12)$$

Applying the classical expression for the nucleus-nucleus and electron-electron potentials, the energy of a single atom is then obtained:

$$E_{TF}[\rho(\vec{r})] = \frac{3}{10} (3\pi^2)^{2/3} \int \rho^{5/3}(\vec{r}) d\vec{r} - Z \int \frac{\rho(\vec{r})}{r} d\vec{r} + \frac{1}{2} \int \int \frac{\rho(\vec{r}_1)\rho(\vec{r}_2)}{r_{12}} d\vec{r}_1 d\vec{r}_2. \quad (3.13)$$

Although the change from wave function to the electron density is a great and important move for the development of DFT, the accuracy for this model is limited since the terms of the energy in the equation is only from approximations, especially the kinetic energy term. Lacking the consideration for the exchange energy and the electron correlation, further improvements are required.

3.1.3 Hohenberg-Kohn (HK) Theorem

Proposed by Hohenberg and Kohn in 1964, the existing of the two simple theorems make it possible for DFT to develop and be widely used by scientists. [209] The first HK theorem indicates that the Hamiltonian operator can be determined by the electron density and so are the properties of the system. It states that *for any system of interacting particles, the external potential $V_{ext}(\vec{r})$, and hence the total energy, is a unique*

functional of the electron density $\rho(\vec{r})$; since, in turn $V_{ext}(\vec{r})$ fixes \hat{H} , we see that the full many particle ground state is a unique functional of $\rho(\vec{r})$.

This theorem provides the prerequisite for the use of electron density in the Schrödinger as $\rho(\vec{r})$ determines $V_{ext}(\vec{r})$ and thus the properties of the system. Therefore, the kinetic energy, potential energy and total energy of the system can be derived as

$$E[\rho] = E_{Ne}[\rho] + T[\rho] + E_{ee}[\rho] = \int \rho(\vec{r})V_{Ne}(\vec{r})d\vec{r} + F_{HK}[\rho], \quad (3.14)$$

where

$$F_{HK}[\rho] = T[\rho] + E_{ee}. \quad (3.15)$$

As one can see, $F_{HK}[\rho]$ contains both the kinetic energy $T[\rho]$ and the electron-electron interaction, E_{ee} , whose explicit forms are unknown. Nevertheless, the latter term can be described as the sum of the classical part $J[\rho]$ and an complicated non-classical part of the electron-electron interaction, including the exchange and correlation of electrons:

$$E_{ee}[\rho] = \frac{1}{2} \int \int \frac{\rho(\vec{r}_1)\rho(\vec{r}_2)}{r_{12}} d\vec{r}_1 d\vec{r}_2 + E_{ncl} = J[\rho] + E_{ncl}[\rho]. \quad (3.16)$$

Thus we can see that the major challenge of the problem is the description of $T[\rho]$ and $E_{ncl}[\rho]$.

As for the second HK theorem, it demonstrates that the functional, $F_{HK}[\rho]$, gives the ground state energy, if and only if the ground state density is used. The second theorem states that the ground state energy can be achieved variationally: *the density that minimizes the total energy is the exact ground state density*, which can be expressed as the below formula:

$$E_0 \leq E[\tilde{\rho}] = T[\tilde{\rho}] + E_{Ne}[\tilde{\rho}] + E_{ee}[\tilde{\rho}]. \quad (3.17)$$

3.1.4 The Kohn-Sham (KS) Equations

To sum up the above discussion, the ground state energy of a system can be obtained by the equation below:

$$E_0 = \min_{\rho \rightarrow N} (F[\rho] + \int \rho(\vec{r}) V_{Ne} d\vec{r}), \quad (3.18)$$

where the functional $F[\rho]$ is presented as

$$F[\rho] = T[\rho] + J[\rho] + E_{ncl}[\rho]. \quad (3.19)$$

Now as $J[\rho]$ is already known, the main challenge is the solution for $T[\rho]$ and $E_{ncl}[\rho]$.

Very similar as the TF model of section 3.1.2, in 1965, Kohn and Sham proposed their

method to solve this problem where a non-interacting reference system is used to exactly calculate the kinetic energy as below. [210]

$$T_s = -\frac{1}{2} \sum_i^N \langle \psi_i | \nabla^2 | \psi_i \rangle \quad \rho_s(\vec{r}) = \sum_i^N \sum_s |\psi_i(\vec{r}, \vec{s})|^2 = \rho(\vec{r}) \quad (3.20)$$

Here ψ_i represent the orbitals of a non-interacting system and T_s is explained as the following equation:

$$F[\rho] = T_s[\rho] + J[\rho] + E_{XC}[\rho]. \quad (3.21)$$

The last term $E_{XC}[\rho]$ is defined as the exchange-correlation energy of the system as shown below

$$E_{XC}[\rho] \equiv (T[\rho] - T_s[\rho]) + (E_{ee}[\rho] - J[\rho]). \quad (3.22)$$

Thus all the unknown terms are concentrated to this term.

But how to uniquely determine the non-interacting orbitals with a Slater determinant which represents a real interacting system? To solve this problem, an additional term is introduced:

$$E[\rho] = T_s[\rho] + J[\rho] + E_{XC}[\rho] + E_{Ne}[\rho], \quad (3.23)$$

which can be further written as

$$\begin{aligned}
 E[\rho] = & T_s[\rho] + \frac{1}{2} \iint \frac{\rho(\vec{r}_1)\rho(\vec{r}_2)}{r_{12}} d\vec{r}_1 d\vec{r}_2 + E_{XC}[\rho] + \int V_{Ne}\rho(\vec{r}) d\vec{r} = \\
 & -\frac{1}{2} \sum_i^N \langle \psi_i | \nabla^2 | \psi_i \rangle + \frac{1}{2} \sum_i^N \sum_j^N \iint |\psi_i(\vec{r}_1)|^2 \frac{1}{r_{12}} |\psi_j(\vec{r}_1)|^2 d\vec{r}_1 d\vec{r}_2 + E_{XC}[\rho] - \\
 & \sum_i^N \int \sum_A^M \frac{Z_A}{r_{1A}} |\psi_i(\vec{r}_1)|^2 d\vec{r}_1. \quad (3.24)
 \end{aligned}$$

To apply the variational principles, the KS equations are written as

$$\left(-\frac{1}{2} \nabla^2 + \left[\int \frac{\rho(\vec{r}_2)}{r_{12}} + V_{XC}(\vec{r}_1) - \sum_Z^M \frac{Z_A}{r_{1A}} \right] \right) \psi_i = \left(-\frac{1}{2} \nabla^2 + V_s(\vec{r}_1) \right) \psi_i = \epsilon_i \psi_i, \quad (3.25)$$

where

$$V_s(\vec{r}_1) = \int \frac{\rho(\vec{r}_2)}{r_{12}} + V_{XC}(\vec{r}_1) - \sum_Z^M \frac{Z_A}{r_{1A}}. \quad (3.26)$$

As we can see that if the exact expression of E_{XC} and V_{XC} could be obtained, the KS equation would give us the exact energy as in equation 3.24.

3.1.5 The Exchange-Correlation Functionals

For all the exchange-correlation functionals, the local density approximation (LDA) is the most basic one. [211] The model assumes that there is a uniform electron gas, which the central idea can be written as the following equation

$$E_{XC}^{LDA}[\rho] = \int \rho(\vec{r}) \epsilon_{XC}(\rho(\vec{r})) d\vec{r}, \quad (3.27)$$

where $\epsilon_{XC}(\rho(\vec{r}))$ is the exchange-correlation energy per particle in this electron gas.

The accuracy of this LDA method is moderate and in certain cases, it can also fail which is thus insufficient for most DFT calculations. To further increase the accuracy, another approximation method was proposed in which not only the density, $\rho(\vec{r})$, but also the gradient of the density, $\nabla\rho(\vec{r})$, is used to describe a true electron environment. This method is called the generalized gradient approximation (GGA) as written below, [212]

$$E_{XC}^{GGA}[\rho_\alpha, \rho_\beta] = \int f(\rho_\alpha, \rho_\beta, \nabla\rho_\alpha, \nabla\rho_\beta) d\vec{r}. \quad (3.28)$$

Based on GGA, another method called the hybrid functional is derived, [213,214]

$$E_{XC}^{hyb} = \alpha E_X^{KS} + E(1 - \alpha)_{XC}^{GGA}, \quad (3.29)$$

where the first term in the right part of the formula is the exchange calculated with the KS wave function.

Although, in certain cases such as the calculation of Van der Waals energies, these functionals are still inadequate, GGA and the hybrid functional have already enhanced the reliability of the calculations and are widely used for computational physics and computational chemistry.

In this study, all the DFT calculations were performed via the Vienna ab initio Simulation Package (VASP) [215,216] with projected augmented wave (PAW) [217] method for the geometry optimization. Both standard DFT with GGA [212] and hybrid functional [213,214] methods were employed to investigate the energy of the system. To simulate Van der Waals interaction in the system, DFT-D3 method [218] was applied. A plane-wave cutoff energy of 400 eV was used and all the structures were fully relaxed with energy and force convergence criteria of 10^{-4} eV and 10^{-2} eV/Å, respectively. The Brillouin zone was sampled with different Monkhorst–Pack mesh k-points [219] with separation criteria of 0.03.

3.2 Nudged Elastic Band (NEB) Method

The NEB is a method to find the minimum energy path (MEP) between the known reactants and products. [220] Within the potential energy surface, the initial and final states, *i.e.* reactant and product, are both at the local minimum with multiple possible paths connecting in between. Among these paths, some may need to climb mountains (energy peaks), while some may pass through valleys. The most important one of these paths is the MEP along which any point is an energy minimum in all directions perpendicular to the path. [221] Thus, there must be an energy maximum along the path direction, which is called the saddle point in the potential energy surface. This saddle point is of great importance for characterizing the transition state and the energy

difference between this point and the initial state, called the activation energy, experimentally determines the rate of this reaction.

The NEB, called a chain-of-states method, [222] works by optimizing a string of images along the reaction path. These are the geometric configurations of the system along the path. During the optimization, spring forces are used at the same time to connect these configurations as to maintain equal spacing to neighboring configurations. After the optimization, the NEB is supposed to converge to the MEP, meaning the configurations of NEB would be able to describe the real reaction.

A NEB calculation starts with the insertion of images into the reaction path from the initial and final state. Usually, a linear initial path in terms of coordinates is enough, while, in some case, the linear path may lead to the problems. For example, along a linear path, the atoms may get too close to each other, resulting in huge repulsive force, which can destroy the configuration during the next optimization step. Or in other cases, typical paths have appeared before. Under these circumstances, manual adjustments will greatly increase the accuracy or reduce the time cost.

In the NEB method, the images will be optimized to the MEP with the help of a force combined with a spring force along the path direction to ensure equal spacing, and a potential force perpendicular to the path to reach an energy minimum along all the other directions. Once the convergence criteria are met, the optimizations stop and the NEB is done. The configurations of the MEP and their energies will be obtained. A line could

be drawn along the energies and at the peak is the saddle point as shown in Figure 3.1. However, as we can see in the figure, the regular NEB is usually not able to have an exact configuration of the transition state at the saddle as the saddle itself comes from the fitting of the energies. Due to the fitting, the activation energy should be only an estimation suffering from low accuracy.

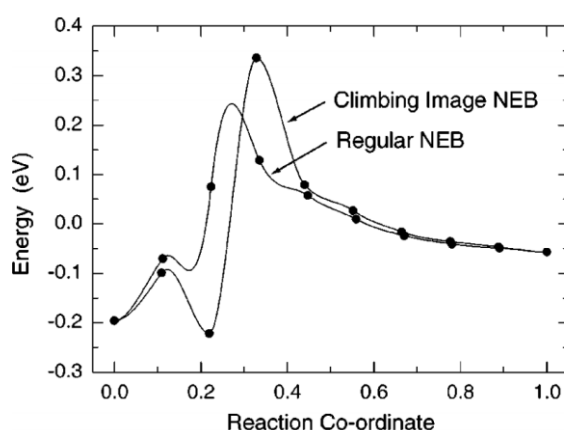


Figure 3.1 NEB and CINEB calculations of the MEP for CH₄ decomposition on Ir(111) surface.

Reprinted from [223], with the permission of AIP Publishing.

With the above considerations, a small modification has been made to improve the NEB method in which the highest energy image is forced to climb to the saddle point. [223] This climbing image NEB (CI-NEB) method starts to work after a few steps of regular NEB, while, at the time, the image of the highest energy already distinguishes itself. This image will then not be affected by the spring forces and climbs up the potential energy surface along the path but goes down along the other directions that perpendicular to the path. The other images follow the same protocol as in the NEB. Therefore, after converging to MEP, there will be an image right at the saddle point,

which exactly tells the activation energy and configuration of the transition state in some way. As shown in Figure 3.1, there is a much higher estimation of the activation energy of CI-NEB compared with that of the regular NEB, while the computational costs of both methods are almost the same. It is noted that without the spring forces' restriction, the spacing on each side of the climbing image will be different from the others, one side to be compressed and the other to be stretched.

The NEB method used in this studied is the CI-NEB version that has been incorporated into the DFT code VASP. Except for the initial and final configurations, four additional images were inserted into to the path. The spring constant of the forces between the images was set to $-5.0 \text{ eV/\text{Å}^2}$. The optimizer employed in CI-NEB here was from the VASP optimizer specified by IBRION, indicating it is a damped molecular dynamics method. The other parameters were just set as the same as those of the above DFT's.

Chapter 4. Graphene CVD Growth with Continuous Supply of Oxygen

4.1 Introduction

As stated in the literature review, a large number of previous work have been done for the synthesis of graphene of large-area, high-quality, and single-crystal on copper foils. [123,126,172] Their successes in the uniform graphene growth usually lie on the suppression of the nucleation sites. However, these ways of nucleation reduction are usually achieved by decreasing the feedstock concentration, which, in return, brings about the steep drop of growth rate.

On the contrary, the CVD growth of high-quality carbon nanotubes with a growth rate up to 80 $\mu\text{m/s}$ has already been achieved. [224] Since graphene as the 2D form of such graphite materials shares various similarities with this 1D counterpart, one would, without hesitation, expect a growth rate of the same level via CVD method. After we reviewed all the previous work about graphene CVD growth, the highest growth rate we found, however, is only 4.2 $\mu\text{m/s}$ with the help of a Cu-Ni alloy. [172] This means a wide gap in which scientists can do much further research work for increasing the growth rate of graphene by CVD method.

Furthermore, the role of oxygen in graphene CVD growth has been investigated by many researchers. [121,123,173] The oxygen was believed to suppress the nucleation,

as well as to accelerate the growth. However, the mechanism of the acceleration is unknown, and the increase of the growth rate is limited, probably due to the insufficient supply of oxygen. Thus, experimentally how to continuously deposit oxygen onto the catalyst surface, and theoretically how oxygen is able to promote graphene growth, are problems need to be solved.

4.2 Experimental and Elementary Theoretical Results by Collaborators

To ensure the supply of a continuous oxygen flow, our collaborators, Xu *et al.* came up with an idea to add an adjacent oxide substrate below the copper foil as shown in Figure 4.1a and b. The CH₄ feeding vapor was able to flow through the gap between the oxide substrate and the copper foil with a width of about 15 μm. [122] It was proved by previous work that at a temperature of higher than 800 °C, the oxide substrate was able to generate oxygen slowly, which serves as the continuous supply of oxygen here. [225] With the help of Auger electron spectroscopy (AES) as shown in Figure 4.1c, an oxygen release from the oxide substrate was proved both after the annealing in CVD and in ultrahigh vacuum. Further demonstration of the high concentration of oxygen in the narrow gap was presented by their diffusive model of air flow as shown in the supplementary of their work. [122] Thus a greatly increased oxygen attachment to the copper surface was guaranteed.

With this modification of the CVD method, large-area circle-shaped graphene films with a size of ~ 0.3 mm were synthesized on the copper foils both with the SiO_2 and Al_2O_3 substrates (Figure 4.1d and f) within only one minute. To be noticed, the large and circular films were only observed on the back side of the copper foils as marked in Figure 4.1b, while on the front side of these copper foils, graphene films were of much smaller size (~ 20 μm) and with star-like shape (Figure 4.1e). By substituting the oxide substrate by graphite as a control check, on both the front and back sides of the copper foils grew similar small star-shaped graphene films. As graphite brought an oxygen-free environment to the system, it is reasonable to say that oxygen here plays an important role in fabricating the large-area graphene with a high growth rate.

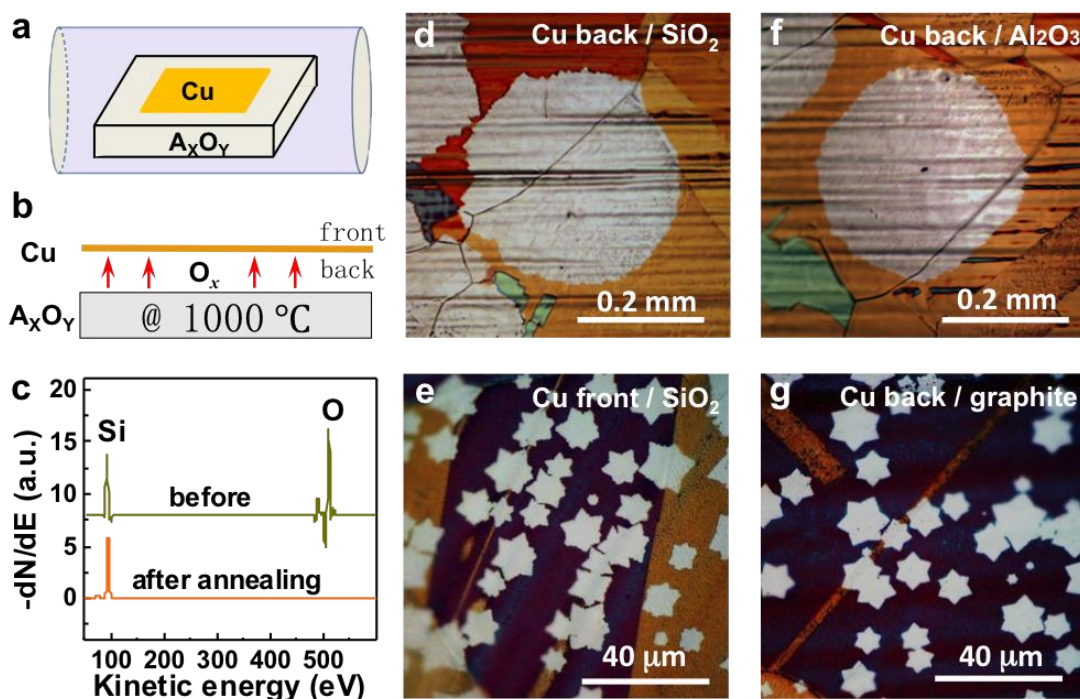


Figure 4.1 (a) Schematic of graphene ultrafast CVD growth on an oxidized substrate and (b) its side view. (c) Auger electron spectroscopy (AES) of SiO_2/Si substrate at $\sim 1,000^\circ\text{C}$ illustrating the

releasing of oxygen. Optical micrographs of graphene **(d)** large round domains on the back of the copper foil and **(e)** the small star-like domains on the front with SiO₂/Si substrate. Optical micrographs of graphene **(f)** large domains on the back of copper foils with Al₂O₃ and **(g)** small star-like domains with graphite substrate. Reprinted by permission from Macmillan Publishers Ltd: Nature Nanotechnology [122], copyright(2016).

To further confirm the high quality of the grown graphene, high-resolution measurements were conducted as shown in Figure 4.2 including SEM, SAED, LEED, and STM measurements. The SEM image of the graphene domains in Figure 4.2a firstly verify the large area of the graphene. Figure 4.2b-d are the SAED patterns from the marked areas in Figure 4.2a. Figure 4.2e-h present the LEED patterns of a typical graphene domain. The highly identical crystallographic orientations of SAED and LEED patterns of the fabricated graphene demonstrate that the graphene domains have high-quality single-crystalline structures. The four STM images as shown in Figure 4.2i-l, further reveal the high quality of the graphene crystals with perfect hexagonal lattices and no defects. The hall mobility of the synthesized graphene was also measured after the transferring to SiO₂/Si substrates. The 4,500-6,500 cm²V⁻¹s⁻¹ value at 1.4 K is comparable with most reported values for the CVD growth of graphene.

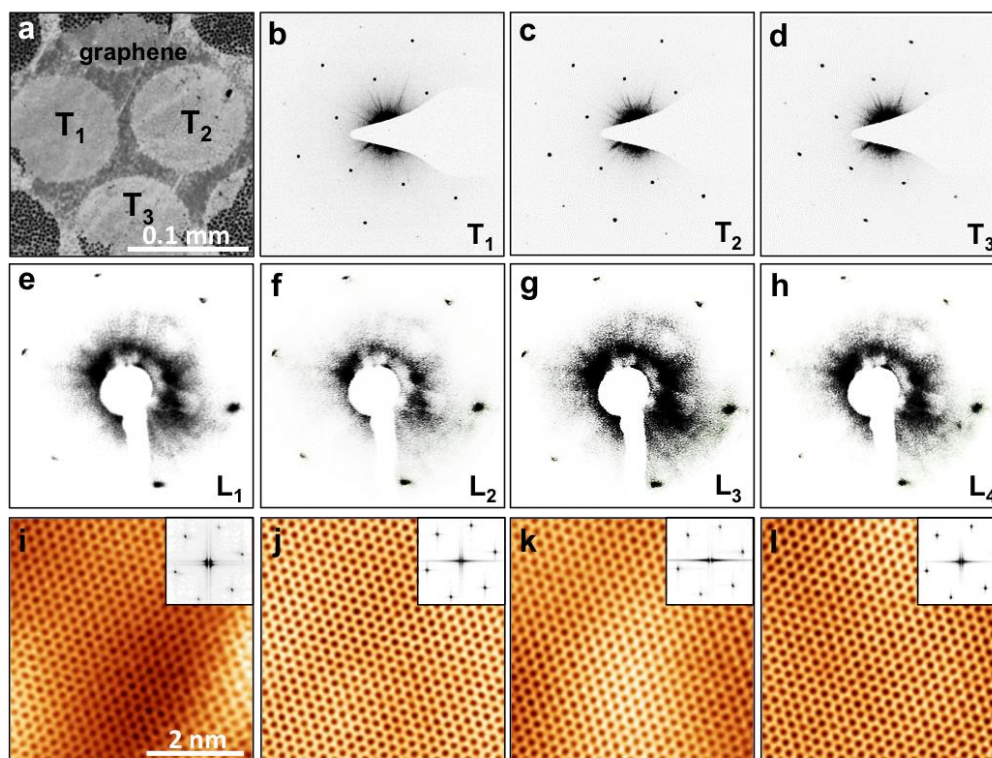


Figure 4.2 (a) SEM image of graphene domains. (b-d) SAED patterns of T₁, T₂ and T₃. (e-h) LEED patterns of graphene domains of 4 different areas. (i-l) STM images of different areas in one graphene domain. Reprinted by permission from Macmillan Publishers Ltd: Nature Nanotechnology [122], copyright(2016).

Further, optical microscope captured the images of the graphene growth with continuous supply of oxygen at time 0 s, 2 s, and 5 s as shown in Figure 4.3a, b, and c, respectively. The time $t=0$ s is defined as when the graphene domain was able to be spotted, of which the size is $\sim 2 \mu\text{m}$. The Figure 4.3c clearly shows that, with only 5 seconds, the graphene domain was able to reach a size of 0.3 mm, since the reaction had been stopped at each time t by terminating the heating and inputting a large Ar flow

instead of CH_4 feeding. This means a surprisingly high growth rate of $\sim 60 \mu\text{m/s}$, which is several orders of magnitude higher than previous reported values. More importantly, as shown in Figure 4.3d, the linear increase of the domain size, with growth time, indicates that, during the whole growth process, the high rate was able to maintain constant. The observed high and constant growth rate is quite different from the previous studies.

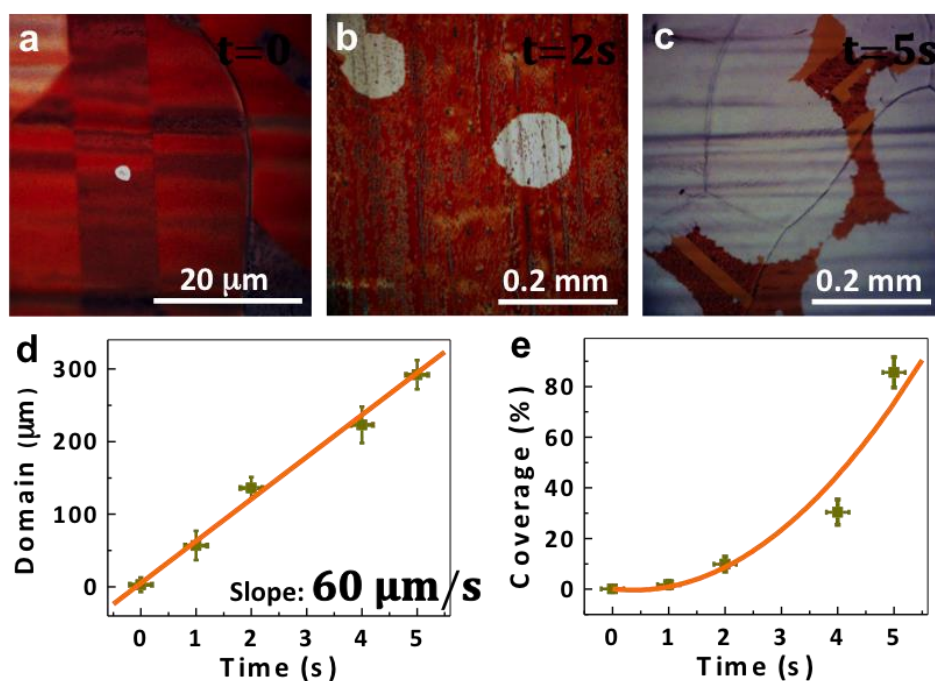


Figure 4.3 (a-c) Optical images of graphene size at different times. (a) $t = 0$ s stands for the moment when the graphene domain was visible at first time. (b) 2 s and (c) 5 s mean the graphene domain had grown for 2 and 5 seconds from the moment graphene domain was large enough to be seen. (d) Graphene domain size vs growth time. The slope indicates a $60 \mu\text{m/s}$ growth rate. (e) Graphene coverage vs growth time. Reprinted by permission from Macmillan Publishers Ltd: Nature Nanotechnology [122], copyright(2016).

It is noticed that i) the average growth rate is surprisingly high (several orders of magnitude higher than previous values); ii) the rate remains constant during the growth; iii) the grown graphene domains tend to be in rounded shapes. But usually the self-limited growth of graphene on copper substrates, resulting from the low carbon flux, will lead to a star-like domain shapes like those on the front of the copper foils. And with this self-limited mechanism, the growth of graphene is always nonlinear, *i.e.* the rate will decrease fast as the graphene coverage increases. These contradictories could indicate a different mechanism for the graphene growth with the assistance of oxygen. And the carbon flux is expected to play a critical role in this change. To investigate the mechanism for the ultrafast growth of graphene, phase field theory (PFT) was firstly used to simulate influence of the different carbon flux (F) in the experiment, ranging from 0.001 to 4, on the growth and evolution of graphene domains.

As we can see from Figure 4.4a-c, with small F (0.001), graphene domain tends to be fractal. With the increase of F , the fractal shape vanishes, and at $F=0.1$, it turns to become more in a star-like shape. Finally at $F=4$, the domain becomes round-shaped. The corresponding concentration of the carbon precursor on the catalyst surface, as shown in Figure 4.4d-f, could probably explain the reason. Since at low F , the concentration around the graphene domain increases gradually, while at high F , the carbon concentration immediately reaches the highest at the edge of graphene domain. Defined as the distance of a strip between 90% maximum concentration and 110% minimum concentration, the width of depletion zone (Figure 4.4g) is significantly large

at the edge of the graphene domain with a low carbon flux. Thus the carbon concentration should be much lower at the growth edge than that in the area far from the graphene domain. While with high carbon flux, the depletion zone becomes almost negligible and therefore every growth site at the domain edge is offered with supersaturated carbon species that can afford graphene's ultrafast growth.

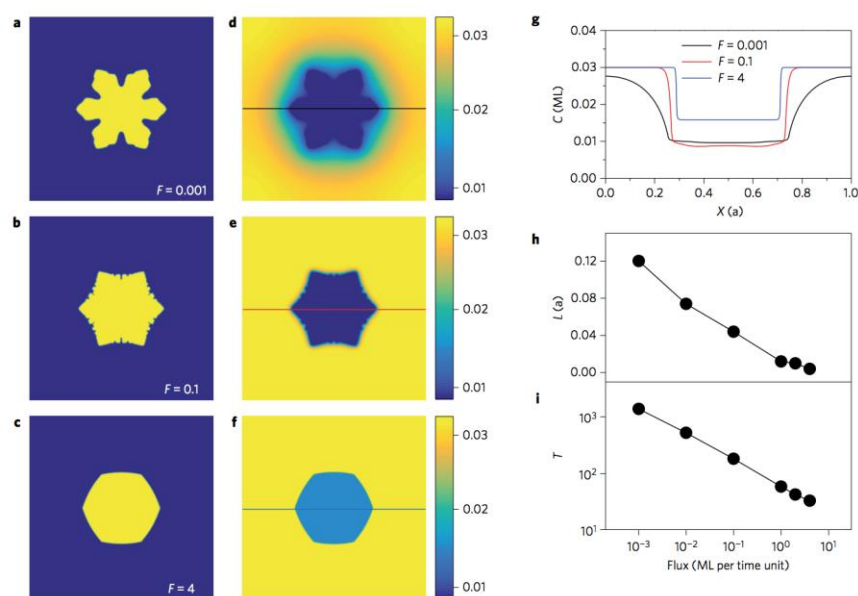


Figure 4.4 PFT simulation of the graphene domain evolution with carbon flux (F) change. **(a–c)**, Graphene domain change, and **(d–f)** concentration profile change with carbon flux from 0.001 **(a,d)** to 0.1 **(b,e)** and then to 4 **(c,f)** by the PFT calculations. **(g)** Concentration profiles of the carbon species as precursor along the lines marked in **(d, e, f)**. **(h)** Width of the depletion zone and **(i)** time for growing a domain with the size of 1/4 coverage as a function of the carbon flux. Reprinted by permission from Macmillan Publishers Ltd: Nature Nanotechnology [122], copyright(2016).

Figure 4.4h makes it clear that with the increase of carbon flux, the width of depletion zone decreases. At a carbon flux of 4, the depletion zone nearly disappears and the

graphene growth switches from a diffusion-limited (self-limited) model to an attachment-limited model. This growth mechanism change could also be well proved by the above discussion about the change of the shape evolution of graphene from fractal to round hexagonal domains. [7] In Figure 4.4i, the growth time required for 1/4 graphene domain coverage drops almost linearly as the carbon flux goes up. It reasonably confirms that when the carbon flux is large enough, the growth rate of graphene domains could be very high just as what we achieved in our new graphene CVD method.

This PFT simulation shows that the greatly enhanced carbon flux leads to a mechanism change from the diffusion-limited growth to attachment-limited growth, and thus results in the significant increase of growth rate and the round domain shape of graphene. But how to relate the increase of carbon flux with the continuous supply of oxygen? The below section tells the reason.

4.3 Oxygen Assistance on CH₄ Dissociation

In last section, it has been demonstrated that the ultrafast growth of graphene and the round-shaped domain result from the high carbon flux. Here, how the continuous supply of oxygen from the oxide substrate could greatly promote the dissociation of CH₄ molecules, and then increase the carbon flux on the copper surface is revealed by

CI-NEB method with DFT calculations.

In this section, the metal surfaces were simulated by 4-atomic layer thick slab models of Cu(100) surface with periodic boundary condition (PBC). The PBC supercells consisted of 4×4 copper atoms on the x - y plane. A ~ 15 Å thick vacuum layer is used to separate the slabs to avoid periodic image interaction. When the structures were optimized, the bottom layer of the slabs was fixed, while copper atoms of all the other layers were fully relaxed. According to the size of the models, the Brillouin zone was sampled with $3 \times 3 \times 1$ Monkhorst–Pack mesh k-point.

To investigate the role of oxygen on graphene ultrafast growth, a calculation of the first step of the dehydrogenation process of CH_4 on Cu(100) surface with and without the assistance of oxygen was performed. To point out, the reason for choosing Cu(100) as the copper surface for our calculation is that our previous study (to be submitted) shows that Cu(100) is more favorable than Cu(111) and Cu(110) as for the full decomposition of CH_4 . The result is shown in Figure 4.5. The CH_4 decompositions with and without the existence of oxygen atom are through the reaction paths of



which we denote as reaction (1) and (2), respectively. Taking the reactant's energy as

0, the potential energies of the transition state and the product of reaction (1) are 0.62 and 0.24 eV, respectively, whereas those of reaction (2) are 1.57 and 0.84 eV. This means that the energy barriers of CH₄ decompositions with and without oxygen atom are, 0.62 and 1.57 eV, respectively, and the reaction energies of these two paths are 0.24 and 0.84 eV, respectively. It is obvious that the existence of the significant reduction of both energy barrier (0.95 eV) and reaction energy (0.60 eV) with the supply of oxygen will greatly raise the reaction rate of the first step of CH₄ decomposition, and also the concentration of CH₃ radicals. By the further dissociation of CH₃ radicals, it could be expected that the concentrations of CH₂, CH, and C will increase too.

To obtain a deeper understanding on how oxygen is capable of reducing the barrier of CH₄ decomposition on the copper surface, the optimized structures of reactants, transition states, and products of reaction (1) and (2) are presented in Figure 4.5b. It is clearly seen that, during the CH₄ decomposition through reaction (2), a transition state appears, where the hydrogen atom is isolated and its bonding with C is breaking up while the bonding with Cu has not been built up. This is surely a state with extremely high potential energy. With the existence of oxygen atom on copper surface as in reaction (1), this condition with high potential energy is eased, because the oxygen atom here stabilizes the isolated hydrogen by the formation of O-H bonding, and thus greatly lowers the potential energy of the transition state. Very similar process takes place in products, where the otherwise isolated hydrogen atom on the copper would be

substantially stabilized by the existing O atom. Oxygen atoms, here, act as a bridge between H and the Cu surface. The formation of Cu-O-H bond is much more favorable than that of weak interaction between hydrogen and copper atoms as Cu-H bond. These changes, thus, significantly reduce the energy barrier and the reaction energy of CH₄ decomposition.

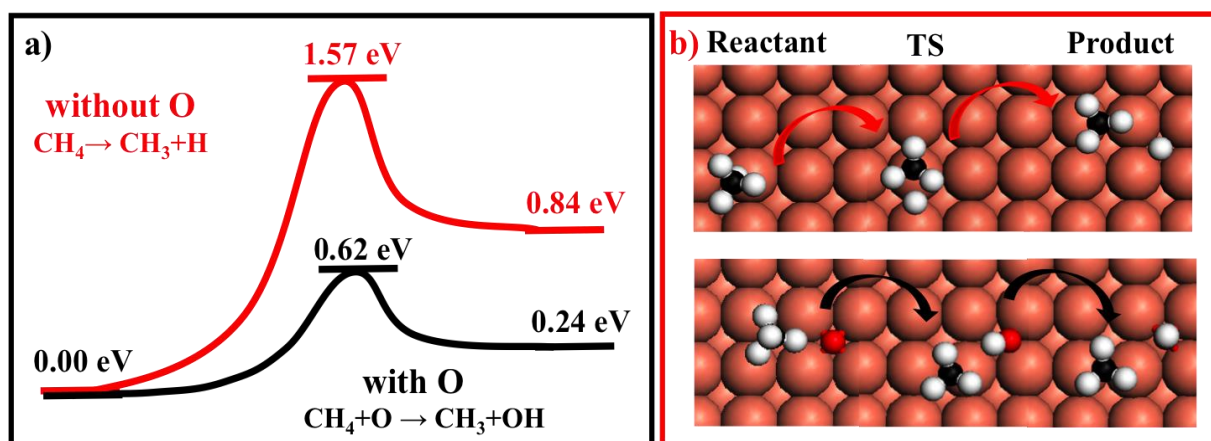


Figure 4.5 CI-NEB calculation of CH₄ dissociation reaction with and without the assistance of oxygen on Cu(100) surface. (a) The energy barriers of the CH₄ decomposition reactions of CH₄+O → CH₃+OH (1) and CH₄ → CH₃+H (2) on the Cu(100) surface with (black line) and without (red line) oxygen, are 0.62 and 1.57 eV, respectively. (b) The MEP of decomposition reaction (1) (lower figure with black arrowheads), and reaction (2) (upper figure with red arrowheads) on copper surface with and without oxygen atoms, respectively. The white, red, black, and orange spheres represent H, O, C, and Cu atoms, respectively. All the atomic structures of reactants, transition states (TS), and products are optimized.

To roughly estimate the increase of carbon flux as a result of barrier reduction, the coverage of oxygen atoms on Cu(100) surface is assumed to be in a range of $c_o=0.01$

to 0.1. According to the theories of reaction kinetics, the rate of CH₄ decomposition through reaction (1) on Cu(100) surface is expected to increase by

$$c_o \cdot \exp(\Delta E_b/k_B T) = c_o \cdot \exp(0.95 \text{ eV}/k_B T) \sim 57 - 570 \quad (4.3)$$

Here, T is the normal temperature for graphene growth on copper surfaces and k_B is the Boltzmann constant. This estimation, together with our result of CI-NEB calculation, indicates that, with the continuous supply of oxygen, the carbon species flux can be increased by several orders of magnitude. The enhanced carbon flux, as discussed in last section, will change the growth model and then increase the growth rate of graphene domains. Together with the other well-established theories of the role of oxygen in lowering the nucleation sites [121,123,197], our mechanism of oxygen assisted barrier reduction has well explained the growth rate increase for graphene CVD synthesis.

Considering the multiple possibilities of the carbon species (CH₃, CH₂, CH, and C) that could actually be utilized in graphene growth, a further investigation on the full dehydrogenization of CH₄ has been made. Except for reaction (1) and (2) as the first step of the decomposition, the second step of CH₄ dissociation with and without oxygen atom are written as





which are denoted as reaction (3) and (4). The third step reactions with and without oxygen denoted as reaction (5) and (6) are



while the fourth step with and without oxygen denoted as reaction (7) and (8) are



Each decomposition, with or without oxygen atom, consists of four steps in which the four hydrogen atoms all break their bonds with the carbon atom. The result of CI-NEB calculations of the left three steps of the composition reactions is presented in Figure 4.6. Together with Figure 4.5, it is clearly seen that, for each step, the reaction with oxygen atom has a lower barrier and a lower reaction energy: 0.95 and 0.60 eV for energy barrier and reaction energy reductions in first step dehydrogenization, 0.08 and 0.22 eV for those in second step, 0.16 and 0.41 eV for those in third step, and 0.36 and 0.81 eV for those in final step.

As we can see in Figure 4.6b, d, f, and Figure 4.5b, in the decomposition reactions without oxygen, the adsorbed CH₄ molecule breaks one C-H bond each step and then the detached hydrogen is adsorbed by the copper surface again. For the final step, after the departure of the last hydrogen, the carbon atom is adsorbed alone on the hollow site of the Cu(100) surface. Since the potential and the position of each carbon species on copper surface are different, the immediate state of the further dehydrogenized carbon radical and the detached hydrogen atom is of great difference. Thus the potential energies of the transition states and the products vary significantly. As a result, the energy barriers and reaction energies of CH₄ decomposition range from 0.69 to 1.57 eV and -0.02 to 0.84 eV, respectively.

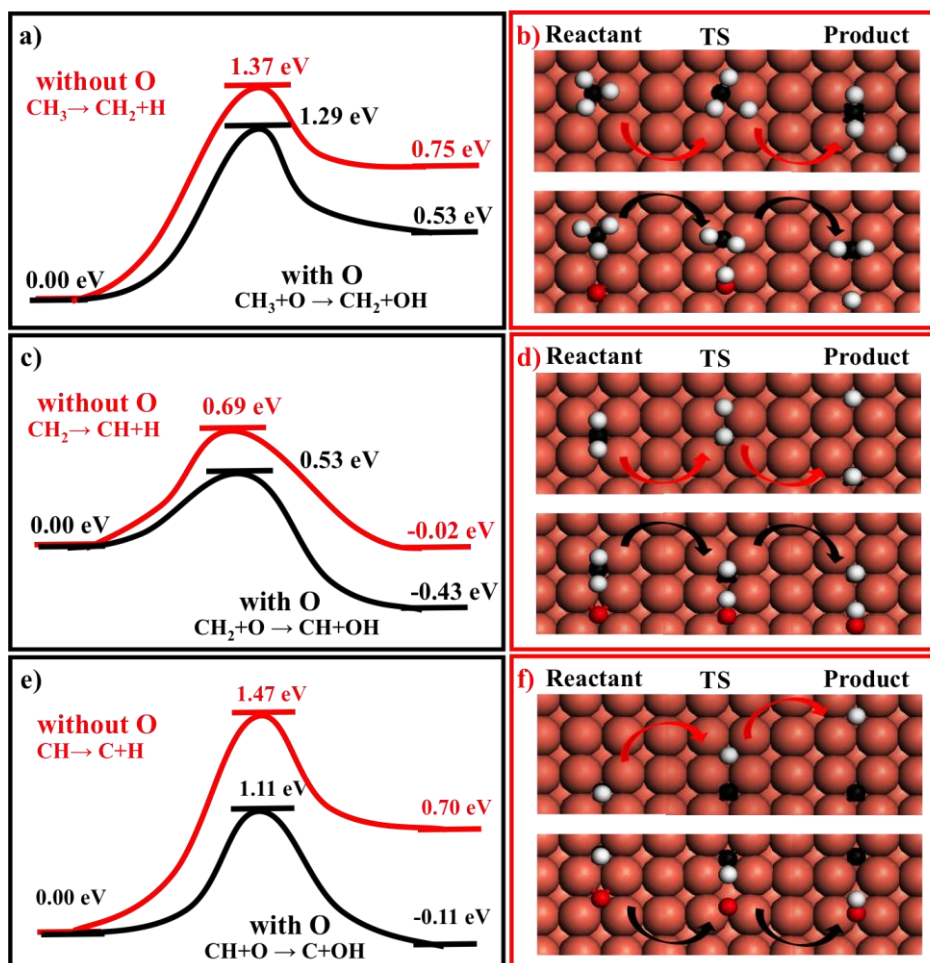


Figure 4.6 CI-NEB calculation of $\text{CH}_3/\text{CH}_2/\text{CH}$ dissociation reaction with and without the assistance of oxygen on Cu(100) surface. (a), (c), (e) The energy barriers of decomposition reactions of (a) $\text{CH}_3 + \text{O} \rightarrow \text{CH}_2 + \text{OH}$ (3) and $\text{CH}_3 \rightarrow \text{CH}_2 + \text{H}$ (4) with (black line) and without (red line) oxygen, (c) $\text{CH}_2 + \text{O} \rightarrow \text{CH} + \text{OH}$ (5) and $\text{CH}_2 \rightarrow \text{CH} + \text{H}$ (6) with (black line) and without (red line) oxygen, (e) $\text{CH} + \text{O} \rightarrow \text{C} + \text{OH}$ (7) and $\text{CH} \rightarrow \text{C} + \text{H}$ (8) with (black line) and without (red line) oxygen, on the Cu(100) surface, respectively. (b), (d), (f) The MEP of decomposition reaction (3), (5), (7) (lower figure of (b), (d), (f) with black arrowheads), and reaction (4), (6), (8) (upper figure of (b), (d), (f) with red arrowheads) on copper surface with and without oxygen atoms, respectively. The white, red, black, and orange spheres represent H, O, C, and Cu atoms, respectively. All the

atomic structures of reactants, transition states (TS), and products are optimized.

In reactions with oxygen atom, each time when the C-H bond is breaking up, the bond between hydrogen and oxygen is building up, and every detached hydrogen atom will be adsorbed by the copper surface in the form of OH radical, which is much more stable. Therefore, the potential energy for each step lowers with oxygen as well as the reaction energy. For the decomposition without oxygen, the reactions are almost all endothermic (except for step 3, *i.e.* reaction (6), with only a very little decrease in potential energy during the dehydrogenization), while oxygen, step 3 and 4 (reaction (5) and (7)) both become exothermic, which also means that the reactions happen much easier.

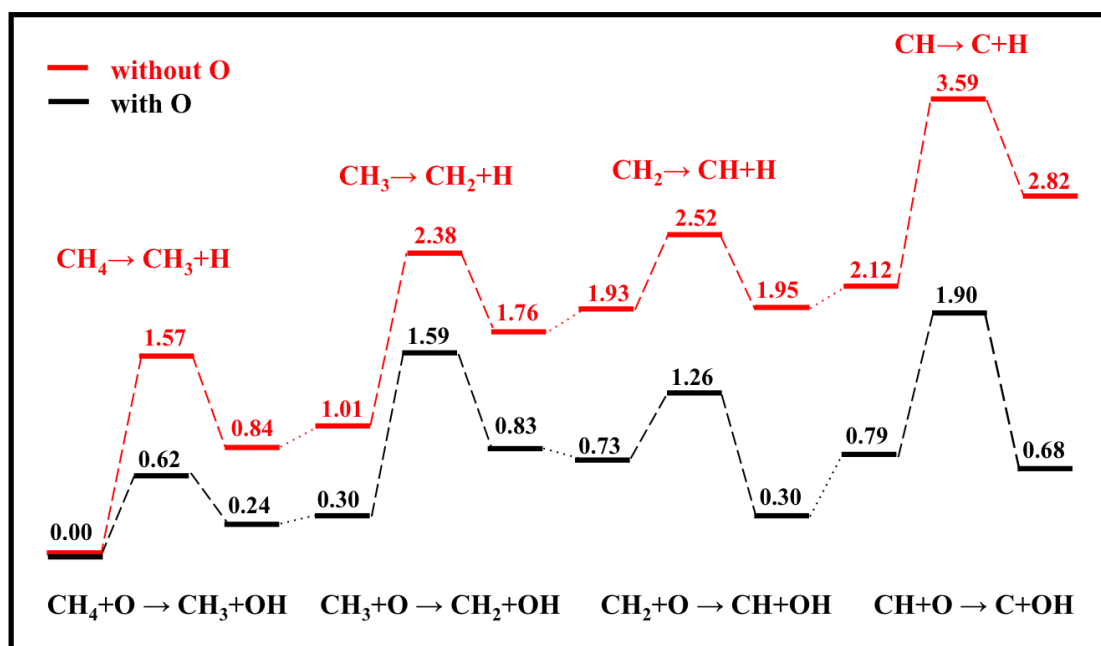


Figure 4.7 Summary of CI-NEB calculations of CH_4 full dissociation reactions with and without the assistance of oxygen on Cu(100) surface. The energy barriers of the CH_4 decomposition reactions of $\text{CH}_4 + \text{O} \rightarrow \text{CH}_3 + \text{OH}$ (1), $\text{CH}_3 + \text{O} \rightarrow \text{CH}_2 + \text{OH}$ (3), $\text{CH}_2 + \text{O} \rightarrow \text{CH} + \text{OH}$

(5), and $\text{CH}+\text{O} \rightarrow \text{C}+\text{OH}$ (7) on the Cu(100) surface with (black line) oxygen, are 0.62, 1.29, 0.53 and 1.11 eV, respectively; the energy barriers of the CH_4 decomposition reactions of $\text{CH}_4 \rightarrow \text{CH}_3+\text{H}$ (2), $\text{CH}_3 \rightarrow \text{CH}_2+\text{H}$ (4), $\text{CH}_2 \rightarrow \text{CH}+\text{H}$ (6), and $\text{CH} \rightarrow \text{C}+\text{H}$ (8) on the Cu(100) surface without (red line) oxygen, are 1.57, 1.37, 0.59, and 1.47 eV, respectively.

To present a whole picture of oxygen's effect on CH_4 dissociation, Figure 4.7 shows the potential energy changes during the CH_4 full decomposition process with and without oxygen atom on Cu(100) surface. After climbing an energy barrier of 0.62 eV, CH_4 is transformed first into CH_3+OH with the existence of oxygen, whose reaction energy is predicted to be 0.24 eV. Since the OH radical is considered to liberate from copper surface, there is surely a potential energy difference between this product and the next time reactant as in the initial state, a new oxygen atom is required to help decomposition. Thus, second step decomposition reaction $\text{CH}_3+\text{O} \rightarrow \text{CH}_2+\text{OH}$ proceeds by overcoming a barrier of 1.29 eV, with a reaction energy of 0.53 eV. Similarly, the CH_2 species can further dissociate to CH and OH, whose formation demands a barrier of 0.53 eV, with a reaction energy of -0.43 eV. The calculation suggests that the final product of C and OH lies 0.68 eV in the potential surface, and a barrier of 1.11 eV is required for this step.

Comparing CH_4 full decomposition with and without oxygen's assistance, it clearly shows that for each dehydrogenization step, the barrier is lower with oxygen. This indicates that, with the continuous supply of oxygen, the reaction rate is higher for each

decomposition step. Thus, no matter which kind of carbon species is the key participant of graphene growth, the flux will be raised and the growth rate increased. The highest energy barrier of the four steps with oxygen (step 2, 1.29 eV), also, is lower than that without oxygen (step 1, 1.57 eV). However, it might not be reasonable to just compare the highest barrier, though it indicates the rate-determining step. Because, as we mentioned before, the dissociation reaction is complicated, and more importantly, it is not sure that which kind of carbon species is dominant as the precursor of graphene growth. Also to be noticed, if there exists oxygen, the reaction energy is also lower for each step of the decomposition reaction; more steps are exothermic; the potential energy of the final product (the adsorbed carbon atom) is 2.14 eV lower than that without oxygen. These all demonstrates that the CH_4 decomposition are thermodynamically more favorable with the existence of oxygen.

4.4 Summary

In this chapter, by CI-NEB method, the mechanism of the ultrafast growth of high-quality single-crystal graphene on copper foils with the continuous supply of oxygen is studied. With the innovative CVD approach of our collaborators, the growth of 0.3-mm-sized graphene domains in just with a significant growth rate of 60 μm was achieved. To illustrate the mechanism of the high growth rate and the round shape of graphene domain, the PFT method was firstly used to show that it is due to the high

carbon flux in the system that the growth rate of graphene could be higher than previously reported ones and the graphene domain shape could be specifically round. Thus, to connect the assistance of oxygen with the high carbon flux, the CI-NEB method was employed to examine the energy barrier difference between the CH₄ decomposition with and without the continuous supply of oxygen. The result shows that with the existence of oxygen atom, the energy barrier of the dehydrogenization of CH₄ is 0.95 eV lower than that without oxygen atom for the first step, as well as the reaction energy reduction (0.60 eV). According to reaction dynamics, this kind of barrier reduction would lead to a great increase of reaction rate by a few orders of magnitude, and also the increase in the concentration of other carbon species. This result could perfectly explain the ultrafast growth of graphene. Since the participation of oxygen in CH₄ decomposition greatly reduce the reaction barrier and reaction energy, it results in the increase of carbon flux and finally changes the growth mechanism to raise the growth rate of graphene.

Chapter 5. Isomers of Phosphorene

5.1 Introduction

After the successful isolation of BP, many scientists have become interested in the exploration of the stability and electronic properties of other phosphorene phases since the sp^3 -bonded way of phosphorus makes it possible to form a vast variety of isomers. David Tomanek's group first predicted the famous blue phosphorene (BLP) with a much larger band gap (2.66 eV) than BP (1.36 eV), but is almost equally stable with only an energy difference of 0.03 eV/atom. [188] Later, they predicted another two kinds of phosphorene, named γ - and δ -phosphorene, along with BP and BLP named α - and β - phosphorene. [189] Other researchers like J. X. Zhong and H. Zeng have also done similar work [191,192]. Most of the above phosphorene isomers are predicted to be energetically stable but present quite different electronic properties, which indicates that these fantastic properties of phosphorene isomers may be tuned by the structural arrangement of phosphorus atoms. Thus it is intriguing to find out if there are more 2D monolayer phosphorene isomers with modified band gaps and electronic properties.

Here, in lack of a comprehensive and systematic searching for all the possible phosphorene isomers, we propose a strategy to explore the allotropes of phosphorene within small unit cell ($N_p \leq 8$). Excluding the less stable structures, 8 isomers are obtained including 5 reported structures named as α - (BP), β - (BLP), γ -, and δ -phosphorene and the recently found red phosphorene by carefully optimization. While

BP is the most energetically stable isomer reported and predicted, we find that all the good structures we get resembles the specific features of BP such as the similar bond length and bond angle. Furthermore, our study shows that although the found isomers all share similar stabilities, they differ in electronic properties since their energy band gaps range from 0.30 to 2.66 eV.

5.2 A Global Searching Method for Phosphorene Isomers

In all reported phosphorenes, phosphorus atom is sp^3 -bonded, (Figure 5.1a) meaning only three of the hybridized orbitals form coordinated bonds, while another orbital is occupied by a lone electron pair, which results in the puckered structure of phosphorene. For sp^3 -bonded phosphorus, the bond angles usually can range from 90° to 109.5° of an ideal maximum of tetrahedral without lone electron pair, while for a P-P bond, the bond length ranges from 2.18 to 2.35 Å [226].

To further narrow down the number of isomers, we need to apply Euler's theorem [227]:

$$F_c - E + V = \chi, \quad (5.1)$$

where F_c , E , and V represent the number of faces, edges and vertices, respectively.

χ , here, is called the Euler characteristic, while in 2D, it should be just 2. Thus,

$$F_c - E + V = 2. \quad (5.2)$$

For a system of N -side polygons and z coordinates ($z=3$), we have

$$F_c = \frac{V \cdot z}{N}, \quad (5.3)$$

$$\text{and } E = \frac{V \cdot z}{2}. \quad (5.4)$$

With formula (5.2), (5.3) and (5.4),

$$\frac{z}{N} = \left(1 - \frac{1}{V}\right) \cdot \frac{2}{N-2}. \quad (5.5)$$

Considering it is an infinite 2D network ($V \rightarrow \infty$), we get $N=6$, which means, though it may not be a flat system, it should still be a hexagonal network as graphene.

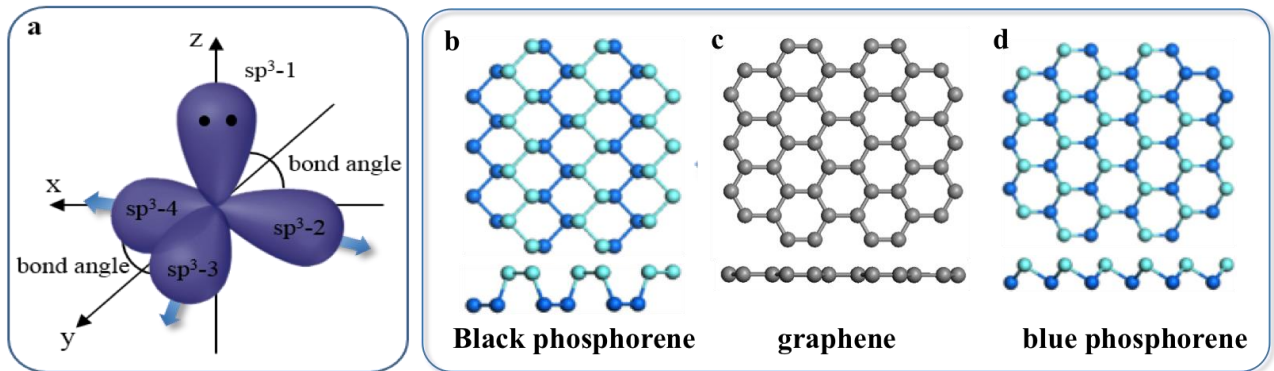


Figure 5.1 (a) Phosphorus atom's sp^3 hybridized orbital model. One of the sp^3 orbital is occupied by a lone electron pair and the other three orbitals form covalent bonds with other atoms. (b) Simple atomic structures of black phosphorene, graphene, and blue phosphorene. The grey, light blue, and dark blue spheres represent carbon atoms, upper level and lower level phosphorus atoms, respectively.

As stated that the sp^3 hybridization determines that phosphorene cannot maintain to be flat as graphene (Figure 5.1c), as well as the two-level system of all the predicted

phosphorene isomers (Figure 5.1b and d), a buckled honeycomb lattice is expected for the isomer prediction. Further, to prevent the 2D material from bending, as that in black and blue phosphorenes (Figure 5.1b and d), half of the phosphorus atoms should be lifted to the upper level and the other half remains down.

To maintain a high symmetry and stability, the unit cell is not proper to be too large. Thus a restriction of the number of phosphorus atoms in a unit cell is set to be no larger than 8 ($N_p \leq 8$). Elementary calculation results also suggest that if an atom along with its all three neighbors is in the same level, it is energetically unfavorable. Therefore, another rule is that no atom along with all its three neighbors can be in the same level.

Thus, for all the above considerations, the basic rules for the isomer searching method is set up as:

- i) A hexagonal network like graphene and all the other 2D materials is required, and all the phosphorus atoms are 3-coordinated;
- ii) Half of the phosphorus atoms are lifted to the upper level while the other half remain down;
- iii) The maximum number of phosphorus atoms in a unit cell is 8 ($N_p \leq 8$);
- iv) No atom along with its all three neighbors can be in the same level.

A simple program code based on these rules was then written to run the searching. Deleting all the repeated and mirror symmetrical ones, we array all the 14 isomer models according to the number of atoms in a unit cell as shown in Figure 5.2. For two-atom unit cell, there is only one isomer (Figure 5.2a). Four-atom unit cell has 2 isomers (Figure 5.2b), six-atom unit cell 2 isomers (Figure 5.2c), and eight-atom unit cell 9 isomers (Figure 5.2d, e, and f). These isomers were labeled in Arabic numbers from 1 to 14. The grey spheres represent the carbon atoms for the origin model, whereas the light blue spheres and dark blue spheres denote the lifted upper level and the bottom level phosphorus atoms. As it can be seen that each unit cell has half upper level atoms and half bottom level atoms, respectively.

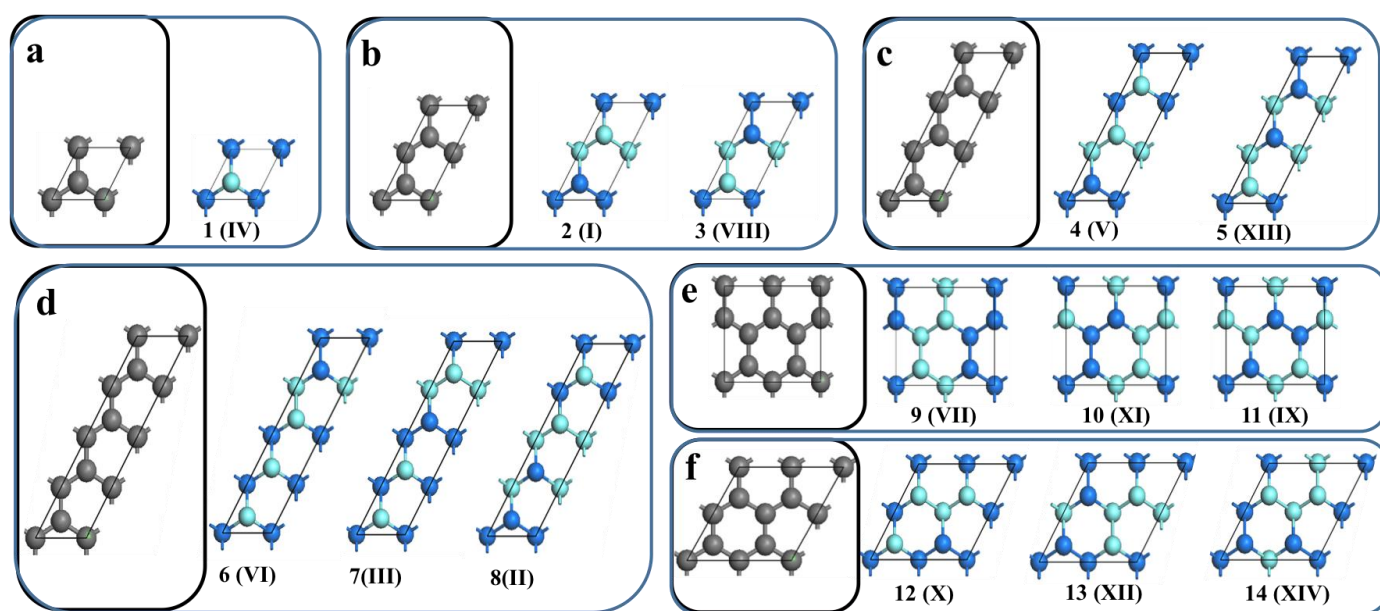


Figure 5.2 Phosphorene isomer models found under our isomer searching method. For two-atom unit cell, (a) shows the isomer found in a $(1,0)\times(0,1)$ unit cell. For four-atom unit cell, (b) shows the isomers found in a $(1,0)\times(0,2)$ unit cell. For six-atom unit cell, (c) shows the isomers

found in a (1,0)×(0,3) unit cell. For eight-atom unit cell, **(d)**, **(e)**, and **(f)** show the isomers found in (1,0)×(0,4), (2,0)×(1,2), (2,0)×(0,2) unit cell.

While these were only the elementary models that meet certain basic requirements, further optimizations of the structures were needed to acquire stable phases of phosphorene. During the optimization, adjustments of lattice parameters a_1 , a_2 , and θ , as well as the coordinates of the atoms, were allowed. Each above isomer model was optimized to get a set of the best lattice parameters by DFT calculations, which were performed via the VASP with PAW method. To consider van der Waals interaction in the system, DFT-D3 method was applied. A plane-wave cutoff energy of 400 eV was used and later all the structures were fully relaxed to have the lowest formation energy. The energy and force convergence criteria were 10^{-4} eV and 10^{-2} eV/Å, respectively. The Brillouin zone was sampled with different Monkhorst–Pack mesh k-points to meet the same separation criteria of 0.03 \AA^{-1} between k points. Standard DFT-PBE of GGA were employed to calculate the energy of the system while both DFT-PBE and the HSE hybrid functional method (here specifically HSE06) were used to investigate the band structures of the phosphorene isomers.

Figure 5.3 below shows the final result of our global searching method: all the 14 structures of phosphorene isomers after optimization. All these isomers were rearranged and relabeled in Roman numbers I to XIV according to their stability, and their old Arabic numbers were marked in the right brackets.

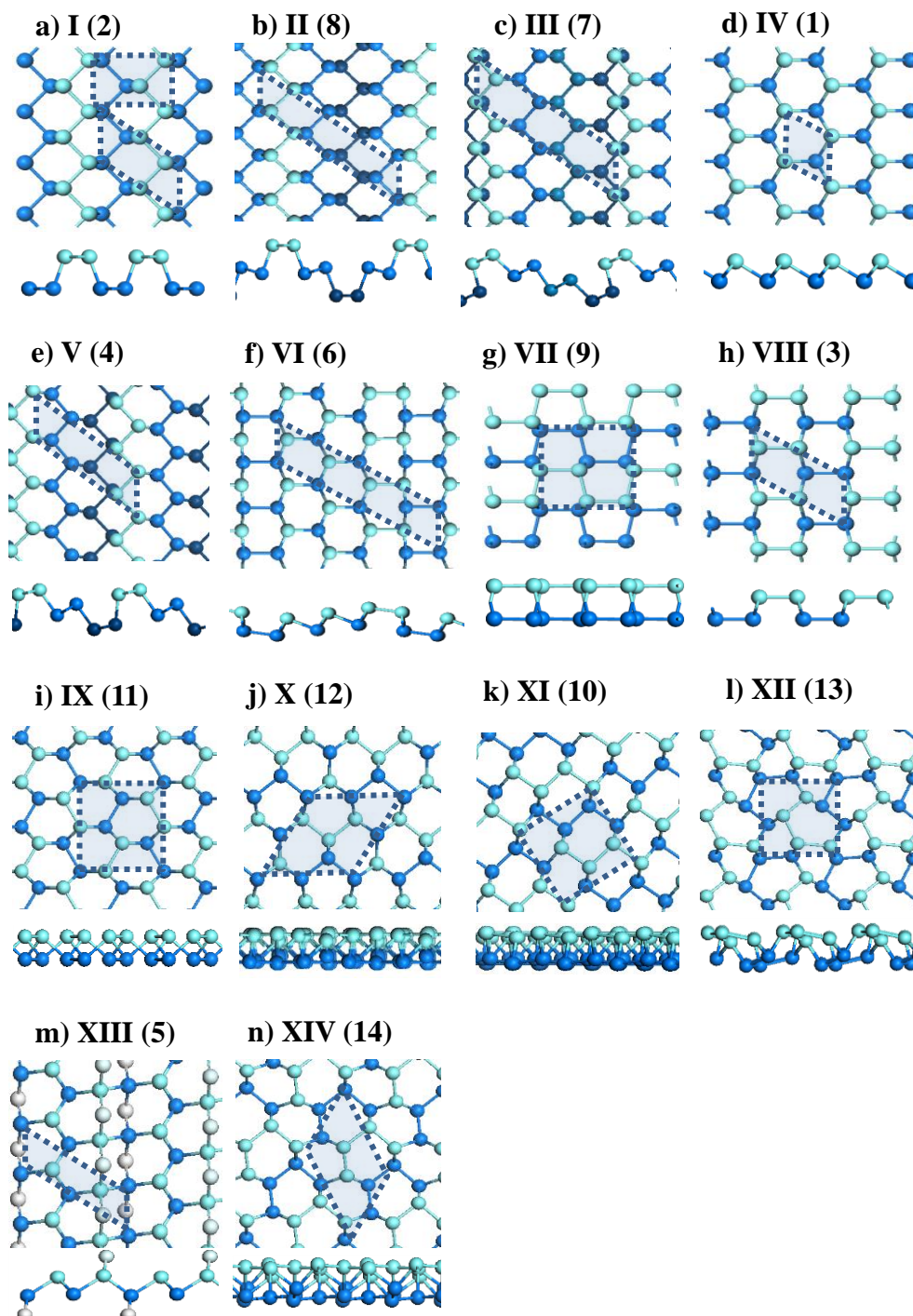


Figure 5.3 Optimized atomic structures of all the 14 phosphorene isomers found with our global searching method. (a-n) show the atomic structures of the 14 phosphorenes after optimization, labeled in Roman numerals from I to XIV, in top and side views, respectively. The dashed line draws out the unit cell of each phosphorene isomer. All the spheres represent phosphorus

atoms while they are on the upper level, their color lighter, and on the lower level, their color darker, except for the white spheres that stand for the phosphorus atoms bonding with only two neighbor atoms.

To give a whole picture of this searching method for all the possible phosphorene isomers, Figure 5.4 shows a schematic diagram of how this method was able to find phosphorene isomers with several well-known examples. In the center is the origin of the idea—graphene’s planar honeycomb lattice, as according to our analysis before, 2D materials usually tends to remain a hexagonal lattice. Due to phosphorus atom’s diverse bonding strategies resulting from its sp^3 hybridization, the arrangements of the atoms were countless. Further combing with certain rules regarding the stability and symmetry, the patterns were selected by simple program code and it was narrowed down to only 14 isomer models. And several of them were presented around the original graphene lattice in light and dark grey in Figure 5.4. Then lattice parameters a_1 , a_2 , and θ were adjusted and geometry optimization were conducted to get the final structures of phosphorene isomers which were energetically favorable, as shown in Figure 5.4.

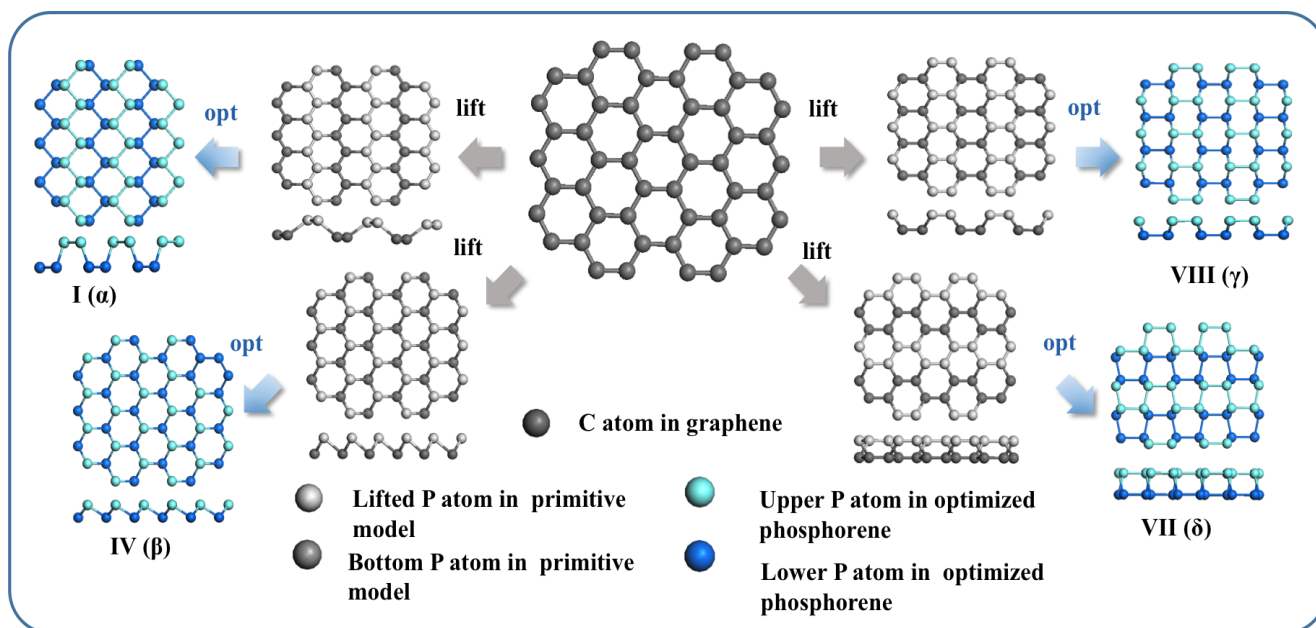


Figure 5.4 Schematic diagram of the searching method for finding the four most well-known isomers, α , β , γ , and δ -phosphorene, from the original graphene honeycomb lattice.

5.3 Discussion of the Predicted Phosphorene Isomers

For the 14 structures labeled from I to XIV shown in Figure 5.3, their optimized lattice parameters and energies obtained from both with DFT-PBE and HSE06 methods are presented in Table 5.1. It is clearly shown that all the lattice parameters a_1 , a_2 , and θ of different isomers are changed from the original set to fit a proper structure to minimize the total energy of the whole system. To be noticed, these sets of lattice parameters are all from the original isomer models' parameter sets after further optimization. But each phosphorene isomer has different ways to choose sets of lattice parameters. For example, phosphorene isomer I (P-I) is recognized as α -phosphorene (black

phosphorene). In Table 5.1, the lattice parameters for this isomer is 3.31 Å, 5.49 Å, and 52.9°, as shown in the unit cell marked with dashed line in Figure 5.3a. However, usually the reported lattice parameter set for α -phosphorene is another set as marked in the upper unit cell, though they are actually the same. This is for unification as this isomer is obtained from the optimization of the original isomer model 2 in Figure 5.2b.

Table 5.1 Optimized lattice parameters and energy differences of the phosphorene isomers: lattice parameters a_1 , a_2 (in Å), θ (°), and energy differences (eV/atom) between every isomer and isomer I (α -phosphorene) by PBE and HSE06.

	a_1	a_2	θ	$\Delta E^{(PBE)}$	$\Delta E^{(HSE)}$
I α	3.31	5.49	52.9	0.00	0.00
II	3.27	11.11	53.9	0.01	0.01
III	3.22	10.97	54.1	0.03	0.03
IV β	3.28	3.28	60.0	0.03	0.06
V	3.25	8.04	60.0	0.06	0.06
VI	3.20	12.69	59.8	0.07	0.08
VII δ	5.52	5.52	90.0	0.08	0.10
VIII γ	3.37	6.26	57.4	0.13	0.17
IX ϵ	5.74	6.10	90.0	0.16	0.18
X	6.34	6.50	60.0	0.16	0.19
XI	5.52	6.00	90.0	0.17	0.20
XII	5.25	6.02	90.0	0.20	0.24
XIII	3.07	8.46	50.3	0.21	0.24
XIV	6.33	6.42	61.4	0.28	0.33

The energies of the isomers in Table 5.1 are actually the energy differences between each isomer and P-I, since P-I is the reported most stable phase of phosphorus. It is clearly seen that the isomers found and optimized are all with high stability since the

energy differences are all in the range from 0 to 0.33 eV per atom. This demonstrates that our basic rules of the searching method are reasonable and effective to find the stable structures. Also the energy differences calculated with PBE and HSE methods are very similar, especially when the energy difference itself is small. Therefore, the calculation error caused by different methods is small and negligible. This indicates that with higher stability, the accuracy of energy calculation is higher. Since HSE method is usually recognized to be more accurate, the isomers will be discussed in terms of HSE calculation results.

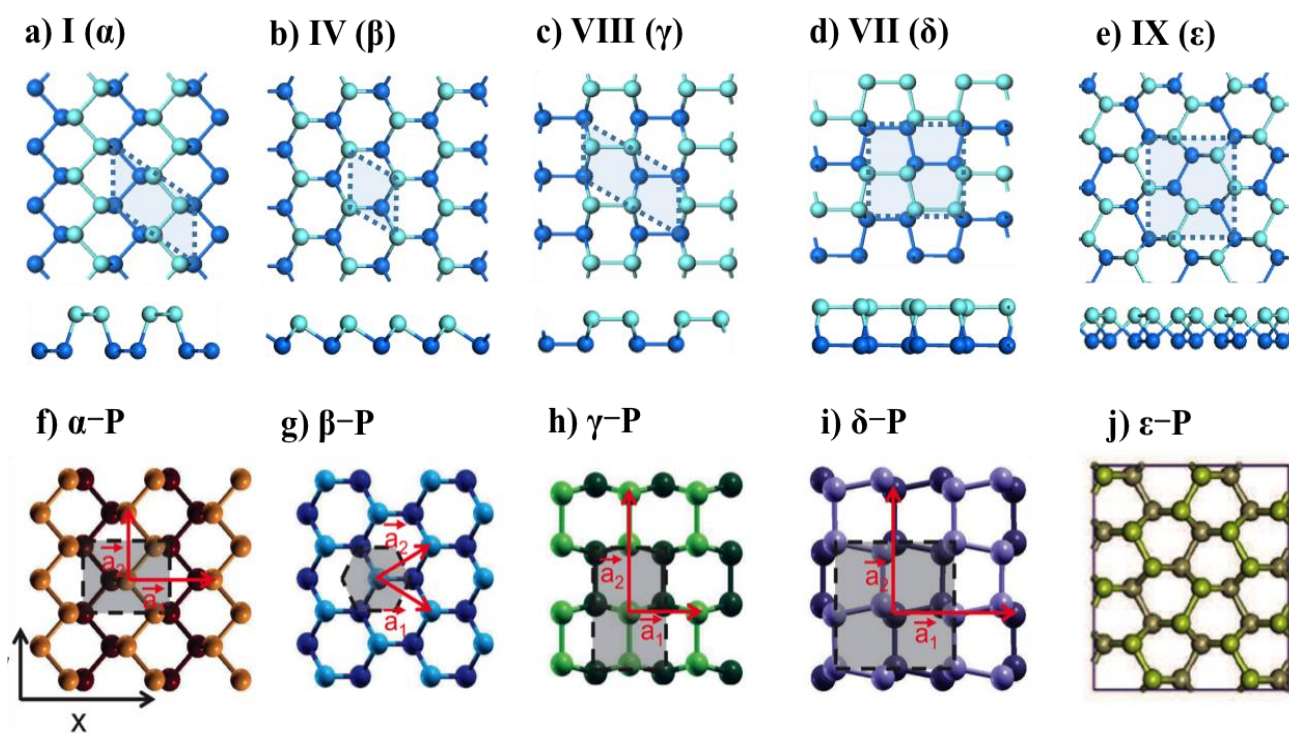


Figure 5.5 A comparison of the isomers found with our searching method and the well reported α -, β -, γ -, δ -, and ϵ -phosphorene. (a-e) show the atomic structures of P-I, P-IV, P-VIII, P-VII, and P-IX after optimization, in top and side views, respectively. (f-j) show the atomic

structures of α -, β -, γ -, δ -, and ϵ -phosphorene reported before. **(f-i)** Reprinted with permission from [189]. Copyright (2014) by the American Physical Society. **(j)** From reference [192], copyright (2016) by John Wiley & Sons, Inc. Reprinted by permission of John Wiley & Sons, Inc.

With further observation, it is not surprising that, according to the optimized structures, the isomers here labeled as P-I, P-IV, P-VIII, P-VII, and P-IX (Figure 5.5 a-e) are just the well-known α -, β -, γ -, δ -, and ϵ -phosphorene (Figure 5.5 f-j). As shown in Table 5.1, they are also very stable phases in our prediction, where taking P-I (α) phase as an energy criterion ($E_f=0$). The formation energy of P-IV (β) phase is just 0.06 eV per atom higher than that of P-I (α) phase, P-VIII (γ) 0.17 eV/atom higher, P-VII (δ) 0.10 eV/atom higher, and P-IX (ϵ) 0.18 eV/atom higher. These include all the most stable structures of phosphorene allotropes that have been predicted, which indicate that our searching method is, in some way, global and comprehensive.

Except for the successful prediction of these already known phosphorene isomers, several other structures are found to show great stability, such as P-II, P-III, P-V, and P-VI, whose energies are just 0.01, 0.03, 0.06, 0.08 eV per atom higher than α phase. The former two (P-II and P-III) are even more stable than P-IV (β), and P-V and P-VI are more stable than P-VIII (γ), P-VII (δ), and P-IX (ϵ) as shown in Figure 5.6a. Therefore, more attention has been focused on these relatively stable isomers, from P-I to P-VIII, whose energy difference with P-I (α) phase is lower than 0.175 eV per atom. Apart from the already well-known α -, β -, γ -, δ -, and ϵ -phosphorene (Figure 5.5 a-d),

atomic structures of P-II, P-III, P-V, and P-VI are presented in Figure 5.6 b-e, in which light blue spheres mean the upper level phosphorus atoms, dark blue spheres mean the lower level phosphorus atoms, and the darker the lower.

From top views (Figure 5.5 a-d and Figure 5.6 b-e), it clearly shows that the newly found isomers all share common features with the already reported ones: isomer P-II, P-III, and P-V have zigzag ridges in the same atomic level like those in P-I (α), in these new cases only more ridges in different levels within a unit cell; isomer P-VI is partial P-IV (β) phase and partial P-VIII (γ) phase. It is very interesting that all the structures (P-I (α), P-II, P-III, and P-V) with zigzag ridges are energetically more stable than isomers like P-VII (δ) phase which has armchair ridges in the same atomic level; P-VIII (γ) and P-VI phases, which do not have either zigzag ridges or armchair ridges, are energetically much less stable. So, to arrange the isomers according to energies, first comes the most stable P-I (α) phase, second are the P-II, P-III, P-V phases with zigzag ridges and the special P-IV (β) phase, then the energetically less favorable P-VI, P-VII (δ) and P-VIII (γ) phases. What should be noted is that zigzag ridge in phosphorene isomers is not only energetically favored as we predicted, but also affects phosphorene's electronic anisotropy. [20,228]

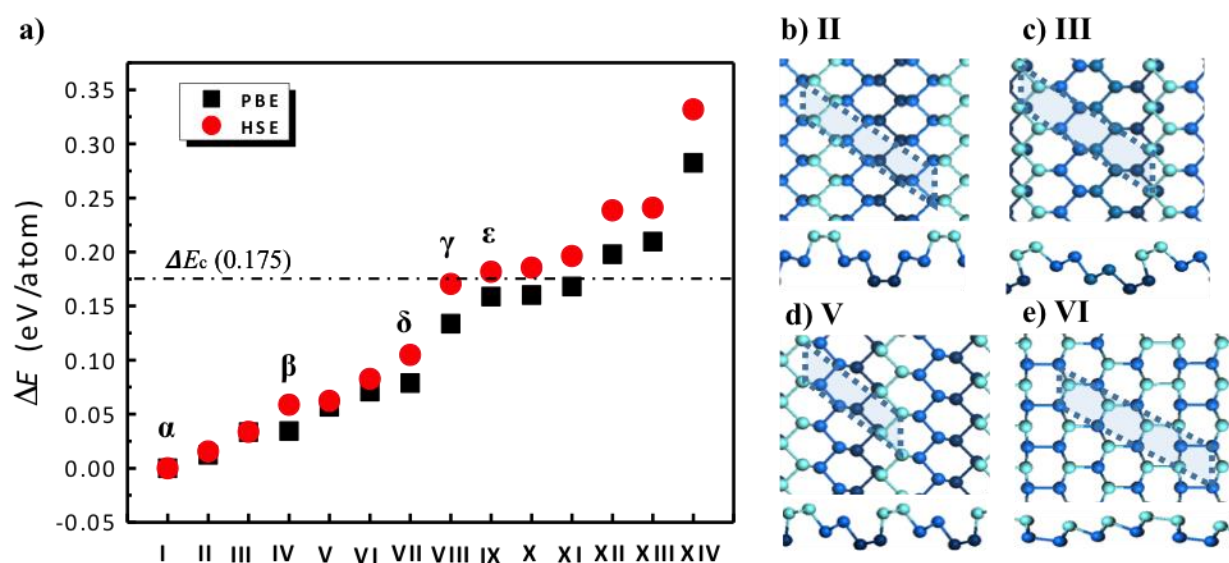


Figure 5.6 (a) Energy differences between all the isomers found and the black phosphorene with both PBE and HSE06 methods. Taking an energy difference of 0.175 eV per atom as a criterion, isomers with energy differences lower than it are considered as the relatively stable ones, including the widely reported α , β , γ , δ , and ϵ -phosphorene. (b), (c), (d), and (e) are the optimized atomic structures of the four newly found stable phosphorene isomers labeled as P-II, P-III, P-V, and P-VI, in top and side view, respectively. The dashed lines draw out the unit cell of each phosphorene isomer.

To further illustrate the structural similarities of the most stable P-I (α), P-II, P-III, P-V, and the special P-IV (β) phases, comparison has been made from different perspective. From side views, their structural features have been portrayed and simplified in the schematic diagram in Figure 5.7. In Figure 5.7 a-f, each of these phosphorene isomers is represented by combination of lines of different colors. Red lines represent isomer P-IV (β) and blue lines represent isomer P-I (α), *etc.* As indicated by the dashed line,

isomer P-IV (β) is composed by only χ unit, while its mirror symmetrical identity P-IV' (β') is composed by only χ' . Therefore, as the figure shows isomer P-I (α) is composed by χ and χ' unit in the arrangement of $\chi - \chi' - \chi - \chi' - \chi - \chi' \dots$, isomer P-II in the arrangement of $\chi - \chi - \chi' - \chi' - \chi - \chi - \chi' - \chi' - \chi \dots$, isomer P-V in the arrangement of $\chi - \chi' - \chi' - \chi - \chi' - \chi' - \chi - \chi' - \chi' - \chi \dots$, and isomer P-III in the arrangement of $\chi - \chi' - \chi' - \chi' - \chi - \chi' - \chi' - \chi' - \chi \dots$. What's more important is that these two elementary components are just the up-down reflection to each other. On the base of isomer P-IV (β), periodic flipping down of the χ unit to be the χ' , we can get the other four isomers, very similar to the conversion of black (P-I (α)) to blue (P-IV (β)) phosphorene by dislocation mentioned by David Tomanek . [188]

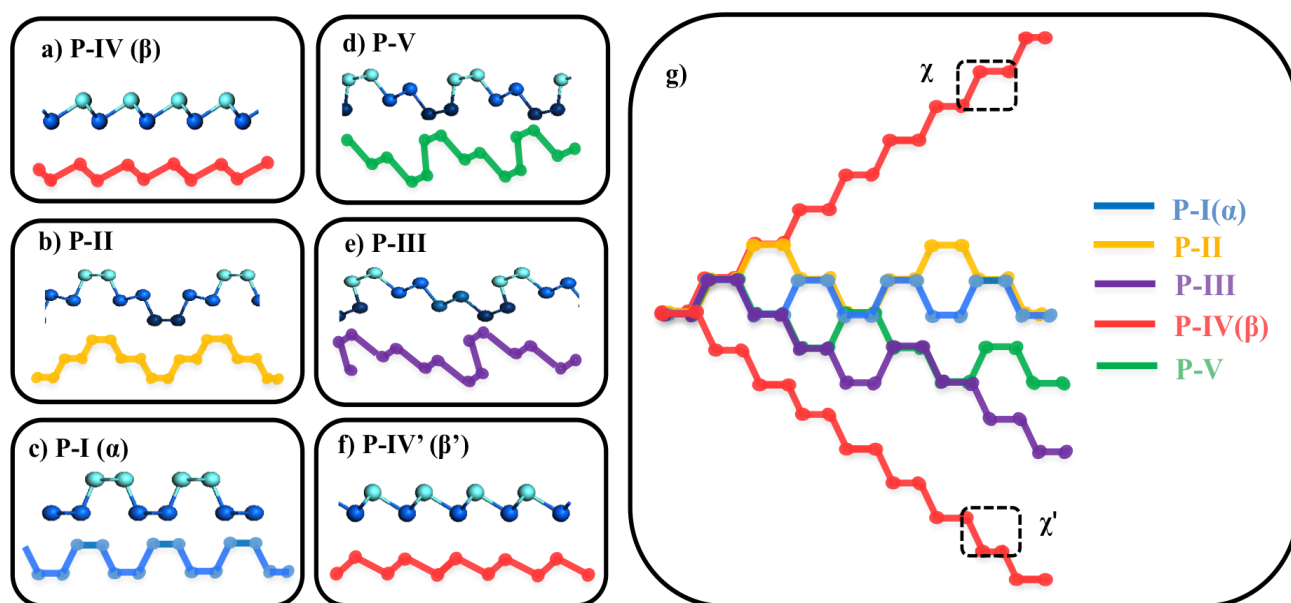


Figure 5.7 Structural comparison of the most stable phosphorene isomers. (a-f) Structural simplifications of P-IV, P-II, P-I, P-V, P-III, and P-IV', respectively. (g) Schematic diagram of structural similarities and differences of isomer P-I, P-II, P-III, P-IV and P-V. Side view images of these phosphorene isomers are seen as simply composed of χ and χ' elements. The top and bottom

red colored figures in (g) are two mirror symmetrical images of blue phosphorene (a) and (f).

To understand it in another way, this kind of structural similarities can result in the similar distribution of bond length and bond angle. In isomer P-IV (β), there is only one type of bond length as $\sim 2.25 \text{ \AA}$ and one type of bond angle as $\sim 94^\circ$, while isomer P-I (α) has bond lengths of ~ 2.22 and $\sim 2.25 \text{ \AA}$, and bond angles of $\sim 96^\circ$ and $\sim 102^\circ$. As for P-II, P-III, P-V isomers, there are little deviations but the major two sets of bond lengths around 2.22 and 2.25 \AA , and bond angles around 96° and 102° remain. This indicates that phosphorene structures favor these kinds of bond lengths and bond angles.

Furthermore, to study the electronic properties of the 14 phosphorene isomers, the electronic band structures as well as the vacuum level, conduction band minimum (CBM) and valence band maximum (VBM) were calculated with both PBE and HSE method. Figure 5.8 shows the electronic band structures of the eight most stable phosphorene isomers with HSE06 method, and Table 5.2 gives both PBE and HSE06 calculation results. From the two sets of results, it clearly shows that PBE calculation results are much lower than those of HSE06 methods. For example, with PBE method the band gap of BP (P-I (α)) is only 0.69 eV , which is much lower than the other experimental and theoretical data [229,230]. As PBE method is known to underestimate the band gap, electronic band structures are all presented at the HSE06 level in Figure 5.8 and the results of the band gaps of all the 14 found phosphorene isomers are plotted

in Figure 5.9.

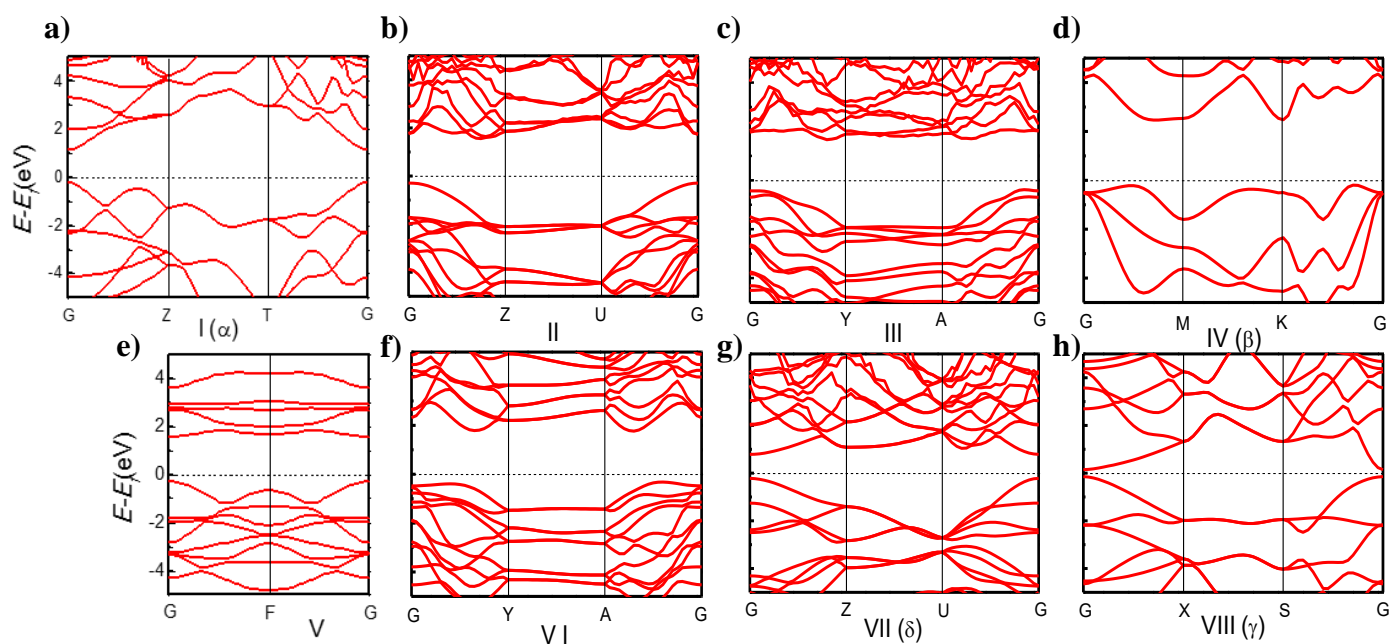


Figure 5.8 Band structures of the phosphorene isomers. Electronic band structures of the eight most stable phosphorene isomers, (a) P-I (α), (b) P-II, (c) P-III, (d) P-IV (β), (e) P-V, (f) P-VI, (g) P-VII (δ), and (h) P-VIII (γ) with HSE06 method.

Table 5.2 Band gap of the eight most stable phosphorene isomers with both PBE and HSE06 methods.

	I(α)	II	III	IV(β)	V	VI	VII(δ)	VIII(γ)
E_g(PBE)	0.69	1.08	1.33	1.83	1.11	1.31	0.34	0.07
E_g(HSE)	1.36	1.85	2.04	2.66	1.84	2.08	1.01	0.30

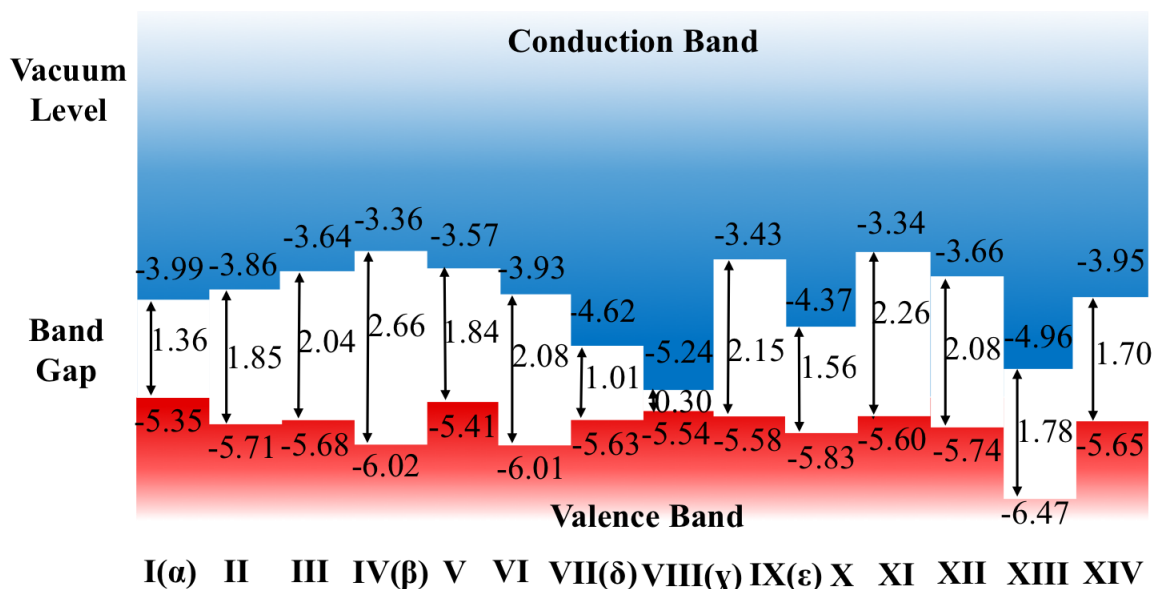


Figure 5.9 Band gaps of all the 14 found phosphorene isomers. The blue space represents the conduction band while the red space represents the valence band. Thus the white space in the middle denotes the band gap of each phosphorene.

It shows that BLP (P-IV(β)) is with the largest band gap of 2.66 eV while BP (P-I (α)) has a band gap of 1.36 eV. Isomer P-VI, though structurally very similar to BLP (P-IV(β)), has a much smaller band gap of 2.08 eV, as it's partially composed of P-VIII (γ) phase which possesses a only 0.30 eV band gap. Thus, in total, phosphorene isomers together possess a very wide range of band gaps (0.30 eV to 2.66 eV), which should be an advantage for photocatalysis and optoelectronic devices.

It is intriguing that band gaps of those isomers with zigzag ridges, P-I (α), P-II, P-III, and P-V, are somehow related to their structures. As shown in Figure 5.7, if P-I (α) can be seen as possessing one step up from the bottom atomic level in side view, there are

two steps in the structures of P-II and P-V and three steps of P-III phase. The band gaps follow this order as one step structure has 1.36 eV band gap (P-I (α)), two steps structures have 1.84 and 1.85 eV band gaps, and three steps structure has 2.04 eV band gap--the band gap is increasing with the number of steps. As zigzag ridges are already known to be very important to the electronic properties of BP, such as its anisotropic carrier mobility, it is not surprising that it has a relationship with phosphorenes' band structures, which could be exploited to specific electronic applications.

5.4 Summary

In this chapter, a global searching method for all the possible and stable phases of phosphorene was proposed. With careful consideration of symmetry, stability and phosphorus atom's bonding properties, basic rules for the searching method were set and a simple program code written to run the searching. After further adjustment of lattice parameters and geometry optimization, 14 phosphorene isomers were found with great stability. Within these 14 isomers, there include all the 5 reported most stable isomers of phosphorene-- α -, β -, γ -, δ -, and ϵ -phosphorene, which demonstrates that our searching method is reasonable and effective to find the stable structures. Except for these 5 already known isomers, 3 other isomers with comparable stability were found. Among these 3 isomers, P-II and P-III are even more stable than P-IV (β), whose energy is only 0.01 and 0.03 eV per atom higher than P-I (α). It is interesting that the newly

found isomers all share certain structural features with old stable ones. Specific bond lengths of ~ 2.22 and ~ 2.25 Å and bond angles of $\sim 96^\circ$ and $\sim 102^\circ$ are preferred in stable structures; the zigzag ridge in the same atomic level not only increases the stability but also has a relationship with the electronic properties of the phosphorene isomers. Furthermore, the whole isomer group shows a wide range of band gaps, from 0.30 eV to 2.66 eV, which enriches the potential of phosphorene's optoelectronic and electronic applications.

Chapter 6. Phosphorene CVD Growth on Catalyst Surfaces

6.1 Introduction

CVD method has been used to synthesize low dimensional materials for many decades, especially for the synthesis of large-area high-quality 2D materials. For example, the roll-to-roll production of 30-inch graphene films grown by CVD on copper substrates [36], the wafer-scale CVD growth of large domain size h-BN film [231], and the large-area MoS₂ atomic layers synthesized on SiO₂ substrates by CVD [232]. However, up to now, most phosphorene samples are obtained by exfoliating the bulk BP. Certainly, the CVD synthesis of large-area high-quality phosphorene is a crucial step towards the industrial applications. So is it possible to synthesize phosphorene by using the CVD method? As that for most 2D materials synthesis, the key of CVD synthesis is the selection of a proper substrate. For graphene, copper and nickel show distinctly different mechanisms of growth. Due to the lower solubility of carbon, the growth of graphene on Cu substrate becomes a surface reaction which leads to a high percentage of single layer comparing with nickel which has a much higher solubility of carbon in the bulk, resulting in the percentage increase in multilayer graphene [143]. So what about phosphorene? Which would be the best choice for the CVD synthesis of phosphorene among all those mostly used metal catalysts—Au, Ag, Cu, Ni, Ru, Pt, and Sn? According to our discussion in last chapter, there are isomers of phosphorene with

relative stability. Which isomer should be the most possible one to be synthesized on substrate by CVD method among all the widely reported ones?

Here we explore the potential of using the CVD method to synthesis large area 2D phosphorene by *ab initio* calculations. By carefully exploring the formation of various 2D phosphorene isomers, including α (black), β (blue), γ , and δ phases, we found that the blue phosphorene owns superior stability on most metal surfaces. Considering the solubility and the binding strengths between the phosphorene isomers and the catalyst surfaces, we showed that the Sn, Ag, Au are proper catalysts for the synthesis of easy transferable 2D blue phosphorene.

6.2 Theoretical Analysis of Phosphorene CVD Growth on Transition Metals

As stated in last chapter, we have found that many phosphorene isomers share similar stability. It is possible that in the relatively high temperature of CVD synthesis different phases of phosphorene may transform from each other. It is reasonable to question which one would be the most possible phase to be synthesized *via* CVD method. Here we only choose 4 most widely reported isomers, α -, β -, γ -, and δ -phosphorene, as the possible growing phases during the CVD process and build up the optimized models. The original lattice parameters of α , β , γ , and δ -phosphorene are from reference [189]. Their lattice parameters were further optimized and the final results are shown in Figure

6.1 and Table 6.1. It is seen in Table 6.1 that the parameters change very little from the original data. Except for the 4 phosphorene isomers used in the simulation, 7 transition metal surfaces were also modeled as for the catalyst substrates—Ag(111), Au(111), Cu(111), Ni(111), Pt(111), Ru(0001), and β -Sn(001) surfaces, since they are the most commonly used metal surfaces in CVD growth of 2D materials. All these seven metal surfaces were simulated by three-layer-thick slab models with all the atoms in the bottom layer fixed during the simulations. Metal slabs with optimized lattice parameters and structures are presented in Figure 6.2.

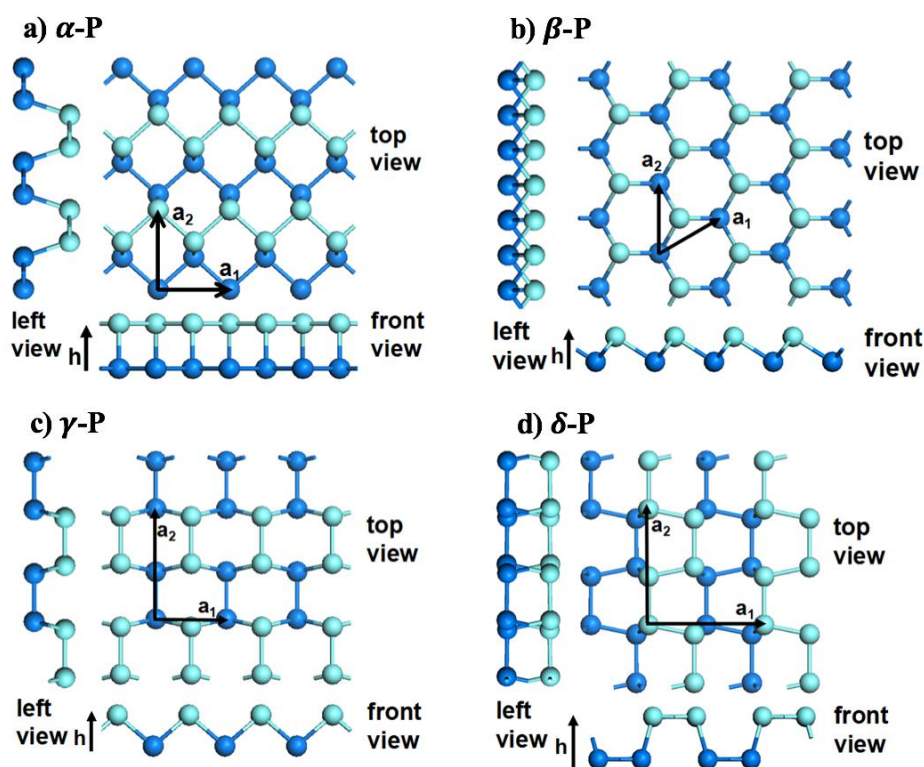


Figure 6.1 Optimized atomic structures of α , β , γ , and δ -phosphorene in vacuum in top, front, and left views. Lattice parameters are denoted with black lines. The light blue spheres represent the upper level phosphorene atoms while the dark blue spheres represent the bottom level phosphorus

atoms.

Table 6.1 Calculated parameters of the four phosphorene isomers used in this study. a , a_2 , and θ are the lattice parameters of the super cell models. E_f is the formation energy of the phosphorene isomer in vacuum.

	Super cell	Super cell	Super cell	E_f
	a_1 (Å)	a_2 (Å)	θ (°)	(eV/atom)
α	3.31	4.38	90	0.0
β	3.28	3.28	60	0.034
γ	3.37	5.28	90	0.133
δ	5.52	5.52	90	0.078

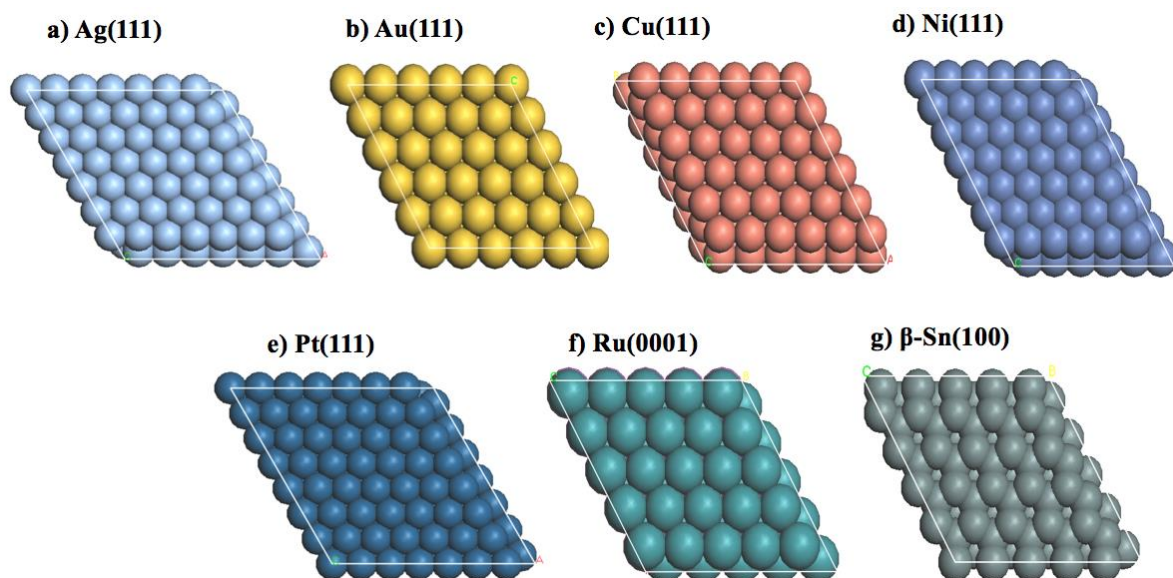


Figure 6.2 Optimized atomic structures of Ag(111), Au(111), Cu(111), Ni(111), Pt(111), Ru(0001) and β -Sn(100) surfaces.

Then let's come to the most difficult part that the four isomers of phosphorene were placed onto the seven metal substrates by carefully choosing the super cell size of the system, which ensures the lattice mismatch between the phosphorene and the substrate to be lower than 3%. The models were all PBC super cells along x- and y- axis. To avoid periodic image interaction along z-axis, all slabs were separated by a vacuum layer of $\sim 15 \text{ \AA}$.

Taking β -Sn(100) surface as an example for the substrate of this CVD reaction, four phosphorene isomers α , β , γ , and δ -phosphorene were fitted onto it. With careful optimization, four atomic structures of these models were obtained as shown in Figure 6.3. The distances between phosphorene and Sn substrate (parameter d in plots) are 2.98 \AA , 2.76 \AA , 2.51 \AA , and 2.89 \AA as for α , β , γ , and δ -phosphorene, respectively, much larger than those between phosphorene and other metals like Ni and Pt, indicating that the interactions between phosphorene isomers and Sn should be more like van der Waals interaction.

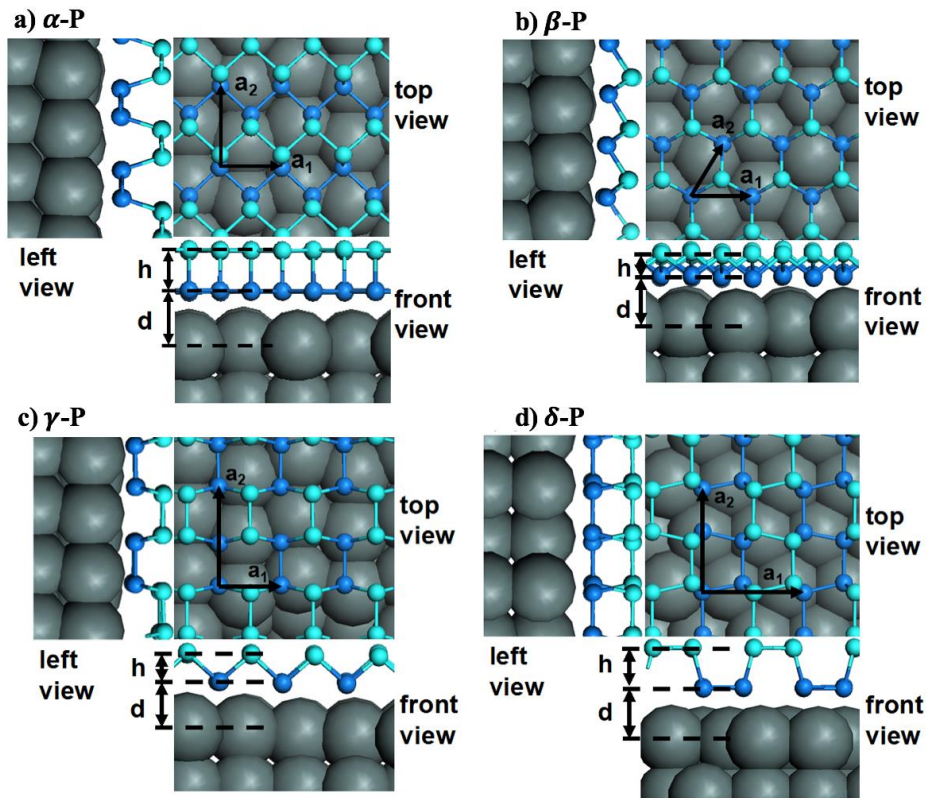


Figure 6.3 Atomic structures of (a) α -, (b) β -, (c) γ -, and (d) δ -phosphorene on β -Sn(100) surface in top view, front view and left view. The green, light blue and dark blue spheres represent tin, upper level and bottom level phosphorus atoms, respectively.

The stability of a phosphorene isomer on a metal surface is measured by its formation energy as defined below:

$$E_{f(i-p)} = (E_{i-p/M} - E_M - N_p * \epsilon_{\alpha-p})/N_p, \quad (6.1)$$

where $i = \alpha, \beta, \gamma$ or δ , and $E_{i-p/M}$, E_M , $\epsilon_{\alpha-p}$, and N_p represent the total energy of the $i - p$ on metal surface, the energy of the metal surface, the energy of α -P (BP) in the unit of eV/atom and the number of phosphorus atoms in a super cell. The definition of binding energy between $i - p$ and the metal surface can be written as

$$\begin{aligned}
 E_{b(i-p)} &= (E_{i-p/M} - E_M - N_p * \epsilon_{i-p})/N_p \\
 &= E_{f(i-p)} - E_{i-p} \\
 &= (E_{i-p/M} - E_M - N_p * \epsilon_{\alpha-p})/N_p - (\epsilon_{i-p} - \epsilon_{\alpha-p}), \tag{6.2}
 \end{aligned}$$

where E_{i-p} demonstrates the relative stability of $i-p$ in compare with the $\alpha-p$ (BP). This definition indicates that the strong binding energy may lead to the low formation energy and thus high stability on the metal substrate.

The formation energies of these four structures ($E_{fa} = -0.155$ eV/atom, $E_{fb} = -0.127$ eV/atom, $E_{fc} = -0.088$ eV/atom, $E_{fd} = -0.096$ eV/atom) clearly demonstrate the relative stability of the four phases, $\alpha > \beta > \delta > \gamma$, *i.e.* black phosphorene shows the highest stability on β -Sn(100) surface. However, the distances seem not directly correlated with the formation energies, though usually the smaller the distance the larger the formation energy. That could result from the structure differences of these four phases. Because of the sp^3 hybridization of phosphorus, there would be a variety of binding ways between atoms, therefore different layer structures. The stability of phosphorene on metal substrate would thus, be a complicated thing that not only distance between them should be taken into account but also other factors, such as layer thickness of phosphorene (parameter h in plots) and degree of lattice match between phosphorene isomer and the substrate.

For the interactions between different phases of phosphorene and different metal

substrates, we make a comparison of the optimized structures of α and β -phosphorene on β -Sn(100), Au(111) and Ni(111) surfaces as shown in Figure 6.4 and their charge density difference (CDD) plots as shown in Figure 6.5. The yellow and blue clouds in the figure represent charge density transfer through the interaction between the phosphorene isomer and the substrate, yellow for charge density increase and blue for decrease. It is clearly seen that few charge density transfer occurs on β -Sn(100) surface (Figure 6.5a), much more on Au(111) surface (Figure 6.5c), and most on Ni(111) surface (Figure 6.5e) even with charge density transfer on the second and third layers of Ni substrate and upper layer phosphorus atoms in black phosphorene. At the same time, the distances between black phosphorene and β -Sn(100), Au(111), Ni(111) surfaces are respectively 2.98 Å, 2.63 Å, and 1.75 Å, respectively (Figure 6.4a, e, and Figure 6.3a), which are in agreement with the charge density transfer data. These data indicate that the interactions between black phosphorene and Sn, Au, Ni change from weak van der Waals interaction to strong binding interaction. Similar tendency occurs in Figure 6.5b, d, and f for blue phosphorene and the distance between blue phosphorene and β -Sn(100), Au(111), Ni(111) surfaces are 2.66, 2.40, and 1.88 Å, respectively (Figure 6.4b, f and 6.3b).

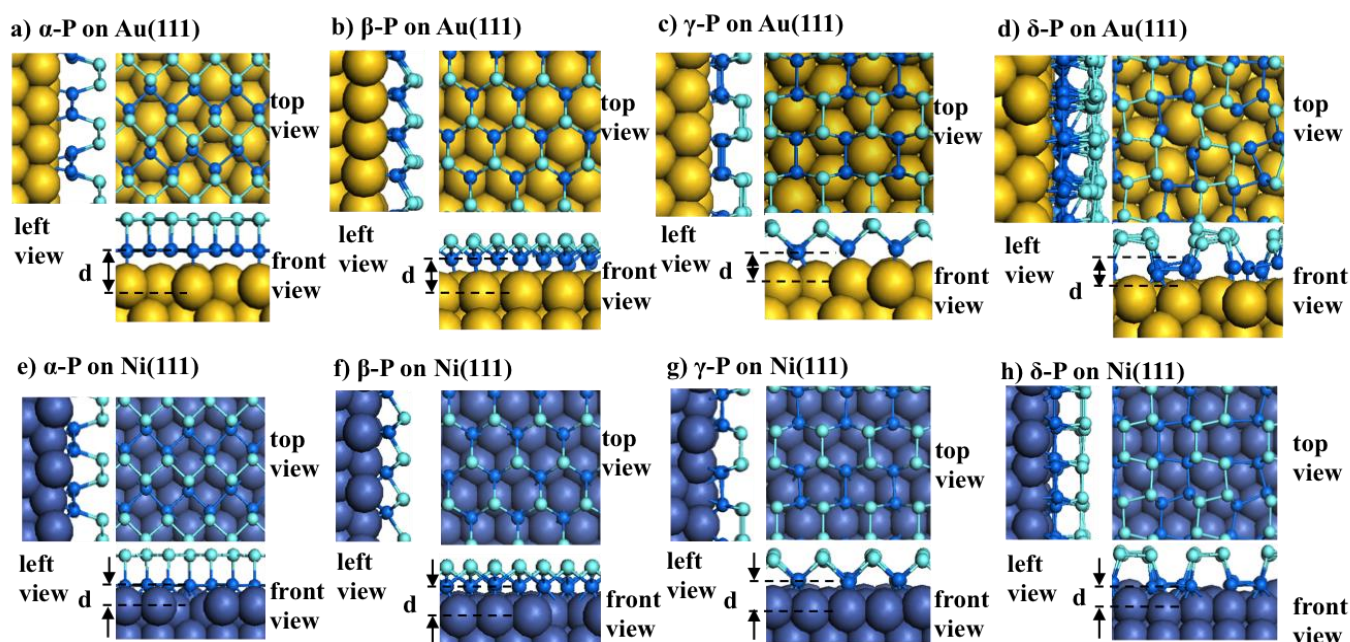


Figure 6.4 Optimized atomic structures of α , β , γ , and δ -phosphorene on (a-d) Au(111) and (e-h)

Ni(111) surfaces in top, front and left views. The yellow, purple, light blue and dark blue spheres represent the gold, nickel, upper level and bottom level phosphorus atoms.

As for the comparison between black and blue phosphorene on the same substrate, there is obviously much more charge density transfer happening between blue phosphorene and the substrate (Figure 6.5 a and b, c and d, e and f) and much shorter distance as well (Figure 6.4 a and b, e and f, Figure 6.3 a and b). This demonstrates the stronger bindings between blue phosphorene and β -Sn(100), Au(111), Ni(111) surfaces than those of black phosphorene. The structure differences could also be the explanation for the binding strength: the layer thickness of blue phosphorene is about 1.20 Å, much smaller than that of black phosphorene (2.19 Å), which leads upper phosphorus atoms to interact with the substrate, as shown in the Figure 6.5b, d, and f.

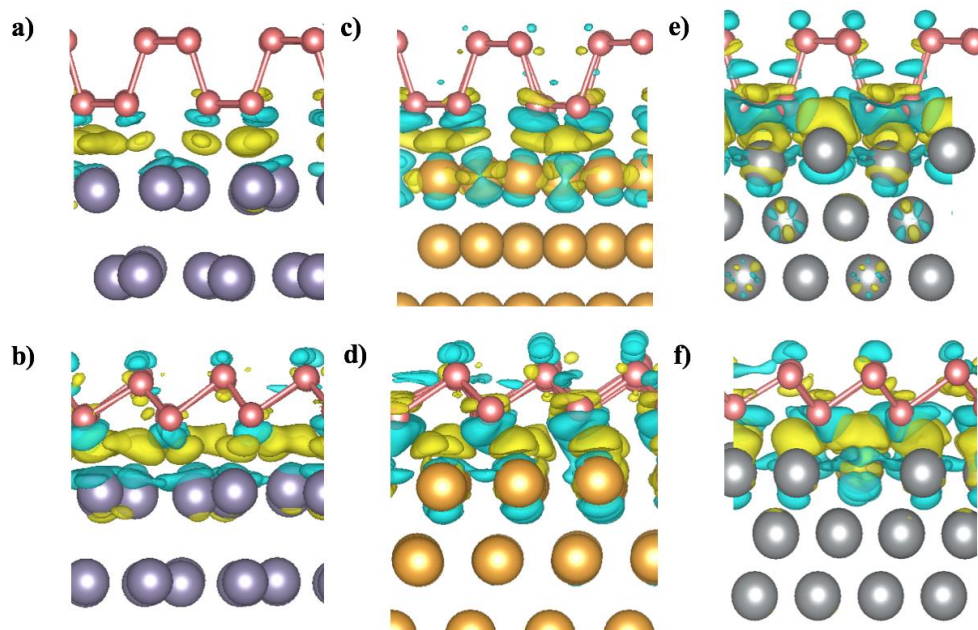


Figure 6.5 Charge Density Difference (CDD) Plots of phosphorene on substrates. (a), (c) and (e) are models of α -phosphorene on β -Sn(100), Au(111) and Ni(111) surfaces, while (b), (d) and (f) are β -phosphorene on β -Sn(100), Au(111) and Ni(111) surfaces, respectively. The iso-surface levels are all set at $0.002 e^*a_0^{-3}$, where e is the elementary electron charge, and a_0 is the Bohr radius.

In this study, we further explore the formation of all four kinds of phosphorene on β -Sn(100), Au(111), Ag(111), Cu(111), Ni(111), Pt(111), and Ru(0001) surfaces. As shown in Figure 6.6, optimized atomic structures of α -phosphorene on the seven metal substrates are presented. The distances are 2.98, 2.63, 2.61, 2.24, 1.75, 2.20, and 1.95 Å, respectively, *i.e.* β -Sn(100) > Au(111) > Ag(111) > Cu(111) > Pt(111) > Ru(0001) > Ni(111). This could also indicate the binding strengths between α -phosphorene and the substrates from very weak interaction to strong binding. All the other lattice parameters, the distances between phosphorene isomers and substrates, lattice mismatches during

the fitting, formation energies and binding energies are presented in Table 6.2.

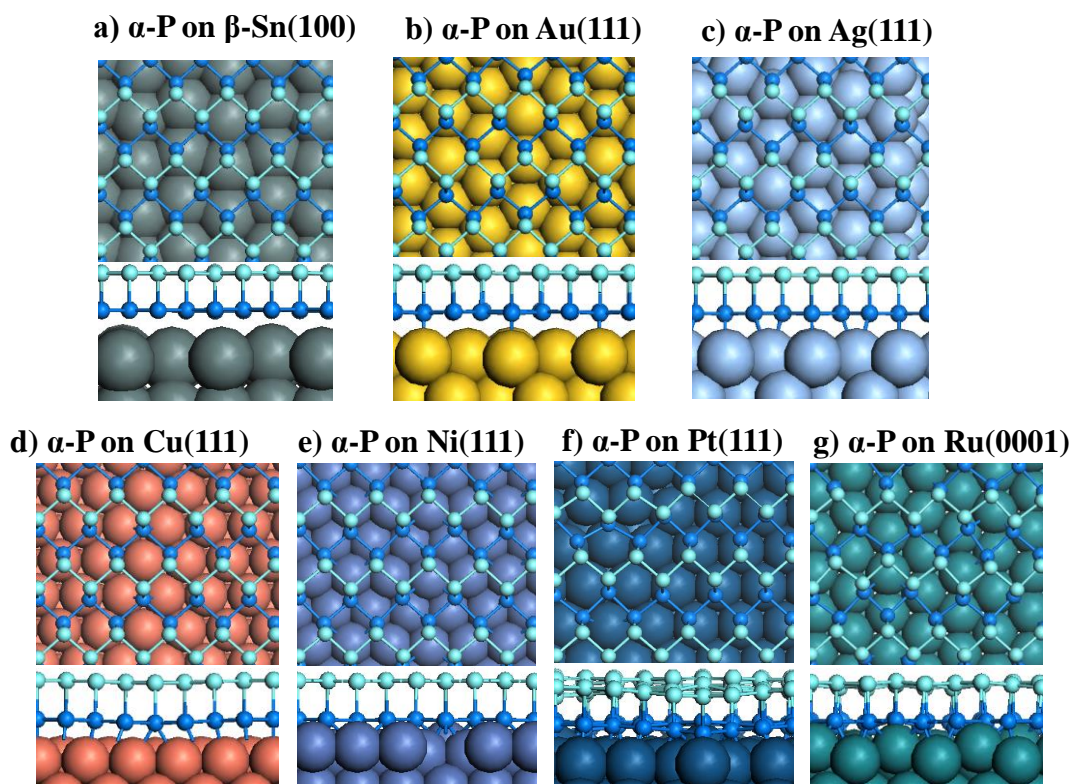


Figure 6.6 Optimized atomic structures of α -phosphorene on β -Sn(100), Au(111), Ag(111), Cu(111), Ni(111), Pt(111), and Ru(0001) surfaces in top and front views, respectively. The distances between α -phosphorene and the substrates are 2.98, 2.63, 2.61, 2.24, 1.75, 2.20, and 1.95 Å, respectively.

Table 6.2 Calculated parameters of all the phosphorene-on-substrate models. a and b are the lattice parameters of the modeled super cells. a_p , b_p , a_m and b_m represent the lattice mismatches (along a and b directions) in percentage for phosphorene and the metal substrates, respectively, in comparison with the freestanding phosphorene and bulk metal; d is the distance between the phosphorene and the metal substrate after optimization; E_f and E_b are the formation energy and binding energy as defined in this main text.

		Supercell	supercell	mismatch	mismatch	distance	E_f	E_b
		a (Å)	b (Å)	$a_p; b_p$ (%)	$a_m; b_m$ (%)	d (Å)	(eV/atom)	(eV/atom)
β-Sn(100)	α	23.17	21.90	0;0	0.5;1.4	2.98	-0.155	-0.155
	β	22.96	22.72	0;0	1.4;2.3	2.66	-0.127	-0.161
	γ	23.58	15.83	0;0	1.3;0.0	2.52	-0.088	-0.222
	δ	22.06	5.60	0;0.3	0.7;3.0	2.90	-0.096	-0.175
Au(111)	α	9.93	8.76	0;0	2.9;1.0	2.63	-0.226	-0.226
	β	22.96	22.96	0;0	2.8;2.8	2.40	-0.287	-0.321
	γ	10.11	21.10	0;0	1.0;2.1	2.44	-0.261	-0.395
	δ	55.16	11.03	0;0.1	0.3;3.0	2.42	-0.231	-0.309
Ag(111)	α	9.93	8.76	0;0	0.7;1.1	2.61	-0.243	-0.243
	β	19.96	19.96	0;0	1.3;1.3	2.39	-0.300	-0.335
	γ	10.23	26.70	0;0	2.2;2.6	2.26	-0.255	-0.388
	δ	5.56	49.14	0.2;0	3.0;1.8	2.57	-0.179	-0.258
Cu(111)	α	13.24	13.14	0.5;0	3.0;1.1	2.24	-0.381	-0.381
	β	9.98	9.98	0;0	2.4;2.4	2.16	-0.536	-0.570
	γ	10.23	26.70	0;0	0.1;0.5	2.00	-0.454	-0.587
	δ	22.24	21.84	0.1;0	3.0;1.3	2.20	-0.337	-0.415
Ni(111)	α	9.93	8.76	0;0	0.4;1.5	1.75	-0.795	-0.795
	β	9.98	9.98	0;0	1.1;1.1	1.88	-0.931	-0.965
	γ	10.23	21.36	0;0	2.6;1.0	1.83	-0.857	-0.991

	δ	22.24	21.84	0;0	0.8;1.2	1.83	-0.755	-0.834
Pt(111)	α	16.55	39.42	0;0	0.6;2.5	2.20	-0.618	-0.618
	β	16.63	16.63	0;0	0.1;0.1	1.99	-0.816	-0.850
	γ	13.64	37.38	0;0	1.7;2.8	1.90	-0.690	-0.824
	δ	33.36	5.52	0;0	0.8;1.6	2.05	-0.569	-0.648
	α	23.17	13.14	0;0	1.1;2.8	1.95	-0.649	-0.649
Ru(0001)	β	13.30	13.30	0;0	1.7;1.7	1.98	-0.821	-0.855
	γ	23.87	10.68	0;0	1.8;1.3	1.97	-0.828	-0.962
	δ	27.80	10.92	0;0	1.1;0.9	1.93	-0.698	-0.777

The formation and binding energies in Table 6.2 are plotted in Figure 6.7 to give a direct comparison. All the structures are relatively stable since the formation energies (Figure 6.7a) are negative. It is surprising that black phosphorene (α phase) is the most stable isomer only on the β -Sn(100) surface while blue phosphorene (β phase) is most stable on most other catalyst surfaces except the Ru(0001) surface. The formation energies of β and γ -phosphorene on Ru(0001) surface are almost the same. This may result from the strong binding between γ -phosphorene and the Ru(0001) surface. Thus, we predict that α -phosphorene, β -phosphorene and γ -phosphorene could be the most likely phases

of phosphorene to be synthesized by CVD method with large area and high quality.

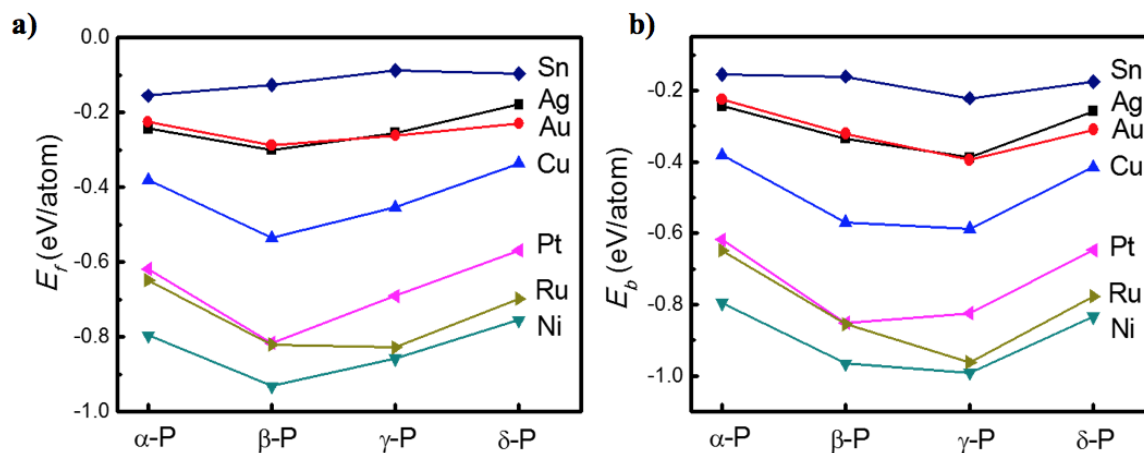


Figure 6.7 Formation energies (a) and binding energies (b) of α , β , γ , and δ -phosphorene on Ag(111), Au(111), Cu(111), Ni(111), Pt(111), Ru(0001) and β -Sn(100) surfaces, respectively.

For further consideration of device applications, the binding energies of this particular phosphorene to the substrate can't be too large since high binding energy would increase the difficulty of the transfer of phosphorene in later experiments. Therefore, as shown in Figure 6.7b, Pt, Ru and Ni with high binding energies should be excluded. Furthermore, phosphorus solubility in these metal substrates would also influence the CVD growth of phosphorene. According to Professor Hiroshi Okamoto's binary phase diagram [233], Sn, Ag, and Au almost have no phosphorus solubility while Cu has a solubility of about 1% at growth temperature. So, these three metal catalysts, compared with other tested metals would be better choices as substrates for phosphorene CVD growth.

Very recently, in 2016, Zhang *et al.* reported a molecular beam epitaxial growth of single-layer blue phosphorene on Au(111) by using black phosphorus as precursor at 230 °C. [196] As our theoretical calculation was done before 2016, this experimental work perfectly validates our prediction for the high possibility to synthesize blue phosphorene on Au(111) surface.

6.3 Summary

In this chapter, we explore the potential of using CVD method to synthesize large area 2D phosphorene films on metal surfaces by *ab initio* calculations. Four most widely reported phosphorene isomers, α , β , γ , and δ -phosphorene, were optimized as the test phases of phosphorene that would be possible to be synthesized during CVD growth. Seven metal substrates, β -Sn(100), Au(111), Ag(111), Cu(111), Ni(111), Pt(111), and Ru(0001), were used as the catalyst surfaces since they are the most widely used substrates. With careful fitting and optimization, our results show that black phosphorene (α -P) is the most stable phase of phosphorene on β -Sn(100) surface. It is surprising that on most other substrates, blue phosphorene (β -P) is the most likely isomer to be synthesized with CVD method as it is energetically favorable on these substrates. Further considering that the strong binding energies could lead to the failure of transfer process, weak binding strengths between isomers and substrates are more preferred. Thus the better choices for the synthesis of blue phosphorene should be Au(111) and Ag(111) surfaces. Ru(0001) surface, though very stable with γ -

phosphorene, is not a good choice for phosphorene CVD synthesis, since the binding strength between this substrate and the corresponding isomer is too strong.

Chapter 7. Conclusions

Since the first isolation of graphene films was awarded the Nobel Prize of Physics in 2010, a large amount of experimental and theoretical research has been done for the growth of large-area, high-quality, and single-crystal graphene films, especially its CVD synthesis as it is the most promising method for the future massive production of high quality graphene. However, further improvements of the graphene CVD growth, especially the increase of growth rate, need to be done and their mechanisms to be explored.

As a newly emerged 2D material, phosphorene has not been well researched yet. Theoretical works about phosphorene mainly focus on its fancy electronic and photoelectric properties. Due to its sp^3 hybridization strategy, phosphorene is predicted to have a large number of isomers. However, a systematic searching for all the possible isomers of phosphorene is still unavailable though there are many relative works. On the other hand, few experiments for the CVD growth of large-area high-quality phosphorene films have been reported successful though it is of great importance for realizing its great potentials in electronic and many other fields. Thus theoretical works about phosphorene CVD growth could be done first to shed light on its experimental exploration.

Motivated by the above challenges, this Mphil study concentrates on i) the mechanism of the ultrafast CVD growth of graphene with the supply of oxygen; ii) a global

searching method for finding all the possible phosphorene isomers; iii) the mechanism for the CVD growth of phosphorene on metal substrates.

- i) The mechanism of the ultrafast CVD growth of single-crystal large-area graphene with the continuous supply of oxygen and the round shape of grown graphene domains was investigated. The CI-NEB method was employed to investigate the energy barriers of the CH₄ decompositions with and without the existence of oxygen atoms. It shows that the continuous supply of oxygen could greatly reduce the energy barrier of CH₄ dissociation as well as the reaction energy for each step of the dissociation. This would dramatically increase the carbon flux around the edge of the graphene domains, changing the growth from a diffusion-limited process to a attachment-limited process, and then greatly increases the growth rate and results in the round shape of the graphene domains.

- ii) A global searching method for all the possible and stable phases of phosphorene was proposed since the previous predictions are all not systematic enough. By carefully considering phosphorus' bonding characteristics resulting from its sp³ hybridization, as well as the stability and symmetry of the isomers, 14 highly stable isomers were found with our buckled honeycomb lattice strategy and named P-I to P-XIV. Among these isomers, 5 are the most widely reported α -, β -, γ -, δ -, and ϵ -phosphorene and 3

new isomers that have not been predicted are also with comparable stability, in which P-II and P-III are even more stable than P-IV (β). This demonstrates that our searching method is effective and comprehensive to find all the stable phosphorene isomers. It is interesting that the newly found isomers share structural similarities with the old stable ones in term of bond lengths and bond angles, and preferring zigzag ridges. The entire isomer group also possesses a wide band gap range from 0.30 to 2.66 eV.

- iii) The potential of synthesizing phosphorene single-layer films on metal substrates *via* CVD method was investigated with DFT method. 4 most widely reported phosphorene isomers, α , β , γ , and δ -phosphorene, and 7 metal catalyst surfaces, β -Sn(100), Au(111), Ag(111), Cu(111), Ni(111), Pt(111), and Ru(0001), were all optimized as the test samples for the exploring of the possible isomers to be synthesized by the CVD method and the best substrate used. The calculation results shows that black phosphorene is most likely to be synthesized on tin surface while blue phosphorene can be synthesized by using gold and silver surfaces with CVD method. Although γ -phosphorene is the most stable isomer on Ru(0001) surface, their binding strength is too strong that would lead to the failure of further transfer.

This study firstly gives an explanation for the mechanism of the ultrafast growth of high quality graphene single layer films with the continuous oxygen supply. This would

surely shed light on the further development of a convenient and ultrafast CVD growth method of high quality graphene, which could probably lead to the final realization of industrial production of graphene for various applications. Then using a comprehensive method to find all the highly stable phosphorene isomers, and investigating the possible isomers and substrates in the CVD growth, the study proposes the most likely strategies for the CVD synthesis of high quality phosphorene. It provides adequate theoretical supports for the future realization of experimental phosphorene synthesis. Luckily this theoretical prediction was soon well demonstrated by the epitaxial growth of blue phosphorene on Au(111) later in 2016 by Zhang *et al.* [196] However, due to the limited computational resource, the study has focused only on several very specific circumstances: CH₄ decomposition on Cu(100) surface only; four kinds of phosphorene isomers on seven kinds of substrates. Additional research is recommended to confirm the role of oxygen on other surfaces and to examine the CVD growth of several other phosphorene isomers on other substrates.

Reference:

- 1 Novoselov, K. S.; Geim, A. K.; Morozov, S. V.; Jiang, D.; Zhang, Y.; Dubonos, S. V.; Grigorieva, I. V.; and Firsov, A. A. 2004, 'Electric Field Effect in Atomically Thin Carbon Films', *Science*, vol. 306, no. 5696, pp. 666-669.
- 2 Geim, A. K.; and Novoselov, K. S. 2007, 'The rise of graphene', *Nature Materials*, vol. 6, pp. 183-191.
- 3 Novoselov, K. S.; Geim, A. K.; Morozov, S. V.; Jiang, D.; Katsnelson, M. I.; Grigorieva, I. V.; Dubonos, S. V.; and Firsov, A. A. 2005, 'Two-dimensional gas of massless Dirac fermions in graphene', *Nature*, vol. 438, pp. 197-200.
- 4 Castro Neto, A. H.; Guinea, F.; Peres, N. M. R.; Novoselov, K. S.; and Geim, A. K. 2009, 'The electronic properties of graphene' *Reviews of Modern Physics*, vol. 81, no. 1, pp. 109-162.
- 5 Zhang, Y. B.; Tan, Y. W.; Stormer, H. L.; and Kim, P. 2005, 'Experimental observation of the quantum Hall effect and Berry's phase in graphene', *Nature*, vol. 438, pp. 201-204.
- 6 Li, X. S.; Cai, W.; An, J.; Kim, S.; Nah, J.; Yang, D.; Piner, R.; Velamakanni, A.; Jung, I.; Tutuc, E.; Banerjee, S. K.; Colombo, L.; and Ruoff, R. S. 2009, 'Large-Area Synthesis of High-Quality and Uniform Graphene Films on Copper Foils', *Science*, vol. 324, pp. 1312-1314.
- 7 Gao, J.; Yip, J.; Zhao, J.; Yakobson, B. I.; Ding, F. 2011, 'Graphene Nucleation on Transition Metal Surface: Structure Transformation and Role of the Metal Step Edge', *Journal of American Chemical Society*, Vol. 133, no. 13, pp. 5009-5015.
- 8 Wang, Y.; Shao, Y.; Matson, D.W.; Li, J.; Lin, Y. 2010, 'Nitrogen-Doped Graphene and Its Application in Electrochemical Biosensing', *ACS nano*, vol. 4, no. 4, pp. 1790-1798.
- 9 Lia, Z.; Shaheer Akhtara, M.; Kuka, J. H.; Kongc, B.; Yanga, O. 2012, 'Graphene application as a counter electrode material for dye-sensitized solar cell', *Materials Letters*, vol. 86, pp.96-99
- 10 Dean, C. R.; Young, A. F.; Meric, I.; Lee, C.; Wang, L.; Sorgenfrei, S.; Watanabe, K.; Taniguchi, T.; Kim, P.; Shepard, K. L.; Hone, J. 2010, 'Boron nitride substrates for high-quality graphene electronics', *Nature Nanotechnology*, vol. 5, pp. 722-726.

- 11 Giovannetti, G.; Khomyakov, P. A.; Brocks, G.; Kelly, P. J.; van den Brink, J. 2007, 'Substrate-induced band gap in graphene on hexagonal boron nitride: Ab initio density functional calculations', *Physical Review B*, vol. 76, pp. 073103.
- 12 Jin, C. H.; Lin, F.; Suenaga, K.; Iijima, S. 2009, 'Fabrication of a Freestanding Boron Nitride Single Layer and Its Defect Assignments', *Physical Review Letters*, vol. 102, pp. 195505.
- 13 Oshima, C.; Nagashima, A. 1997, 'Ultra-thin epitaxial films of graphite and hexagonal boron nitride on solid surfaces', *Journal of Physics: Condensed Matter*, vol. 9, pp. 1-20.
- 14 Pacile, D.; Meyer, J. C.; Girit, C. O.; Zettl, A. 2008, 'The two-dimensional phase of boron nitride: Few-atomic-layer sheets and suspended membranes', *Applied Physics Letters*, vol. 92, pp. 133107.
- 15 Vogt, P.; De Padova, P.; Quaresima, C.; Avila, J.; Frantzeskakis, E.; Asensio, M. C.; Resta, A.; Ealet, B.; Le Lay, G. 2012, 'Silicene: compelling experimental evidence for graphenelike two-dimensional silicon', *Physical Review Letters*, vol. 108, no. 15, pp. 155501.
- 16 Liu, C. C.; Feng, W. X.; Yao, Y. G. 2011, 'Quantum spin Hall effect in silicene and two-dimensional germanium', *Physical Review Letters*, vol. 107, no. 7, pp. 076802.
- 17 Lebegue, S.; Eriksson, O. 2009, 'Accurate electronic band gap of pure and functionalized graphene from GW calculations', *Physical Review B*, vol. 79, no. 24, pp. 245117.
- 18 Fleurence, A.; Friedlein, R.; Ozaki, T.; Kawai, H.; Wang, Y.; Yamada-Takamura, Y. 2012, 'Experimental evidence for epitaxial silicene on diboride thin films', *Physical Review Letters*, vol. 108, no. 24, pp. 245501.
- 19 Lalmi, B.; Oughaddou, H.; Enriquez, H.; Kara, A.; Vizzini, S.; Ealet, B.; Aufray, B. 2010, 'Epitaxial growth of a silicene sheet', *Applied Physics Letters*, vol. 97, no. 22, pp. 223109.
- 20 Liu, H.; Neal, A. T.; Zhu, Z.; Luo, Z.; Xu, X. F.; Tomanek, D.; Ye, P. D. D. 2014, 'Phosphorene: an unexplored 2D semiconductor with a high hole mobility', *Acs Nano*, vol. 8, no. 4, pp. 4033-41.
- 21 Dai, J.; Zeng, X. C. 2014, 'Bilayer Phosphorene: Effect of Stacking Order on Bandgap and Its Potential Applications in Thin-Film Solar Cells', *The Journal of*

- Physical Chemistry Letters*, vol. 5, no. 7, pp. 1289-1293.
- 22 Peng, X. H.; Wei, Q.; Copple, A. 2014, 'Strain-engineered direct-indirect band gap transition and its mechanism in two-dimensional phosphorene', *Physical Reviews B*, vol. 90, no. 8, pp. 085402.
 - 23 Wei, Q.; Peng, X. H. 2014, 'Superior mechanical flexibility of phosphorene and few-layer black phosphorus', *Applied Physics Letter*, vol. 104, no. 25, pp. 251915.
 - 24 Reich, E. S. 2014, 'Phosphorene excites materials scientists', *Nature*, vol. 506, pp. 19.
 - 25 Radisavljevic, B.; Radenovic, A.; Brivio, J.; Giacometti, V.; Kis, A. 2011, 'Single-layer MoS₂ transistors', *Nature Nanotechnology*, vol. 6, pp. 147.
 - 26 Mak, K. F.; Lee, C.; Hone, J.; Shan, J.; Heinz, T. F. 2012, 'Atomically thin MoS₂: a new direct-gap semiconductor', *Physical Review Letters*, vol. 105, no. 13, pp. 136805.
 - 27 Splendiani, A.; Sun, L.; Zhang, Y. B.; Li, T. S.; Kim, J.; Chim, C. Y.; Galli, G.; Wang, F. 2010, 'Emerging photoluminescence in monolayer MoS₂', *Nano Letters*, vol. 10, no. 4, pp. 1271.
 - 28 Wang, Q. H.; Kalantar-Zadeh, K.; Kis, A.; Coleman, J. N.; Strano, M. S. 2012, 'Electronics and optoelectronics of two-dimensional transition metal dichalcogenides', *Nature Nanotechnology*, vol. 7, no. 11, pp. 699-712.
 - 29 Li, Y. G.; Wang, H. L.; Xie, L. M.; Liang, Y. Y.; Hong, G. S.; Dai, H. J. 2011, 'MoS₂ nanoparticles grown on graphene: an advanced catalyst for the hydrogen evolution reaction', *Journal of the American Chemical Society*, vol. 133, no. 19, pp. 7296-9.
 - 30 Morgenstern, M. 2011, 'Scanning tunneling microscopy and spectroscopy of graphene on insulating substrates', *Physica Status Solidi B*, vol. 248, no.11, pp. 2423-2434.
 - 31 Luo, A. P.; Liu, M.; Wang, X. D.; Ning, Q. Y.; Xu, W. C.; Luo, Z. C. 2015, 'Few-layer MoS₂-deposited microfiber as highly nonlinear photonic device for pulse shaping in a fiber laser', *Photonics Research*, vol. 3, A69-A78.
 - 32 Ling, Z.; Ren, C. E.; Zhao, M. Q.; Yang, J.; Giammarco, J. M.; Qiu, J. S.; Barsoum, M. W.; Gogotsi, Y. 2014, 'Flexible and conductive MXene films and nanocomposites with high capacitance', *Proceedings of the National Academy of Sciences of the United States of America*, vol. 111, no. 47, pp. 16676-81.

- 33 Nistor, R. A.; News, D. M.; Martyna, G. J. 2011, 'Crown Graphene Nanomeshes: Highly Stable Chelation-Doped Semiconducting Materials', *Acs Nano*, vol. 5, pp. 3096-3103.
- 34 Aghigh, A.; Alizadeh, V.; Wong, H. Y.; Islam, M. S.; Amin, N.; Zaman, M. 2015, 'Recent advances in utilization of graphene for filtration and desalination of water: A review', *Desalination*, vol. 365, pp. 389-397.
- 35 Lisnard, L.; Dolbecq, A.; Mialane, P.; Marrot, J.; Codjovi, E.; Secheresse, F. 2005, 'Molecular and multidimensional polyoxotungstates functionalized by {Cu(bpy)}²⁺ groups', *Dalton Transactions*, pp. 3913-20.
- 36 Bae, S.; Kim, H.; Lee, Y.; Xu, X. F.; Park, J. S.; Zheng, Y.; Balakrishnan, J.; Lei, T.; Kim, H. R.; Song, Y. I.; Kim, Y. J.; Kim, K. S.; Ozyilmaz, B.; Ahn, J. H.; Hong, B. H.; Iijima, S. 2010, 'Roll-to-roll production of 30-inch graphene films for transparent electrodes', *Nature Nanotechnology*, vol. 5, no. 8, pp. 574-8.
- 37 Reina, A.; Jia, X. T.; Ho, J.; Nezich, D.; Son, H. B.; Bulovic, V.; Dresselhaus, M. S.; Kong, J. 2009, 'Large area, few-layer graphene films on arbitrary substrates by chemical vapor deposition', *Nano Letters*, vol. 9, no.1, pp. 30-5.
- 38 Bonaccorso, F.; Sun, Z.; Hasan, T.; Ferrari, A. C. 2010, 'Graphene photonics and optoelectronics', *Nature Photonics*, vol. 4, pp. 611-622.
- 39 Ci, L.; Song, L.; Jin, C. H.; Jariwala, D.; Wu, D. X.; Li, Y. J.; Srivastava, A.; Wang, Z. F.; Storr, K.; Balicas, L.; Liu, F.; Ajayan, P. M. 2010, 'Atomic layers of hybridized boron nitride and graphene domains', *Nature Materials*, vol. 9, no. 5, pp. 430-435.
- 40 Wu, B.; Geng, D.; Xu, Z.; Guo, Y.; Huang, L.; Xue, Y.; Chen, J.; Yu, G. and Liu, Y. 2013, 'Self-organized graphene crystal patterns', *NPG Asia Materials*, vol. 5, no. 2, e36.
- 41 Mouras, S.; Hamm, A.; Djurado, D. 1987, 'Synthèse de composés d'insertion avec MF_x (M=Mo, W, Re, Nb, Ta, Ti, Nb, I). On forme le fluorure in situ à partir des éléments, puis on fait l'insertion dans le graphite sous atmosphère de fluor', *Revue de Chimie Minerale*, vol. 24, no. 5, pp. 572-582.
- 42 DiVincenzo, D. P.; Mele, E. J. 1984, 'Self-consistent effective-mass theory for intralayer screening in graphite intercalation compounds', *Physical Review B*, vol. 29, no. 4, pp. 1685-1694.

- 43 Ruess, G.; Vogt, F. 1984, 'Höchstlamellarer Kohlenstoff aus Graphitoxhydroxyd', *Monatshefte für Chemie*, vol. 78, pp. 222-242.
- 44 Meyer, J.; Geim, A. K.; Katsnelson, M. I.; Novoselov, K. S.; Booth, T. J.; Roth, S. 2007, 'The structure of suspended graphene sheets', *Nature*, vol. 446, no. 7131, pp. 60–63.
- 45 Kroto, H. W.; Heath, J. R.; O'Brien, S. C.; Curl, R. F.; Smalley, R. E. 1985, ' ', *Nature*, vol. 318, pp. 162-163.
- 46 Iijima, S. 1991, 'Helical microtubules of graphitic carbon', *Nature*, vol. 354, pp. 56-58.
- 47 U. S. Army Materiel Command, source: <http://flickr.com/photos/10393857@N03/6795812766>.
- 48 Winter, C.; Bignardi, L. 2015, 'Time-resolved electron spectroscopy in Graphene with High Harmonic radiation'. Retrieved November 29, 2016, from Physikalisches Institut, web site: <http://www.uni-muenster.de/Physik.PI/Zacharias/research/graphene/graphene.html>.
- 49 Novoselov, K. S.; Jiang, Z.; Zhang, Y.; Morozov, S. V.; Stormer, H. L.; Zeitler, U.; Maan, J. C.; Boebinger, G. S.; Kim, P.; Geim, A. K. 2007, 'Room-Temperature Quantum Hall Effect in Graphene', *Science*, vol. 315, no. 5817, pp. 1379 .
- 50 Lee, C.; Wei, X. D.; Kysar, J. W.; Hone, J. 2008, 'Measurement of the elastic properties and intrinsic strength of monolayer graphene', *Science*, vol. 321, no. 5887, pp. 385.
- 51 Balandin, A. A.; Ghosh, S.; Bao, W. Z.; Calizo, I.; Teweldebrhan, D.; Miao, F.; Lau, C. N. 2008, 'Superior thermal conductivity of single-layer graphene', *Nano Letters*, vol. 8, no. 3, pp. 902.
- 52 Levendorf, M. P.; Ruiz-Vargas, C. S.; Garg, S.; Park, J. 2009, 'Transfer-free batch fabrication of single layer graphene transistors', *Nano Letters*, vol. 9, no. 12, pp. 4479-4483.
- 53 Dan, Y. P.; Lu, Y.; Kybert, N. J.; Luo, Z. T.; Johnson, A. T. C. 2009, 'Intrinsic response of graphene vapor sensors', *Nano Letters*, vol. 9, no. 4, pp. 1472-5.
- 54 Robinson, J. T.; Perkins, F. K.; Snow, E. S.; Wei, Z. Q.; Sheehan, P. E. 2008, 'Reduced graphene oxide molecular sensors', *Nano Letters*, vol. 8, no. 10, pp. 3137-40.

- 55 Tang, L. H.; Wang, Y.; Li, Y. M.; Feng, H. B.; Lu, J.; Li, J. H.; 2009, 'Preparation, Structure, and Electrochemical Properties of Reduced Graphene Sheet Films', *Advanced Functional Materials*, vol. 19, pp. 2782-89.
- 56 Wang, X.; Zhi, L. J.; Mullen, K.; 2008, 'Transparent, conductive graphene electrodes for dye-sensitized solar cells', *Nano Letters*, vol. 8, no. 1, pp. 323-7.
- 57 Park, S.; Ruoff, R. S. 2009, 'Chemical methods for the production of graphenes', *Nature Nanotechnology*, vol. 4, pp. 217-224.
- 58 Liu, Y. H.; Xue, J. S.; Zheng, T.; Dahn, J. R. 1996, 'Mechanism of lithium insertion in hard carbons prepared by pyrolysis of epoxy resins', *Carbon*, vol. 34, no. 2, pp. 193-200.
- 59 Jang, B. Z.; Zhamu, A. 2008, 'Processing of nanographene platelets (NGPs) and NGP nanocomposites: a review', *Journal of Materials Science*, vol. 43, no. 15, pp. 5092.
- 60 Akinwande, D.; Tao, L.; Yu, Q.; Lou, X.; Peng, P.; Kuzum, D. 2015, 'Large-Area Graphene Electrodes: Using CVD to facilitate applications in commercial touchscreens, flexible nanoelectronics, and neural interfaces', *IEEE Nanotechnology Magazine*, vol. 9, no. 3, pp. 6–14.
- 61 "Graphene™ – Graphene Infused 3D Printer Power-30 Lbs-\$499.95", *Noble3DPrinters*. Retrieved 29 November 2016, web site: www.noble3dprinters.com.
- 62 "Graphene Uses & Applications". *Graphenea*. Retrieved 29 November 2016, web site: <http://www.graphenea.com/pages/graphene-uses-applications#.WD0EGaJ97kI>.
- 63 Li, L.; Yu, Y.; Ye, G. J.; Ge, Q.; Ou, X.; Wu, H.; Feng, D.; Chen, X. H. and Zhang, Y. 2014, 'Black phosphorus field-effect transistors', *Nature Nanotechnology*, vol. 9, pp. 372-377.
- 64 Wei, Q. and Peng, X. 2014, 'Superior mechanical flexibility of phosphorene and few-layer black phosphorus', *Applied Physics Letters*, vol. 104, no. 25, pp. 251915.
- 65 Jiang, J. W. and Park, H. S. 2014, 'Negative poisson's ratio in single-layer black phosphorus', *Nature Communications*, vol. 5, no. 4727.
- 66 Xia, F.; Wang, H.; Jia, Y. 2014, 'Rediscovering black phosphorus as an anisotropic layered material for optoelectronics and electronics', *Nature*

- Communications*, vol. 5, no. 4458.
- 67 Kou, L.; Chen, C. and Smith, S. C. 2015, 'Phosphorene: Fabrication, Properties, and Applications', *The Journal of Physical Chemistry Letters*, vol. 6, no. 14, pp. 2794–2805
- 68 Fei, R. and Yang, L. 2014, 'Strain-engineering the anisotropic electrical conductance of few-layer black phosphorus', *Nano Letters*, vol. 14, no. 5, pp. 2884–2889
- 69 Qin, G.; Yan, Q.-B.; Qin, Z.; Yue, S.-Y.; Cui, H.-J. Zheng, Q.-R. and Su, G. 2014, 'Hinge-like structure induced unusual properties of black phosphorus and new strategies to improve the thermoelectric performance', *Scientific Reports*, 2014, vol. 4, no. 6946.
- 70 Ong, Z.-Y.; Cai, Y.; Zhang, G. and Zhang, Y.-W. 2014, 'Strong Thermal Transport Anisotropy and Strain Modulation in Single-Layer Phosphorene', *The Journal of Physical Chemistry C*, vol. 118, pp. 25272–25277
- 71 Jain, A. and McGaughey, A. J. H. 2014, 'Strongly anisotropic in-plane thermal transport in single-layer black phosphorene', *Scientific Reports*, vol. 5, no. 8501.
- 72 Fei, R.; Faghaninia, A.; Soklaski, R.; Yan, J.-A.; Lo, C. and Yang, L. 2014, 'Enhanced Thermoelectric Efficiency via Orthogonal Electrical and Thermal Conductances in Phosphorene', *Nano Letters*, vol. 14, no. 11, pp. 6393–6399.
- 73 Dragoman, D.; Dragoman, M. 2007, 'Giant thermoelectric effect in graphene', *Applied Physics Letters*, vol. 91, no. 20, pp. 203116.
- 74 Balandin, A. A. 2011, 'Thermal properties of graphene and nanostructured carbon materials', *Nature Materials*, vol. 10, pp. 569-581.
- 75 Sahoo, S.; Gaur, A. P. S.; Ahmadi, M.; Guinel, M. J.-F. and Katiyar, R. S. 2013, 'Temperature-Dependent Raman Studies and Thermal Conductivity of Few-Layer MoS₂', *The Journal Physical Chemistry C*, vol. 117, no. 17, pp. 9042–9047.
- 76 Huang, W.; Da, H. and Liang, G.; 2013, 'Thermoelectric performance of MX₂ (M = Mo,W; X = S,Se) monolayers', *Journal Applied Physics*, vol. 113, no. 10, pp. 104304.
- 77 Deng, Y.; Luo, Z.; Conrad, N. J.; Liu, H.; Gong, Y.; Najmaei, S.; Ajayan, P. M.; Lou, J.; Xu, X. and Ye, P. D. 2014, 'Black Phosphorus–Monolayer MoS₂ van der Waals Heterojunction p–n Diode', *ACS Nano*, vol. 8, no. 8, pp. 8292-8299.
- 78 Na, J.; Lee, Y. T.; Lim, J. A.; Hwang, D. K.; Kim, G.-T.; Choi, W. K. and Song,

- Y.-W. 2014, 'Few-Layer Black Phosphorus Field-Effect Transistors with Reduced Current Fluctuation', *ACS Nano*, vol. 8, no. 11, pp. 11753–11762.
- 79 Zhu, W.; Yogeesh, M. N.; Yang, S.; Aldave, S. H.; Kim, J.-S.; Sonde, S.; Tao, L.; Lu, N. and Akinwande, D. 2015, 'Flexible Black Phosphorus Ambipolar Transistors, Circuits and AM Demodulator', *Nano Letters*, vol. 15, no. 3, pp. 1883–1890
- 80 Zhang, X.; Xie, H.; Liu, Z.; Tan, C.; Luo, Z.; Li, H.; Lin, J.; Sun, L.; Chen, W.; Xu, Z.; Xie, L.; Huang, W. and Zhang, H. 2015, 'Black Phosphorus Quantum Dots', *Angewandte Chemie International Edition in English*, vol. 127, no. 12, pp. 3724–3728.
- 81 Hong, T.; Chamlagain, B.; Lin, W.; Chuang, H.-J.; Pan, M.; Zhou, Z. and Xu, Y.-Q. 2014, 'Polarized photocurrent response in black phosphorus field-effect transistors', *Nanoscale*, vol. 6, pp. 8978–8983.
- 82 Li, W.; Yang, Y.; Zhang, G. and Zhang, Y.-W. 2015, 'Ultrafast and Directional Diffusion of Lithium in Phosphorene for High-Performance Lithium-Ion Battery', *Nano Letters*, vol. 15, no. 3, pp. 1691–1697.
- 83 Sun, J.; Zheng, G.; Lee, H.-W.; Liu, N.; Wang, H.; Yao, H.; Yang, W. and Cui, Y. 2014, 'Formation of Stable Phosphorus–Carbon Bond for Enhanced Performance in Black Phosphorus Nanoparticle–Graphite Composite Battery Anodes', *Nano Letters*, vol. 14, no. 8, pp. 4573–4580
- 84 Song, L.; Ci, L.; Lu, H.; Sorokin, P. B.; Jin, C.; Ni, J.; Kvashning, A. G.; Kvashning, D. G.; Lou, J.; Yakobson, B. I. and Ajayan, P. M. 2010, 'Large Scale Growth and Characterization of Atomic Hexagonal Boron Nitride Layers', *Nano Letters*, vol. 10, no. 8, pp. 3209–15.
- 85 Ouyang, T.; Chen, Y.; Xie, Y.; Yang, K.; Bao, Z. and Zhong, J. 2010, 'Thermal transport in hexagonal boron nitride nanoribbons', *Nanotechnology*, vol. 21, no. 24, pp. 245701.
- 86 Kim, K. K.; Jia, X.; Kim, S. M.; Shi, Y.; Hofmann, M.; Rodriguez-Nieva, J. F.; Dresselhaus, M.; Palacios, T. and Kong, J. 2012, 'Synthesis of monolayer hexagonal boron nitride on Cu foil using chemical vapor deposition', *Nano Letters*, vol. 12, no. 1, pp. 161–6.
- 87 Chen, Y.; Zou, J.; Campbell, S. J. and Caer, G. L. 2004, 'Boron nitride nanotubes: Pronounced resistance to oxidation', *Applied Physics Letters*, vol. 84, no. 13, pp.

- 2430.
- 88 Kubota, Y.; Watanabe, K.; Tsuda, O. and Taniguchi, T. 2007, 'Deep Ultraviolet Light-Emitting Hexagonal Boron Nitride Synthesized at Atmospheric Pressure', *Science*, vol. 317, no. 5840, pp. 932-934.
- 89 Takashi' S. and Tomoyoshi, T. 2000, 'Dielectric Constant of Boron Nitride Films Synthesized by Plasma-Assisted Chemical Vapor Deposition', *Japanese Journal of Applied Physics*, vol. 39, L1101.
- 90 Ataca, C.; Şahin, H. and Ciraci, S. 2012, 'Stable, Single-Layer MX₂ Transition-Metal Oxides and Dichalcogenides in a Honeycomb-Like Structure', *The Journal of Physical Chemistry*, vol. 116, no. 16, pp. 8983.
- 91 Wang, H.; Yu, L.; Lee, Y.; Shi, Y.; Hsu, A.; Chin, M. L.; Li, L.; Dubey, M.; Kong, J. and Palacios, T. 2012, 'Integrated Circuits Based on Bilayer MoS₂ Transistors', *Nano Letters*, vol. 12, no. 9, pp. 4674-4680.
- 92 Pu, J.; Yomogida, Y.; Liu, K.-K.; Li, L.-J.; Iwasa, Y. and Takenobu, T. 2012, 'Highly Flexible MoS₂ Thin-Film Transistors with Ion Gel Dielectrics', *Nano Letters*, vol. 12, no. 8, pp. 4013-4017.
- 93 Ross, J. S.; Klement, P.; Jones, A. M.; Ghimire, N. J.; Yan, J.; Mandrus, D. G.; Taniguchi, T.; Watanabe, K.; Kitamura, K.; Yao, W.; Cobden, D. H. and Xu, X. 2014, 'Electrically tunable excitonic light-emitting diodes based on monolayer WSe₂ p-n junctions', *Nature Nanotechnology*, vol. 9, pp. 268-272.
- 94 Baugher, B. W. H.; Churchill, H. O. H.; Yang, Y. and Jarillo-Herrero, P. 2014, 'Optoelectronic devices based on electrically tunable p-n diodes in a monolayer dichalcogenide', *Nature Nanotechnology*, vol. 9, pp. 262-267.
- 95 Klinovaja, J. and Loss, D. 2013, 'Spintronics in MoS₂ monolayer quantum wires', *Physical Review B*, vol. 88, no. 7, pp. 075404.
- 96 Hinnemann, B.; Moses, P. G.; Bonde, J.; Jørgensen, K. P.; Nielsen, J. H.; Horch, S.; Chorkendorff, I. and Nørskov, J. K. 2005, 'Biomimetic Hydrogen Evolution: MoS₂ Nanoparticles as Catalyst for Hydrogen Evolution', *Journal of the American Chemical Society*, vol. 127, no. 15, pp. 5308-5309.
- 97 Jaramillo, T. F.; Jørgensen, K. P.; Bonde, J.; Nielsen, J. H.; Horch, S. and Chorkendorff, I. 2007, 'Identification of Active Edge Sites for Electrochemical H₂ Evolution from MoS₂ Nanocatalysts', *Science*, vol. 317, no. 5834, pp. 100-102.

- 98 Kibsgaard, J.; Chen, Z.; Reinecke, B. N. and Jaramillo, T. F. 2012, 'Engineering the surface structure of MoS₂ to preferentially expose active edge sites for electrocatalysis', *Nature Materials*, vol. 11, pp. 963-969.
- 99 Yin, Z.; Li, H.; Li, H.; Jiang, L.; Shi, Y.; Sun, Y.; Lu, G.; Zhang, Q.; Chen, X.; Zhang, H. 2012, 'Single-layer MoS₂ phototransistors', *ACS Nano*, vol. 6, no. 1, pp. 74-80.
- 100 Das, S. and Choi, W.: Graphene synthesis. In *Graphene: Synthesis and Applications*, 1st ed.; Choi, W. and Lee, J.-w. Eds.; Taylor & Francis Group: Boca Raton, FL, 2011, vol. 3, pp. 27-63.
- 101 Whitener, K. E. and Sheehan, P. E. 2014, 'Graphene synthesis', *Diamond & Related Materials*, vol. 46, pp. 25-34.
- 102 Bao, J.; Jeppson, K.; Edwards, M.; Fu, Y.; Ye, L.; Lu, X. and Liu, J. 2016, 'Synthesis and applications of two-dimensional hexagonal boron nitride in electronics manufacturing', *Electronic Materials Letters*, vol. 12, no. 1, pp. 1-16.
- 103 Das, S.; Kim, M.; Lee, J. and Choi, W. 2014, 'Synthesis, Properties, and Applications of 2-D Materials: A Comprehensive Review', *Critical Reviews in Solid State and Materials Sciences*, vol. 39, no. 4, pp. 231-252.
- 104 Fang, H.; Chuang, S.; Chang, T. C.; Takei, K.; Takahashi, T. and Javey, A. 2012, 'High-Performance Single Layered WSe₂ p-FETs with Chemically Doped Contacts', *Nano Letters*, vol. 12, no. 7, pp. 3788-3792.
- 105 Novoselov, K. S.; Jiang, D.; Schedin, F.; Booth, T. J.; Khotkevich, V. V.; Morozov, S. V. and Geim, A. K. 2005, 'Two-dimensional atomic crystals', *Proceedings of the National Academy of Sciences of the United States of America*, vol. 102, no. 30, pp. 10451-10453.
- 106 Braga, D.; Gutiérrez Lezama, I.; Berger, H. and Morpurgo, A. F. 2012, 'Quantitative Determination of the Band Gap of WS₂ with Ambipolar Ionic Liquid-Gated Transistors', *Nano Letters*, vol. 12, no. 10, pp. 5218-5223.
- 107 Li, L. H.; Chen, Y.; Behan, G.; Zhang, H.; Petravicc, M.; and Glushenkova, A. M. 2011, 'Large-scale mechanical peeling of boron nitridenanosheets by low-energy ball milling', *Journal Materials Chemistry*, vol. 21, no. 32, pp. 11862-11866.
- 108 Hernandez, Y.; Nicolosi, V.; Lotya, M.; Blighe, F.M.; Sun, Z.; De, S.; McGovern, I. T.; Holland, B.; Byrne, M.; Gun'ko, Y. K.; Boland, J. J.; Niraj, P.; Duesberg,

- G.; Krishnamurthy, S.; Goodhue, R.; Hutchison, J.; Scardaci, V.; Ferrai, A. C. and Coleman, J. N. 2008, 'High-yield production of graphene by liquid-phase exfoliation of graphite', *Nature Nanotechnology*, vol. 3, pp. 563–568.
- 109 Han, W. Q.; Wu, L.; Zhu, Y. and Kenji, T. T. 2008, 'Structure of chemically derived mono- and few-atomic-layer boron nitride sheets', *Applied Physics Letters*, vol. 93, no. 22, pp. 223103.
- 110 Nicolosi, V.; Chhowalla, M.; Kanatzidis, M. G.; Strano, M. S.; Coleman, J. N. 2013, 'Liquid exfoliation of layered materials', *Science*, vol. 340, no. 6139, pp. 1226419.
- 111 Coleman, J. N.; Lotya, M.; O'Neill, A.; Bergin, S. D.; King, P. J.; Khan, U.; Young, K.; Gaucher, A.; De, S.; Smith, R. J.; Shvets, I. V.; Arora, S. K.; Stanton, G.; Kim, H.-Y.; Lee, K.; Kim, G. T.; Duesberg, G. S.; Hallam, T.; Boland, J. J.; Wang, J. J.; Donegan, J. F.; Grunlan, J. C.; Moriarty, G.; Shmeliov, A.; Nicholls, R. J.; Perkins, J. M.; Grieveson, E. M.; Theuwissen, K.; McComb, D. W.; Nellist, P. D. and Nicolosi, V. 2011, 'Two-Dimensional Nanosheets Produced by Liquid Exfoliation of Layered Materials', *Science*, vol. 331, no. 6017, pp. 568–571.
- 112 Lotya, M.; Hernandez, Y.; King, P.J.; Smith, R.J.; Nicolosi, V.; Karlsson, L.S.; Blighe, F.; De, S.; Wang, Z.; McGovern, I. T. ; Duesberg, G. S. and Coleman, J. N. 2009, 'Liquid Phase Production of Graphene by Exfoliation of Graphite in Surfactant/Water Solutions', *Journal of the American Chemical Society*, vol. 131, no. 10, pp. 3611–3620.
- 113 Lotya, M.; King, P.J.; Khan, U.; De, S.; Coleman, J.N. 2010, 'High-Concentration, Surfactant-Stabilized Graphene Dispersions', *ACS Nano*, vol. 4, no. 6, pp. 3155–3162.
- 114 Lee, K.; Kim, H.-Y.; Lotya, M.; Coleman, J. N.; Kim, G.-T.; and Duesberg, G. S. 2011, 'Electrical Characteristics of Molybdenum Disulfide Flakes Produced by Liquid Exfoliation', *Advanced Materials*, vol. 23, no. 36, pp. 4178–4182.
- 115 Dreyer, D.R.; Park, S.; Bielawski, C.W.; Ruoff, R.S. 2010, 'The chemistry of graphene oxide', *Chemical Society Reviews*, vol. 39, no. 1, pp. 228–240.
- 116 Schniepp, H.C.; Li, J.-L.; McAllister, M.J.; Sai, H.; Herrera-Alonso, M.; Adamson, D.H.; Prud'homme, R. K.; Car, R.; Saville, D. A. and Aksay, I. A. 2006, 'Functionalized single graphene sheets derived from splitting graphite oxide', *The Journal of Physical Chemistry B*, vol. 110, no. 17, pp. 8535–8539.

- 117 Wei, Z.; Wang, D.; Kim, S.; Kim, S.-Y.; Hu, Y.; Yakes, M.K.; Laracuenta, A. R.; Dai, Z.; Marder, S. R.; Berger, C.; King, W. P.; Wa, D. H.; Sheehan, P. E.; Riedo, E. 2010, 'Nanoscale tunable reduction of graphene oxide for graphene electronics', *Science*, vol. 328, no. 5984, pp. 1373–1376.
- 118 Nag, A.; Raidongia, K.; Hembram, K. P. S. S.; Datta, R.; Waghmare, U. V. and Rao. C. N. R. 2010, 'Graphene analogues of BN: novel synthesis and properties', *ACS Nano*, vol. 4, no. 3, pp. 1539–1544.
- 119 Yu, J.; Li, J.; Zhang, W. and Chang, H. 2015, 'Synthesis of high quality two-dimensional materials via chemical vapor deposition', *Chemical Science*, vol. 6, pp. 6705-6716.
- 120 Yan, Z.; Lin, J.; Peng, Z.; Sun, Z.; Zhu, Y.; Li, L.; Xiang, C.; Samuel, E. L.; Kittrell, C. and Tour, J. M. 2012, 'Toward the Synthesis of Wafer-Scale Single-Crystal Graphene on Copper Foils', *ACS Nano*, vol. 6, no. 10, pp. 9110–9117.
- 121 Gan, L. and Luo, Z. 2013, 'Turning off Hydrogen To Realize Seeded Growth of Subcentimeter Single-Crystal Graphene Grains on Copper', *ACS Nano*, vol. 7, no. 10, pp. 9480–9488.
- 122 Xu, X.; Zhang, Z.; Qiu, L.; Zhuang, J.; Zhang, L.; Wang, H.; Liao, C.; Song, H.; Qiao, R.; Gao, P.; Hu, Z.; Liao, L.; Liao, Z.; Yu, D.; Wang, E.; Ding, F.; Peng, H.; Liu, K. 2016, 'Ultrafast growth of single-crystal graphene assisted by a continuous oxygen supply', *Nature Nanotechnology*, vol. 11, pp. 930-935.
- 123 Hao, Y.; Bharathi, M.S.; Wang, L.; Liu, Y.; Chen, H.; Nie, S.; Wang, X.; Chou, H.; Tan, C.; Fallahazad, B.; Ramanarayan, H.; Magnuson, C.W.; Tutuc, E.; Yakobson, B.I.; McCarty, K.F.; Zhang, Y.W.; Kim, P.; Hone, J.; Colombo, L.; Ruoff, R.S. 2013, 'The Role of Surface Oxygen in the Growth of Large Single-Crystal Graphene on Copper', *Science*, vol. 342, no. 6159, pp. 720–723.
- 124 Addou, R.; Dahal, A.; Sutter, P.; Batzill, M. 2013, 'Monolayer graphene growth on Ni(111) by low temperature chemical vapor deposition', *Applied Physics Letters*, vol. 100, no. 2, pp. 021601.
- 125 Gao, L.; Ren, W.; Xu, H.; Jin, L.; Wang, Z.; Ma, T.; Ma, L.-P.; Zhang, Z.; Fu, Q.; Peng, L.-M.; Bao, X.; Cheng, H.-M. 2012, 'Repeated growth and bubbling transfer of graphene with millimetre-size single-crystal grains using platinum', *Nature Communications*, vol. 3, no. 699.
- 126 Lee, J. H.; Lee, E.K.; Joo, W.-J.; Jang, Y.; Kim, B.-S.; Lim, J.Y.; Choi, S.-H.;

- Ahn, S.J.; Ahn, J.R.; Park, M.-H. 2014, 'Wafer-scale growth of single-crystal monolayer graphene on reusable hydrogen-terminated germanium', *Science*, vol. 344, no. 6181, pp. 286–289.
- 127 Coraux, J.; N'Diaye, A.T.; Engler, M.; Busse, C.; Wall, D.; Buckanie, N.; Meyer zu Heringdorf, F.-J.; van Gastel, R.; Poelsema, B.; Michely, T. 2009, 'Growth of graphene on Ir(111)', *New Journal of Physics*, vol. 11, pp. 023006.
- 128 Pan, Y.; Zhang, H.; Shi, D.; Sun, J.; Du, S.; Liu, F.; Gao, H.-j. 2009, 'Highly Ordered, Millimeter-Scale, Continuous, Single-Crystalline Graphene Monolayer Formed on Ru (0001)', *Advanced Materials*, vol. 21, no. 27, pp. 2777–2780.
- 129 Liu, X.; Fu, L.; Liu, N.; Gao, T.; Zhang, Y.; Liao, L.; Liu, Z. 2011, 'Segregation Growth of Graphene on Cu-Ni Alloy for Precise Layer Control', *The Journal of Physical Chemistry C*, vol. 115, no. 24, pp.11976–11982.
- 130 Wen, Y.; Shang, X.; Dong, J.; Xu, K.; He, J.; and Jiang, C. 2015, 'Ultraclean and large-area monolayer hexagonal boron nitride on Cu foil using chemical vapor deposition', *Nanotechnology*, vol. 26, no. 27, pp. 275601;.
- 131 Novoselov, K. 2007, 'Graphene: Mind the gap', *Nature Materials*, vol. 6, pp. 720-721.
- 132 Eda, G.; Fanchini, G.; Chhowalla, M. 2008, 'Large-area ultrathin films of reduced graphene oxide as a transparent and flexible electronic material', *Nature Nanotechnology*, vol. 3, no. 5, pp. 270-274.
- 133 Stankovich, S.; Dikin, D. A.; Piner, R. D.; Kohlhaas, K. A.; Kleinhammes, A.; Jia, Y.; Wu, Y.; Nguyen, S. T.; Ruoff, R. S. 2007, 'Synthesis of graphene-based nanosheets via chemical reduction of exfoliated graphite oxide', *Carbon*, vol. 45, no. 7, pp. 1558-1565.
- 134 Si, Y.; Samulski, E. T. 2008, 'Synthesis of Water Soluble Graphene', *Nano Letters*, vol. 8, no. 6, pp. 1679-1682.
- 135 Berger, C.; Song, Z. M.; Li, T. B.; Li, X. B.; Ogbazghi, A. Y.; Feng, R.; Dai, Z. T.; Marchenkov, A. N.; Conrad, E. H.; First, P. N.; de Heer, W. A. 2004, 'Ultrathin Epitaxial Graphite: 2D Electron Gas Properties and a Route toward Graphene-based Nanoelectronics', *The Journal of Physical Chemistry B*, vol. 108, no. 52, pp. 19912-19916.
- 136 Berger, C.; Song, Z.; Li, X.; Wu, X.; Brown, N.; Naud, C.; Mayou, D.; Li, T.; Hass, J.; Marchenkov, A. N.; Conrad, E. H.; First, P. N.; de Heer, W. A. 2006,

- ‘Electronic Confinement and Coherence in Patterned Epitaxial Graphene’, *Science*, vol. 312, no. 5777, pp. 1191-1196.
- 137 Virojanadara, C.; Syvajarvi, M.; Yakimova, R.; Johansson, L. I.; Zakharov, A. A.; Balasubramanian, T. 2008, ‘Homogeneous large-area graphene layer growth on 6H-SiC(0001)’, *Physical Review B*, vol. 78, no. 24, pp. 245403.
- 138 Hass, J.; Feng, R.; Li, T.; Li, X.; Zong, Z.; de Heer, W. A.; First, P. N.; Conrad, E. H.; Jeffrey, C. A.; Berger, C. 2006, ‘Highly ordered graphene for two dimensional electronics’, *Applied Physics Letters*, vol. 89, no. 14, pp. 143106.
- 139 de Heer, W. A.; Berger, C.; Ruan, M.; Sprinkle, M.; Li, X.B.; Hu, Y.K.; Zhang, B.Q.; Hankinson, J.; and Conrad, E. 2011, ‘Large area and structured epitaxial graphene produced by confinement controlled sublimation of silicon carbide’, *Proceedings of the National Academy of Sciences of the United States of America*, vol. 108, no. 41, pp. 16900-16905
- 140 Lu, Y. H.; Chen, W.; Feng, Y. P.; He, P. M. 2009, ‘Tuning the Electronic Structure of Graphene by an Organic Molecule’, *The Journal of Physical Chemistry B*, vol. 113, no. 1, pp. 2-5.
- 141 Ang, P. K.; Wang, S.; Bao, Q. L.; Thong, J. T. L.; Loh, K. P. 2009, ‘High-Throughput Synthesis of Graphene by Intercalation–Exfoliation of Graphite Oxide and Study of Ionic Screening in Graphene Transistor’, *Acs Nano*, vol. 3, no. 11, pp. 3587-3594.
- 142 Reina, A.; Thiele, S.; Jia, X. T.; Bhaviripudi, S.; Dresselhaus, M. S.; Schaefer, J. A.; Kong, J. 2009, ‘Growth of large-area single- and Bi-layer graphene by controlled carbon precipitation on polycrystalline Ni surfaces’, *Nano Research*, vol. 2, no. 6, pp. 509-516.
- 143 Li, X.; Cai, W.; Colombo, L.; Ruoff, R. S. 2009, ‘Evolution of Graphene Growth on Ni and Cu by Carbon Isotope Labeling’, *Nano Letters*, vol. 9, no. 12, pp. 4268-4272.
- 144 Sutter, P. W.; Flege, J. I.; Sutter, E. A. 2008, ‘Epitaxial graphene on ruthenium’, *Nature Materials*, vol. 7, pp. 406-411.
- 145 P. R. Somani, S. P. Somani and M. Umeno, 2006, ‘Planer nano-graphenes from camphor by CVD’, *Chemical Physics Letters*, vol. 430, no. 1, pp. 56–59.
- 146 Klink, C.; Stensgaard, I.; Besenbacher, F.; Laegsgaard, E. 1995, ‘An STM study of carbon-induced structures on Ni(111): evidence for a carbidic-phase clock

- reconstruction', *Surface Science*, vol. 342, no. 1-3, pp. 250-260.
- 147 Dedkov, Y. S.; Shikin, A. M.; Adamchuk, V. K.; Molodtsov, S. L.; Laubschat, C.; Bauer, A.; Kaindl, G. 2001, 'Intercalation of copper underneath a monolayer of graphite on Ni(111)', *Physical Review B*, vol. 64, no. 3-15, pp. 035405.
- 148 Shikin, A. M.; Prudnikova, G. V.; Adamchuk, V. K.; Moresco, F.; Rieder, K. H. 2000, 'Surface intercalation of gold underneath a graphite monolayer on Ni(111) studied by angle-resolved photoemission and high-resolution electron-energy-loss spectroscopy', *Physical Review B*, vol. 62, no. 19, pp. 13202-13208.
- 149 Eom, D.; Prezzi, D.; Rim, K. T.; Zhou, H.; Lefenfeld, M.; Xiao, S.; Nuckolls, C.; Hybertsen, M. S.; Heinz, T. F.; Flynn, G. W. 2009, 'Structure and Electronic Properties of Graphene Nanoislands on Co(0001)', *Nano Letters*, vol. 9, no. 8, pp. 2844-2848.
- 150 Varykhalov, A.; Rader, O. 2009, 'Graphene grown on Co(0001) films and islands: Electronic structure and its precise magnetization dependence', *Physical Review B*, vol. 80, no. 3, pp. 035437.
- 151 Gao, L.; Guest, J. R.; Guisinger, N. P. 2010, 'Epitaxial Graphene on Cu(111)', *Nano Letters*, vol. 10, no. 9, pp. 3512-3516.
- 152 Lee, Y.; Bae, S.; Jang, H.; Jang, S.; Zhu, S.-E.; Sim, S. H.; Song, Y. I.; Hong, B. H.; Ahn, J.-H. 2010, 'Wafer-scale Synthesis and Transfer of Graphene Films', *Nano Letters*, vol. 10, no. 2, pp. 490-493.
- 153 Pan, Y.; Zhang, H. G.; Shi, D. X.; Sun, J. T.; Du, S. X.; Liu, F.; Gao, H. J. 2009, 'Highly Ordered, Millimeter-Scale, Continuous, Single-Crystalline Graphene Monolayer Formed on Ru (0001)', *Advanced Materials*, vol. 20, no. 27, pp. 2777.
- 154 Marchini, S.; Günther, S.; Wintterlin, J. 2007, 'Scanning tunneling microscopy of graphene on Ru(0001)', *Physical Review B*, vol. 76, no. 7, pp. 075429.
- 155 Starodub, E.; Maier, S.; Stass, I.; Bartelt, N. C.; Feibelman, P. J.; Salmeron, M.; McCarty, K. F. 2009, 'Graphene growth by metal etching on Ru(0001)', *Physical Review B*, vol. 80, no. 23, pp. 235422.
- 156 Sutter, E.; Albrecht, P.; Sutter, P. 2009, 'Graphene growth on polycrystalline Ru thin films', *Applied Physics Letters*, vol. 95, no. 13, pp. 133109.
- 157 Wang H., Wang G. Z., Bao P. F., Yang S. L., Zhu W., Xie X., and Zhang W. J., 2012, 'Controllable Synthesis of Submillimeter Single-Crystal Monolayer Graphene Domains on Copper Foils by Suppressing Nucleation', *Journal of the*

- American Chemical Society*, vol. 134, no. 8, pp. 3627-3630
- 158 Li X. S., Magnuson C. W., Venugopal A., Tromp R. M., Hannon J. B., Vogel E. M., Colombo L. G., and Ruoff R. S. 2011, 'Large-Area Graphene Single Crystals Grown by Low-Pressure Chemical Vapor Deposition of Methane on Copper', *Journal of the American Chemical Society*, vol. 133, no. 9, pp. 2816-2819
- 159 Sicot, M.; Bouvron, S.; Zander, O.; Rüdiger, U.; Dedkov, Y. S.; Fonin, M. 2010, 'Nucleation and growth of nickel nanoclusters on graphene Moiré on Rh(111)', *Applied Physics Letters*, vol. 96, no. 9, pp. 093115.
- 160 Wang, B.; Caffio, M.; Bromley, C.; Fruchtl, H.; Schaub, R. 2010, 'Coupling Epitaxy, Chemical Bonding, and Work Function at the Local Scale in Transition Metal-Supported Graphene', *Acs Nano*, vol. 4, no. 10, pp. 5773-5782.
- 161 Coraux, J.; N'Diaye, A. T.; Busse, C.; Michely, T. 2008, 'Structural Coherency of Graphene on Ir(111)', *Nano Letters*, vol. 8, no. 2, pp. 565-570.
- 162 N'Diaye, A. T.; Coraux, J.; Plasa, T. N.; Busse, C.; Michely, T. 2008, 'Structure of epitaxial graphene on Ir(111)', *New Journal of Physics*, vol. 10, no. 4, pp. 043033.
- 163 Sutter, P.; Sadowski, J. T.; Sutter, E. 2009, 'Graphene on Pt(111): Growth and substrate interaction', *Physical Review B*, vol. 80, no. 24, pp. 245411.
- 164 Gao, M.; Pan, Y.; Zhang, C.; Hu, H.; Yang, R.; Lu, H.; Cai, J.; Du, S.; Liu, F.; Gao, H.-J. 2010, 'Tunable interfacial properties of epitaxial graphene on metal substrates', *Applied Physics Letter*, vol. 96, no. 5, pp. 053109.
- 165 Land, T. A.; Michely, T.; Behm, R. J.; Hemminger, J. C.; Comsa, G. 1992, 'STM investigation of single layer graphite structures produced on Pt(111) by hydrocarbon decomposition', *Surface Science*, vol. 264, no. 3, pp. 261-270.
- 166 Kwon, S. Y.; Ciobanu, C. V.; Petrova, V.; Shenoy, V. B.; Bareno, J.; Gambin, V.; Petrov, I.; Kodambaka, S. 2009, 'Growth of Semiconducting Graphene on Palladium', *Nano Letters*, vol. 9, no. 12, pp. 3985-3990.
- 167 An, J.; Voelkl, E.; Suk, J.W.; Li, X.; Magnuson, C.W.; Fu, L.; Tiemeijer, P.; Bischoff, M.; Freitag, B.; Popova, E.; Ruoff, R.S. 2011, 'Domain (Grain) Boundaries and Evidence of "Twinlike" Structures in Chemically Vapor Deposited Grown Graphene', *ACS Nano*, vol. 5, no. 4, pp. 2433-2439.
- 168 Jauregui, L.A.; Cao, H.; Wu, W.; Yu, Q.; Chen, Y.P. 2011, 'Electronic properties of grains and grain boundaries in graphene grown by chemical vapor deposition',

- Solid State Communications*, vol. 151, no. 16, pp.1100–1104.
- 169 Kim, K.; Lee, Z.; Regan, W.; Kisielowski, C.; Crommie, M.F.; Zettl, A. 2011, ‘Grain Boundary Mapping in Polycrystalline Graphene’, *ACS Nano*, vol. 5, no. 4, pp. 2142–2146.
- 170 Vlassiouk, I.; Regmi, M.; Fulvio, P.; Dai, S.; Datskos, P.; Eres, G. and Smirnov, S. 2011, ‘Role of Hydrogen in Chemical Vapor Deposition Growth of Large Single-Crystal Graphene’, *ACS Nano*, vol. 5, no. 7, pp. 6069–6076.
- 171 Wu, Y. A.; Fan, Y.; Speller, S.; Creeth, G. L.; Sadowski, J. T.; He, K.; Robertson, A. W.; Allen, C. S. and Warner, J. H. 2012, ‘Large Single Crystals of Graphene on Melted Copper Using Chemical Vapor Deposition’, *ACS Nano*, vol. 6, no. 6, pp. 5010-5017.
- 172 Wu, T.; Zhang, X.; Yuan, Q.; Xue, J.; Lu, G.; Liu, Z.; Wang, H.; Wang, H.; Ding, F.; Yu, Q.; Xie X. and Jiang, M. 2016, ‘Fast growth of inch-sized single-crystalline graphene from a controlled single nucleus on Cu–Ni alloys’, *Nature Materials*, vol. 15, no. 1, pp. 43-47.
- 173 Magnuson, C. W.; Kong, X.; Ji, H.; Tan, C.; Li, H.; Piner, R.; Ventrice, C. A. and Ruoff, R. S. 2014, ‘Copper oxide as a “self-cleaning” substrate for graphene growth’, *Journal of Materials Research*, vol. 29, no. 3, pp. 403–409.
- 174 Li, Z. C.; Wu, P.; Wang, C. X.; Fan, X. D.; Zhang, W. H.; Zhai, X. F. 2011, ‘Low-Temperature Growth of Graphene by Chemical Vapor Deposition Using Solid and Liquid Carbon Sources’, *ACS Nano*, vol. 5, no. 4, pp. 3385–3390.
- 175 Lahiri, J.; Miller, T.; Adamska, L.; Oleynik, I. I. and Batzill, M. *Nano Letters*, 11 (2), 518–522 (2011).
- 176 Chen, H.; Zhu, W. G. and Zhang, Z. Y. 2010, ‘Contrasting Behavior of Carbon Nucleation in the Initial Stages of Graphene Epitaxial Growth on Stepped Metal Surfaces’, *Physical Review Letters*, vol. 104, no. 18, pp.186101.
- 177 Riikonen, S.; Krasheninnikov, A. V.; Halonen, L. and Nieminen, R. M. 2012, ‘The Role of Stable and Mobile Carbon Adspecies in Copper-Promoted Graphene Growth’, *The Journal of Physical Chemistry C*, vol. 116, no. 9, pp. 5802–5809.
- 178 Gao, J. F.; Yuan, Q. H.; Hu, H.; Zhao, J. J. and Ding, F. 2011, ‘Formation of Carbon Clusters in the Initial Stage of Chemical Vapor Deposition Graphene Growth on Ni(111) Surface’, *The Journal of Physical Chemistry C*, vol. 115, no.

- 36, pp. 17695–17703. ^[1]_[SEP]
- 179 Yuan, Q. H.; Gao, J. F.; Shu, H. B.; Zhao, J. J.; Chen, X. S. and Ding, F. 2012, ‘Magic Carbon Clusters in the Chemical Vapor Deposition Growth of Graphene’, *Journal of the American Chemical Society*, vol. 134, no. 6, pp. 2970–2975.
- 180 Cui, Y.; Fu, Q. A.; Zhang, H. and Bao, X. H. 2011, ‘Formation of identical-size graphene nanoclusters on Ru(0001)’, *Chemical Communications*, vol. 47, no. 5, pp. 1470–1472. ^[1]_[SEP]
- 181 Gao, J. F.; Yip, J.; Zhao, J. J.; Yakobson, B. I. and Ding, F. 2012, ‘Graphene Nucleation on Transition Metal Surface: Structure Transformation and Role of the Metal Step Edge’, *Journal of the American Chemical Society*, vol. 134, no. 22, pp. 9534–9534. ^[1]_[SEP]
- 182 Zhang, X.; Yuan, Q.; Shu, H. and Ding, F. 2013, Mechanisms of Graphene Chemical Vapor Deposition (CVD) Growth, in *Graphene Chemistry: Theoretical Perspectives* (eds D.-E. Jiang and Z. Chen), John Wiley & Sons, Ltd, Chichester, UK. doi: 10.1002/9781118691281.ch12
- 183 Gao, J. F.; Zhao, J. J. and Ding, F. 2012, ‘Transition Metal Surface Passivation Induced Graphene Edge Reconstruction’, *Journal of the American Chemical Society*, vol. 134, no.14, pp. 6204–6209. ^[1]_[SEP]
- 184 Shu, H. B.; Chen, X. S.; Tao, X. M. and Ding, F. 2012, ‘Edge Structural Stability and Kinetics of Graphene Chemical Vapor Deposition Growth’, *ACS Nano*, vol. 6, no. 4, pp. 3243–3250.
- 185 Liu, Y. Y.; Dobrinsky, A.; Yakobson, B. I. 2010, ‘Graphene edge from armchair to zigzag: the origins of nanotube chirality?’, *Physical Review Letters*, vol. 105, no. 23, pp. 235502.
- 186 Artyukhov, Y. L. V. I. and Yakobson, B. I. 2012, ‘Equilibrium at the edge and atomistic mechanisms of graphene growth’, *Proceedings of the National Academy of Sciences of the United States of America*, vol. 109, no. 38, pp. 15136–15140.
- 187 Zhang, X. Y.; Xu, Z. W.; Li, H.; Xin, H. and Ding, F. 2012, ‘How the Orientation of Graphene Is Determined during Chemical Vapor Deposition Growth’, *The Journal of Physical Chemistry Letters*, vol. 3, no. 19, pp. 2822–2827.
- 188 Zhu, Z. and Tománek, D. 2014, ‘Semiconducting Layered Blue Phosphorus: A Computational Study’, *Physical Review Letters*, vol. 112, no. 17, pp. 176802.

- 189 Guan, J.; Zhu, Z. and Tománek, D. 2014, 'Phase Coexistence and Metal-Insulator Transition in Few-Layer Phosphorene: A Computational Study', *Physical Review Letters*, vol. 113, no. 14, pp. 046804.
- 190 Guan, J.; Zhu, Z. and Tománek, D. 2014, 'Tiling Phosphorene', *ACS nano*, vol. 8, no. 12, pp. 12763-12768.
- 191 Zhao, T.; He, C. Y.; Ma, S. Y.; Zhang, K. W.; Peng, X. Y.; Xie, G. F. and Zhong, J. X. 2015, 'A new phase of phosphorus: the missed tricycle type red phosphorene', *Journal of Physics: Condensed Matter*, vol. 27, no. 26, pp. 265301.
- 192 Zhang, S.; Xie, M.; Li, F.; Yan, Z.; Li, Y.; Kan, E.; Liu, W.; Chen, Z. and Zeng, Z. 2016, 'Semiconducting Group 15 Monolayers: A Broad Range of Band Gaps and High Carrier Mobilities', *Angewandte Chemie International Edition in English*, vol. 128, no. 5, pp. 1698-1701.
- 193 Lu, W.; Nan, H.; Hong, J.; Chen, Y.; Zhu, C.; Liang, Z.; Ma, X.; Ni, Z.; Jin, C.; Zhang, Z. 2014, 'Plasma-assisted fabrication of monolayer phosphorene and its Raman characterization', *Nano Research*, vol. 7, no. 6, pp. 853-859.
- 194 Brent, J. R.; Savjani, N.; Lewis, E. A.; Haigh, S. J.; Lewis, D. J. and O'Brien, P. 2014, 'Production of few-layer phosphorene by liquid exfoliation of black phosphorus', *Chemical Communications*, vol. 50, no. 87, pp. 13338-13341.
- 195 Smith, J. B.; Hagaman, D.; Ji, H. 2016, 'Growth of 2D black phosphorus film from chemical vapor deposition', *Nanotechnology*, vol. 27, no. 21, pp. 215602.
- 196 Zhang, J. L.; Zhao, S.; Han, C.; Wang, Z.; Zhong, S.; Sun, S.; Guo, R.; Zhou, X.; Gu, C. D.; Yu, K. D.; Li, Z.; and Chen, W. 2016, 'Epitaxial Growth of Single Layer Blue Phosphorus: A New Phase of Two-Dimensional Phosphorus', *Nano Letters*, vol. 16, no. 8, pp. 4903-4908.
- 197 Zhou, H. L.; Yu, W. J.; Liu, L.; Cheng, R.; Chen, Y.; Huang, X.; Liu, Y.; Wang, Y.; Huang, Y. and Duan, X. 2013, 'Chemical vapour deposition growth of large single crystals of monolayer and bilayer graphene', *Nature Communications*, vol. 4, no. 2096.
- 198 Goddard, W. A.; Dunning, T. H.; Hunt, W. J. and Hay, P. J. 1973, 'Generalized valence bond description of bonding in low-lying states of molecules', *Accounts of Chemical Research*, vol. 6, no. 11, pp. 368-376.
- 199 van Lenthe, J. H., Dijkstra, F., & Havenith, R. 2002, TURTLE - A gradient VBSCF Program. Theory and Studies of Aromaticity. In *Valence Bond*

- Theory*. (Vol. 10, pp. 79-112). (Theoretical and Computational Chemistry 10.). Amsterdam: Elsevier.
- 200 Shaik, S. and Hiberty, P. C. 2004, Valence Bond Theory, Its History, Fundamentals, and Applications: A Primer, in *Reviews in Computational Chemistry*, Volume 20 (eds K. B. Lipkowitz, R. Larter and T. R. Cundari), John Wiley & Sons, Inc., Hoboken, NJ, USA. doi: 10.1002/0471678856.ch1
- 201 Fischer, C. F. 1987, 'General Hartree-Fock program', *Computer Physics Communications*, vol. 43, no. 3, pp. 355-365.
- 202 Hoffmann, R. 1963, 'An Extended Hückel Theory. I. Hydrocarbons', *Journal of Chemical Physics*, vol. 39, no. 6, pp. 1397.
- 203 Slater, J. C.; Koster, G. F. 1954, 'Simplified LCAO method for the Periodic Potential Problem', *Physical Review*, vol. 94, no. 6, pp. 1498-1524.
- 204 Parr, R. G.; Yang, W. 1989, 'Density-Functional Theory of Atoms and Molecules' *New York: Oxford University Press*. ISBN 0-19-504279-4.
- 205 Dirac, P. A. M. 'The principles of quantum mechanics', *Clarendon Press: Oxford*, 1958.
- 206 Born, M. and Oppenheimer, R. 1926, 'Zur Quantentheorie der Molekeln', *Annalen der Physik*, vol. 389, no. 20, pp. 457.
- 207 Thomas, L. H. 1927, 'The calculation of atomic fields', *Proceedings of the Cambridge Philosophical Society*, vol. 23, no. 5, pp. 542-548.
- 208 Fermi, E. 1927, 'Un Metodo Statistico per la Determinazione di alcune Proprietà dell'Atomo', *Rend. Accad. Naz. Lincei.*, vol. 6, pp. 602-607.
- 209 Hohenberg, P. and Kohn, W. 1964, 'Inhomogeneous Electron Gas', *Physical Review*, vol. 136, no. 3B, pp. B864.
- 210 Kohn, W.; Sham, L. J. 1965, 'Self-Consistent Equations Including Exchange and Correlation Effects', *Physical Review*, vol. 140, no. 4A, pp. A1133-A1138.
- 211 Perdew, J. P.; Ruzsinszky, A.; Tao J.; Staroverov, V. N.; Scuseria, G.; Csonka, G. I. 2005, 'Prescriptions for the design and selection of density functional approximations: More constraint satisfaction with fewer fits', *Journal of Chemical Physics*, vol. 123, no. 6, pp. 062201.
- 212 Perdew, J. P.; Burke, K. and Ernzerhof, M. 1996, 'Generalized Gradient Approximation Made Simple', *Physical Review Letters*, vol. 77, no. 18, pp. 3865.

- 213 Heyd, J.; Scuseria, G. E.; Ernzerhof, M. E. 2003, 'Hybrid functionals based on a screened Coulomb potential', *The Journal of Chemical Physics*, vol. 118, no. 18, pp. 8207–8215.
- 214 Heyd, J.; Scuseria, G. E.; Ernzerhof, M. E. 2006, 'Erratum: "Hybrid functionals based on a screened Coulomb potential" [J. Chem. Phys. 118, 8207, 2003]', *The Journal of Chemical Physics*, vol. 124, pp. 219906.
- 215 Kresse, G. and Hafner, J. 1993, 'Ab initio molecular dynamics for open-shell transition metals', *Physical Review B*, vol. 48, no. 17, pp. 13115-13118.
- 216 Kresse, G. and Furthmüller, J. 1996, 'Efficiency of ab-initio total energy calculations for metals and semiconductors using a plane-wave basis set', *Computational Materials Science*, vol. 6, no. 1, pp. 15-50.
- 217 Kresse, G. and Joubert, D. 1999, 'From ultrasoft pseudopotentials to the projector augmented-wave method', *Physical Review B*, vol. 59, no. 3, pp. 1758.
- 218 Grimme, S. 2006, 'Semiempirical GGA-type density functional constructed with a long-range dispersion correction', *Journal of Computational Chemistry*, vol. 27, pp. 1787-1799
- 219 Monkhorst, H. and Pack, J. 1976, 'Special points for Brillouin-zone integrations', *Physical Review B*, vol. 13, no. 12, pp. 5188–5192.
- 220 Jónsson, H.; Mills, G. and Jacobsen, K. W. 1998, *Classical and Quantum Dynamics in Condensed Phase Simulations*, edited by B. J. Berne, G. Ciccotti, and D. F. Coker, World Scientific, Singapore, pp. 385–404.
- 221 Sheppard, D.; Terrell, R. and Henkelman, G. 2008, 'Optimization methods for finding minimum energy paths', *The Journal of Chemical Physics*, vol. 128, no. 13, pp. 134106.
- 222 Pratt, L. R. 1986, 'A statistical method for identifying transition states in high dimensional problems', *The Journal of Chemical Physics*, vol. 85, no. 9, pp. 5045-5048.
- 223 Henkelman, G.; Uberuaga, B. P.; Jónsson, H. 2000, 'A climbing image nudged elastic band method for finding saddle points and minimum energy paths', *The Journal of Chemical Physics*, vol. 113, no. 22, pp. 9901.
- 224 Zhang, R. F.; Zhang, Y.; Zhang, Q.; Xie, H.; Qian, W.; Wei, F. 2013, 'Growth of half-meter long carbon nanotubes based on schulz- flory distribution', *ACS Nano*, vol. 7, no. 7, pp. 6156–6161. ^[L]_{SEP}

- 225 Ishizaka, A. and Shiraki, Y. 1986, 'Low-temperature surface cleaning of silicon and its application to silicon Mbe', *Journal of the Electrochemical Society*, vol. 133, no. 4, pp. 666–671.
- 226 Cowley, A. H. 1965, 'The Chemistry of the Phosphorus-Phosphorus Bond', *Chemical Reviews*, vol. 65, no. 6, pp. 617-634.
- 227 Euler, L. 1763, 'Theoremata arithmetica nova method demonstrata', *Novi Commentarii academiae scientiarum Petropolitanae*, vol. 8, pp. 74-104.
- 228 Tran, V.; Soklaski, R.; Liang, Y.; Yang, L. 2014, 'Layer-controlled band gap and anisotropic excitons in few-layer black phosphorus', *Physical Review B*, vol. 89, no. 23, pp. 235319.
- 229 Woome, A. H.; Farnsworth, T. W.; Hu, J.; Wells, R. A.; Donley, C. L. and Warren, S. C. 2015, 'Phosphorene: Synthesis, Scale-Up, and Quantitative Optical Spectroscopy', *ACS Nano*, vol. 9, no. 9, pp. 8869–8884.
- 230 Rahman, M. Z.; Kwong, C. W.; Davey, K. and Qiao, S. Z. 2016, '2D phosphorene as a water splitting photocatalyst: fundamentals to applications', *Energy and Environmental Science*, vol. 9, no. 3, pp. 709-728.
- 231 Song, X.; Gao, J.; Gao, T.; Nie, Y.; Sun, J.; Chen, J.; Jin, C.; Ding, F.; Zhang, Y.; Liu, Z. 2015, 'Wafer-scale CVD Growth of Monolayer Hexagonal Boron Nitride with Large Domain Size by Cu Foil Enclosure Approach', *Materials Science*, arXiv:1501.01740 [cond-mat.mtrl-sci]
- 232 Lee, Y.; Zhang, X.; Zhang, W.; Chang, M.; Lin, C.; Chang, K.; Yu, Y.; Wang, J.; Chang, C.; Li, ^[1]_{SP}L.; Lin, T. 2012, 'Synthesis of Large-Area MoS₂ Atomic Layers with Chemical Vapor Deposition', *Advanced Materials*, vol. 24, no. 17, pp. 2320–2325.
- 233 Okamoto, H.; Toriumi, K.; Mitani, T. and Yamashita, M. 1990, 'Optical and magnetic properties of the halogen-bridged metal complexes modified by hydrogen bondings: {M(1R,2R-cyclohexanediamine)₂Br}Br₂ (M=Pt, Pd, and Ni)', *Physical Review B*, vol. 42, no. 16, pp. 10381-10387.